OPTIMIZATION OF MULTIMODAL OCT FOR EARLY CANCER DETECTION AND DIAGNOSIS

by

Elham Abouei

B.Sc., Sharif University of Technology, 2012

M.Sc., University of British Columbia, 2014

A THESIS SUBMITTED IN PARTIAL FULFILLMENT OF

THE REQUIREMENTS FOR THE DEGREE OF

DOCTOR OF PHILOSOPHY

in

THE FACULTY OF GRADUATE AND POSTDOCTORAL STUDIES

(Physics)

THE UNIVERSITY OF BRITISH COLUMBIA

(Vancouver)

August 2021

The following individuals certify that they have read, and recommend to the Faculty of Graduate and Postdoctoral Studies for acceptance, the dissertation entitled:

Optimization of Multimodal OCT for Early Cancer Detection and Diagnosis

submitted by Elham Abouei in partial fulfillment of the requirements for

the degree of Doctor of Philosophy

in Physics

Examining Committee:

Dr. Calum MacAulay, Pathology and Laboratory Medicine, UBC

Supervisor

Dr. Pierre Lane, Biomedical Engineering, UBC

Supervisory Committee Member

Dr. Stephen Lam, Medicine, UBC

Supervisory Committee Member

Dr. Shahriar Mirabbasi, Electrical and Computer Engineering, UBC

University Examiner

Dr. Haishan Zeng, Physics and Astronomy, UBC

University Examiner

Additional Supervisory Committee Members:

Dr. Shou Tang, Electrical and Computer Engineering, UBC

Supervisory Committee Member

Abstract

In this thesis, I present improved optical imaging modalities for early cancer detection, diagnosis and prognosis of lung and cervical cancers in a minimally invasive fashion. Optical coherence tomography (OCT), which is based on low coherence interferometry of backscattered light, offers high resolution three-dimensional visualization of structures below the tissue surface. In contrast, autofluorescence imaging (AFI) detects spectral differences in fluorescence and absorption characteristics of endogenous fluorophores. A combined OCT–AFI system uses both complementary modalities to examine structural and molecular information, which may enable increased detection and characterization of features associated with disease. The motivation of this thesis is to improve the capabilities of OCT and OCT-AFI for the *in vivo* detection and localization of early cancers.

Rotary-pullback catheter-based OCT or OCT-AFI systems suffer from motion-induced artifacts. In this thesis, I developed a method for the correction of these motion artifacts present in both 2D and 3D images collected with an endoscopic OCT-AFI system. I optimized and demonstrated the suitability of this method using real and simulated NURD (non-uniform rotation distortion) phantoms and *in vivo* endoscopic pulmonary OCT-AFI. Presented is a qualitative evaluation of this method showing an enhancement of the image quality and a proposed metric to quantitatively evaluate the correction method.

Next, I evaluated a high resolution OCT system for early cervical cancer screening and diagnosis. My work characterized diagnostic OCT features of normal cervix as well as low-grade squamous intraepithelial lesions (LSIL), and high-grade squamous intraepithelial lesions (HSIL). We determined the sensitivity (100%), specificity (83%) and accuracy (85%) of this diagnostic technique in differentiating low-risk and high-risk cervical lesions.

Lastly, I present a design for a forward-viewing fiber scanning high resolution OCT probe for *in vivo* cervical imaging in the clinic. To enable high resolution imaging but allow for sufficient depth penetration into tissue, OCT systems use near-infrared light ~1000 nm in wavelength. As well, I have investigated the suitability of a new supercontinuum light source for this application.

Lay Summary

Cancer is a leading cause of death and an important barrier to increasing life expectancy worldwide. It is critical to diagnose cancer at its early stages for an effective treatment plan and reducing the mortality rate. There is a need for a non-invasive, real time and *in vivo* diagnostic tool for screening patients in the clinical setting that improves upon the limitations of current technologies.

In this thesis, I presented a motion correction method to improve image quality of pulmonary images obtained using techniques called optical coherence tomography (OCT) and autofluorescence imaging acquired as part of a lung cancer early detection study. I also investigated a high resolution OCT system for early diagnosis of cervical cancer. Further, I discussed the design and development of a novel cervical probe capable of screening and imaging cervix in the clinic. Finally, I evaluated a new light source to improve high resolution OCT imaging for biological tissue.

Preface

This thesis presents research conducted by Elham Abouei, under the guidance and supervision of Dr. Calum MacAulay.

The results from **chapter 2** have been orally presented in [C1] and published in [J1]. The content and images of this chapter are based on a collaboration with Drs. Stephen Lam and Pierre Lane. Dr. Pahlevaninezhad was responsible for data collection. I was responsible for designing and implementing the proposed algorithm, image processing and data analysis.

The results from **chapter 3** were presented in [C2] and published in [J1] and [C3]. I was responsible for literature review, modeling and simulation, applying the proposed simulation, performing all experiments, analyzing the results and data analysis.

The results from **chapter 4** have been orally presented in [C4]. I was the research lead on this study. I was responsible for the study design, data collection and image analysis. The entire work was conducted under the supervision of Dr. Guillermo Tearney and Dr. Calum MacAulay and in collaboration with Dr. Michele Follen. I conducted and coordinated all stages of this study including the University of British Columbia Research Ethics Board submission (REB number: H19-00481), data collection in the operating room and data analysis. The study performed in this chapter was also approved by the Massachusetts General Hospital Research Ethics Board (protocol number: 2016P001988). Dr. Huimin Leung and Dr. Joseph Gardecki assisted in the data collection and provided technical support for this study.

I completed the research and results presented in **Chapter 5** under the supervision of Dr. Guillermo Tearney and Dr. Calum MacAulay. Dr. Huimin Leung, Dr. Osman O. Ahsen and Dr.

Chukwuemeka (Emeka) Okoro provided technical advice and research guidance. I was responsible for literature review, design, modeling and simulation of the contents presented.

The results from **Chapter 6** have been reported to the Hamamatsu Photonics. I conducted and completed the research described in chapter 6 under the main supervision of Dr. Guillermo Tearney, and co-supervision of Dr. Joseph Gardecki and Dr. David O. Otuya, who provided research guidance, technical support and advice. I wrote most of the manuscript while Dr. Gardecki and Dr. Otuya actively participated in editing and revising. The thesis was written by Elham Abouei, with editing assistance from Dr. Calum MacAulay. The contributions from this thesis have led to the following presentations and publications:

[C1] E. Abouei*, H. Pahlevaninezhad, A. M. D. Lee, P. Lane, S. Lam, C. MacAulay, "Correction of motion artifacts in OCT-AFI data collected in airways", SPIE Photonic West (Oral presentation) , San Francisco, CA, USA, 2016 Feb 13-18.

[J1] E. Abouei*, A. M. D. Lee, H. Pahlevaninezhad, G. Hohert, M. Cue, P. Lane, S. Lam, C. MacAulay, "Correction of motion artifacts in endoscopic optical coherence tomography and autofluorescence images based on azimuthal *en face* image registration", Journal of Biomedical Optics, (2018), 23(1)

[C2] E.Abouei*, A. M. D. Lee, H. Pahlevaninezhad, G. Hohert, M. Cue, P. Lane, S. Lam, C. MacAulay, "Motion artifacts in endoscopic catheter-based images: simulation and motion correction method", SPIE Structured light (Oral presentation), Yokohama, Japan, 2018 April 25-27.

[C3] E. Abouei*, A. M. D. Lee, G. Hohert, P. Lane, S. Lam, C. MacAulay, “Quantitative Evaluation of Correction Methods and Simulation of Motion Artifacts for Rotary Pullback Imaging Catheters”, MIUA 2018, Southampton, UK

[C4] E. Abouei*, J. A. Gardecki, J. Cutler, L Ricketts-Holcomb, C. MacAulay, M. Follen, G. J. Tearney, “Pilot study of micro optical coherence tomography for detection of invasive and pre-invasive cervical lesions”, SPIE Photonic West (Oral presentation), San Francisco, CA, USA, 2020 Feb 1-6

Table of Contents

List of Tables

List of Figures

List of Abbreviations

1D: 1 dimensional

2D: two-dimensional

3D: three-dimensional

AEIR: azimuthal *en face* image registration

AFI: autofluorescence imaging

AFB: autofluorescence bronchoscopy

ARIS: azimuthal registration of image sequences

BHMC: Brookdale Hospital Medical Center

CI: confidence interval

CIN: cervical intraepithelial neoplasia

CT: computed tomography

DCF: double-clad fiber

DOF: depth of field

EDOF: extended depth of field

FD-OCT: Fourier domain OCT

FFT: fast Fourier transformation

FOV: field of view

FWHM: full width at half maximum

HIC: high-income countries

HPV: human papillomavirus

HSIL: high-grade squamous intraepithelial lesions

ID: inner diameter

KCH: Kings County Hospital

LDCT: low-dose computed tomography

LEEP: loop electrical excision procedure

LMIC: low and middle income countries

LSIL: low-grade squamous intraepithelial lesions

MDC: Multispectral Digital Colposcope

MEMS: microelectromechanical scanners

MGH: Massachusetts General Hospital

MMF: multi mode fiber

MPM: multiphoton microscopy

NA: numerical aperture

NIR: near infrared

NURD: non-uniform rotational distortion

OCT: optical coherence tomography

OD: outer diameter

OPD: optical path difference

OPL: optical path length

PAI: photoacoustic imaging

PBS: phosphate buffered saline

Pap: Papanicolaou

PSF: point spread function

ROIs: regions of interest

RP-EBUS: radial probe endobronchial ultrasound

SFE: scanning fiber endoscopes

SS-OCT: swept source domain OCT

SD-OCT: spectral domain OCT

SLDs: super-luminescent diodes

SMF: single mode fiber

SMM: single-mode-multimode

TNAB: transthoracic needle aspiration biopsy

TD-OCT: time domain OCT

vis-OCT: visible OCT

VIA: visual inspection with acetic acid

WHO: World Health Organization

WLB: white light bronchoscopy

z_R: Rayleigh range

Acknowledgements

- Special thanks to my supervisor Dr. Calum MacAulay, my advisor Dr. Guillermo (Gary) Tearney and my collaborator Dr. Michele Follen.
- Special thanks to my supervisory committee members Dr. Pierre Lane, Dr. Stephan Lam and Dr. Shuo Tang for their dedication, support and kindness.
- Special thanks to Geoffrey Hohert, Sylvia Lam and Dr. Anthony Lee.
- Special thanks to Kings County Hospital staff, specifically Olga Sandy and the Brookdale Hospital Medical Center staff, specifically Felipe Castaneda.
- Special thanks to the Tearney laboratory members specifically Dr. Joseph Gardeki, Dr. Huimin Leung, Dr. David Otuya, Dr. Osman Ahsen and Chukwuemeka (Emeka) Okoro.
- Special thanks to our funding: This work was supported by grants from the Terry Fox Research Institute and Canadian Institute of Health Research (to Dr. Calum MacAulay) and Hamamatsu Photonics (to Dr. Guillermo Tearney). We also gratefully acknowledge the generous support provided by the John and Dottie Remondi Family (to Dr. Guillermo Tearney).
- Special thanks to my family and friends. To my lovely parents and adoring siblings Akram, Aazam and Abolfazl for their continuous encouragement and unconditional support whenever I needed through this journey. I would also like to thank my friends who I was so lucky to have them and their companions in this endeavor: Maryam, Marjan, Masoud, Yalda and Zahra.

Dedication

To my beloved parents.

Chapter 1: Introduction

This dissertation presents techniques for cancer detection, diagnosis and prognosis using non or minimally invasive optical imaging modalities. The focus is on the development of image processing algorithms and optical imaging systems that are applied to tissues of the lung and cervix to detect, localize, diagnose, and prognose cancer.

The first half of this thesis presents an image processing algorithm to assist with improving image quality and quantifying this improvement on artificial images. The second half of this thesis presents an optical imaging modality for screening, early diagnosis, and classification of low-risk and high-risk lesions of cervical dysplasia.

This chapter provides background information including cancer statistics, the importance of medical imaging for early cancer diagnosis and a relevant introduction to the study presented in this thesis. I summarize some of the current state of the art research relevant to our subjects of interest. Finally, I present an overview of this thesis and provide a summary of the dissertation.

1.1 Cancer Statistics

Cancer is a leading cause of death and an important barrier to increasing life expectancy worldwide. According to estimates from the World Health Organization (WHO) in 2019, cancer is the first or second leading cause of death before the age of 70 years in most countries. The global cancer burden is expected to rise by 47% from 2020 to 2040, with a larger increase in developing versus developed countries due to demographic changes. Overall, the burden of cancer incidence and mortality is rapidly growing worldwide. [1]

It is critical to build a sustainable infrastructure for both the communication of cancer prevention measures and provisions for cancer care in developing countries for global cancer control. Efforts to promote early detection through improved awareness and clinical examination by skilled health providers, followed by timely and appropriate treatment, are essential components to improving survival and reducing the mortality rate. [1]

1.1.1 Lung Cancer

Lung cancer was the second most commonly diagnosed cancer and the leading cause of cancer death in 2020. The 5-year survival rate of patients with lung cancer is only 10% to 20% in most countries (diagnosed during 2010 through 2014). [1] Because of low survival rates even in more developed countries, lung cancer mortality rates are generally similar to incidence rates. [2] The driving cause for this low survival rate is that patients are usually diagnosed at an advanced stage, when limited options are available for effective and curative treatment. Figure 1-1 shows premalignant airway fields and progression of lung cancer. Early detection may improve lung cancer survival rate; therefore, screening and early detection of lung cancer is the key to improving the survival rate. [3]

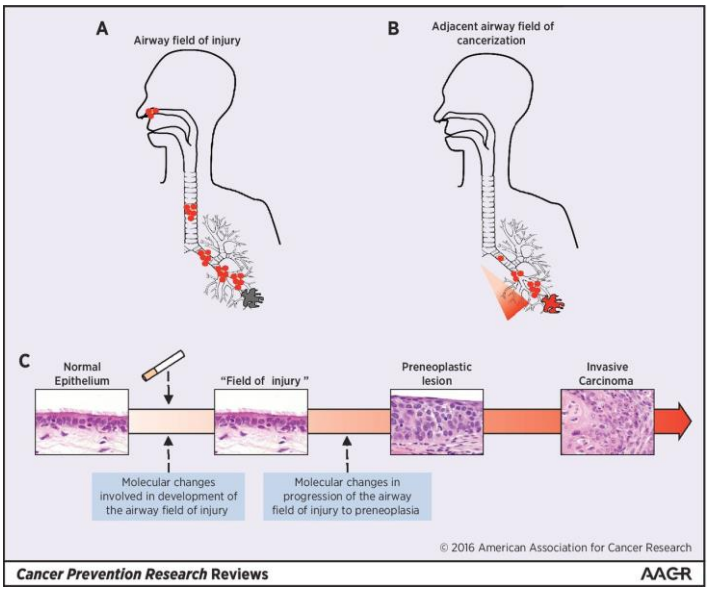

Figure 1-1: Premalignant airway fields and progression of lung cancer. [4]

1.1.2 Cervical Cancer

Cervical cancer is the fourth most frequently diagnosed cancer and the fourth leading cause of cancer death in women worldwide in 2020. Incidence and mortality rates have declined in most areas of the world for the past few decades. However, cervical cancer is the most commonly diagnosed cancer, and the leading cause of cancer death in low and middle income countries (LMIC), where geographic variation is primarily due to differences in the availability of screening. [1]

The human papillomavirus (HPV) is a well-established cancer-causing agent that is the cause of nearly all cervical cancers. Most sexually active people will experience an HPV infection, or several of them, in their lifetime. Although most HPV infections can be cleared without intervention, persistent HPV infection can result in precancerous cervical lesions which may eventually progress to invasive cancers as can be seen in Figure 1-2. With regular cervical cancer

screening and appropriate follow-up, most precancerous lesions can be detected and treated in time to prevent progression to invasive disease. [5] Only comprehensive cervical screening programs have prevented an epidemic of cervical cancer. Therefore, it is important that HPV vaccination and cervical screening be implemented in order to overcome the present international disparities in cervical cancer burden. [6]

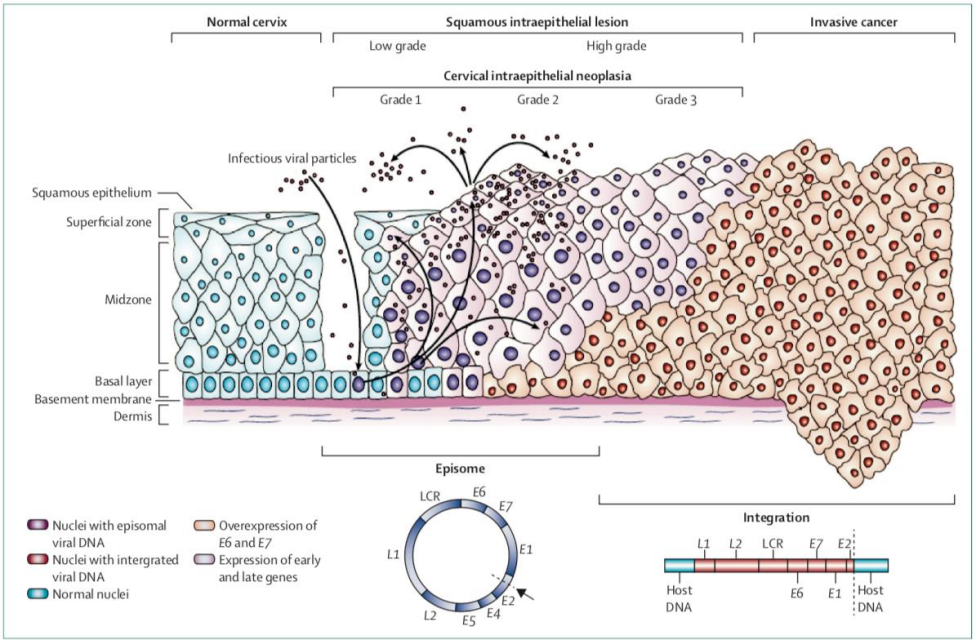

Figure 1-2: Cervical squamous epithelium and cervical cancer progression [6]

1.2 Screening and Diagnostic Techniques

1.2.1 Lung Cancer Screening and Diagnosis

The initial screening method for centrally-located early lung cancers is sputum cytology. In addition, white light bronchoscopy (WLB) is used to directly examine the central airways. However, both sputum cytology and WLB have limited success and provide low sensitivity for detecting early-stage lung cancers in the central airways. Autofluorescence bronchoscopy (AFB)

is able to detect abnormal lesions that cannot be picked up with WLB and has improved the detection of preinvasive and malignant endobronchial lesions. [3]

Computed tomography (CT) can detect smaller peripheral lung lesions than sputum cytology and/or WLB. There have been extensive efforts to improve peripheral lung lesion screening using low-dose computed tomography (LDCT). There has been a dramatic 20% relative decrease in lung cancer mortality when LDCT chest screening is used on high-risk groups such as former or current heavy smokers. However, it is unlikely that this screening method will benefit those in LMIC countries in the near future due to the infrastructure, technical expertise and cost involved. [2]
Suspicious pulmonary nodules detected with CT/LDCT should be biopsied and evaluated based on the collected histological and/or cytological samples. However, as peripheral lung nodules are difficult to locate and biopsy, there exists a need for targeted biopsy approaches. Presently, there are two methods used for sample collection based on the location of nodules: transthoracic needle aspiration biopsy (TNAB) and transbronchial lung biopsy. TNAB uses a CT-guided needle inserted through the pleura to the nodule of interest; it has high diagnostic yield (~90%) but associated with a relatively high risk of pneumothorax. Transbronchial lung biopsy uses an endoscope inserted through the airway to the bronchi nearest to the nodule and is safer if the nodule is accessible through a bronchus, however it has a lower diagnostic yield of 60% to 70%. [3],[7],[8]
A relatively new bronchoscopic modality using radial probe endobronchial ultrasound (RP-EBUS) is used to improve nodules localization by bronchoscopy in order to obtain a biopsy from early lung cancer arising in the peripheral lung fields. Although RP-EBUS has proven to be safer and a powerful technique in visualizing solid large nodules, it has a lower diagnostic yield to detect sub-solid or small pulmonary nodules. Their relatively large probe diameter of 1.4 mm limits their

access to small peripheral airways. [3],[7],[8] Therefore, there is a clinical need for small probes in order to localize and guide sample collection in the peripheral airways.

1.2.2 Cervical Cancer Screening and Diagnosis

Persistent HPV infection can result in precancerous cervical lesions as well as invasive cervical cancer. With regular cervical cancer screening and appropriate follow-up, most cervical cancer precursors can be identified and treated in time to prevent progression to invasive disease. Routine screening for early detection of cervical cancer and precancerous lesions is recommended starting at 21 years of age, continuing through 65 years of age. Available screening tests include conventional and liquid-based cytologic tests such as Papanicolaou (Pap) smear tests and testing for high-risk HPV. An abnormal result from either test should prompt a follow-up colposcopy appointment and biopsy. [5]

Colposcopy uses a mounted magnifying lens to visualize the cervix. The colposcope has white light to visualize lesions and allows the clinician to identify and biopsy areas of interest. Acetic acid may also be used as a contrast agent when applied to the surface of the cervix using a cotton swab and causing dysplastic tissue to turn white through a process called acetowhitening. [6] As a result of the altered nuclear morphology, optical density, and changes in chromatin texture in dysplastic tissue, acetic acid increases the mean scattering coefficient and makes abnormal tissue appear whiter. Diagnosis is made through histologic evaluation of the tissues obtained via biopsy or excision, which determines further treatment decisions and clinical management. [5][9]

1.3 Potential Optical Imaging Technologies for Cancer Screening

An imaging modality that enables non-invasive, real-time imaging of both three-dimensional (3D) cellular resolution tissue morphology as well as assessment of depth resolved involvement could significantly improve cancer screening, treatment and monitoring. Optical imaging techniques have previously been applied to detect early stage cancers based on structural or functional imaging of biological tissue: morphological changes in the tissue may change the light-tissue interaction in terms of absorption, scattering, or polarization; chemical changes in the tissue may change the spectral response as the suite of endogenous fluorophores is altered. [10]

Different optical imaging modalities have been applied to lung and cervical cancer screening including optical coherence tomography (OCT) [11][12][13][14][15], fluorescence or autofluorescence imaging (AFI) [16][11][17], confocal microscopy [16][18][19][20], multiphoton microscopy (MPM) [21][22] and photoacoustic imaging (PAI) [23][24]. Some of these techniques such as confocal, MPM, and fluorescence enable high axial and transverse resolution (≤1 μm) imaging but have limited penetration in biological tissue; some of these image modalities are also limited with respect to navigation or rapid, large-area visualization for *in vivo* clinical implementation. OCT is an emerging, non-invasive optical diagnostic imaging modality, which enables *in vivo* cross-sectional visualization of the microstructure in biological tissue. OCT is able to provide cross-sectional images comparable to H&E histopathology slides of biopsied tissue . [25]

Although biopsy and histopathology remain the gold standard for cancer diagnostics, this diagnostic paradigm is costly: it does not allow for real-time assessment, and can suffer from unacceptable false-negative rates because of sampling errors. A non-invasive, real-time optical

imaging modality could allow for *in vivo* assessment of tissue and could guide biopsies to ensure they are collected at the site of interest. This is particularly important in LMIC countries where it would be more effective for patients to be biopsied and treated during a single visit. There is an unmet clinical need for tools that localize and guide sample collection for early cancer diagnosis, and we suggest that optical imaging modalities may be able to meet this need.

1.3.1 Autofluorescence Imaging

Autofluorescence (AF) imaging (AFI) detects the emission of light from endogenous fluorophores that have been illuminated with excitation light (typically but not exclusively blue 400–480 nm). AFI can probe biological fluorophores such as collagen, elastin, and nicotinamide adenine dinucleotide phosphate. The quantity and distribution of fluorophores *in situ*, as well as the morphology of their environment, determines the intensity and spectrum of tissue AF. Fluorescence provides insights into tissue biochemistry, identifying areas of increased metabolic activity. These areas of increased metabolism show decreased fluorescence. Changes in the intensity and spectral distribution of tissue AF can be used as a distinction between normal and abnormal tissue. Fluorescence of normal tissue reflects subepithelial components such as collagen, elastin, flavins and nicotinamide adenine dinucleotide (oxidized and reduced forms) and appears green under blue illumination. In contrast, fluorescence of abnormal tissue appears darker and slightly brown while high-grade dysplasia and preinvasive or cancerous lesions appear red-brown. In a dual modality configuration where AFI is combined with a volumetric imaging technique such as OCT, it may enable the detection and characterization of functional and structural features associated with multiple biomolecules that are known cancer signals simultaneously. [3][26][27][28]

1.3.2 Optical Coherence Tomography

OCT was first developed by Fujimoto's group at MIT in 1991 [29], and the method has since made a rapid transition from research and development into the clinical setting. OCT has been a valuable clinical imaging modality as it provides high resolution and cross-sectional tomographic imaging of the internal microstructure of biological tissue by measuring back-reflected or backscattered light. Imaging can be performed *in vivo* and in real time. OCT imaging is similar to ultrasound imaging, but uses light instead of sound which allows for resolutions 10 to 100 times higher at the cost of much shorter penetration depth. In most biological tissues, OCT can detect cellular and microarchitectural features with a resolution of 1 to 15 μm and a penetration depth of about 2 mm. [25][30]

Since the invention of OCT, it has been extensively applied in ophthalmology settings and has become a standard of care for diagnosis of ophthalmic diseases. OCT has also been applied in cardiology for the measurement of atherosclerosis plaques. OCT has been investigated in other clinical fields such as dermatology, endoscopy, dentistry and oncology for early cancer diagnosis in skin, lung, esophagus, stomach, colon, oral cavity and cervix, . [25][30][31]

OCT produces an image by measuring the echo time delay of reflected light using low-coherence interferometry. Time domain OCT (TD-OCT) systems were the original implementation of OCT imaging. Figure 1-3 shows a schematic diagram of a simple Michelson interferometer TD-OCT system. It detects the interference between the backreflected or backscattered light from the sample and reference arms. The interference fringes in the sample will only be visible near zero optical path difference (OPD) between the sample and reference arm. A TD-OCT system physically scans the mirror in the reference arm to change its optical path length (OPL), which effectively scans the

location of zero OPD through the sample. This creates a depth profile as a function of time. Each scan of the mirror creates a single depth profile known as an A-scan which is detected by a single photodiode detector on the detection side. TD-OCT systems are limited in scanning speed by the speed at which the reference mirror can be scanned. [25][30][31]

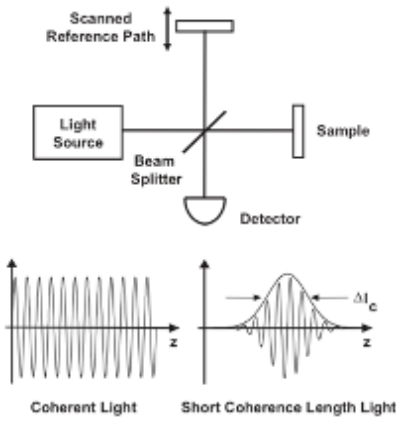

Figure 1-3: Low-coherence interferometry. Schematic showing how low-coherence interferometry works. Backreflected or backscattered light is interfered with light that travels a scanning reference path delay.

There has been a general shift in the method by which researchers implement OCT imaging which is an alternate implementation of OCT known as Fourier domain OCT (FD-OCT). There are two types of Fourier domain detection. One approach, known as swept source domain OCT (SS-OCT), uses an interferometer with a narrow-bandwidth, frequency-swept light source, and detectors which measure the interference output as a function of time. The second approach, known as spectral domain OCT (SD-OCT), uses a broad-bandwidth light source and detects the interference spectrum from the interferometer, using a spectrometer and a high speed, line scan camera. [25][30]

FD-OCT is an alternative approach for A-scan generation that eliminates the need for a scanning reference mirror. In FD-OCT systems, the interference pattern is sampled on the detector in wavenumber instead of detecting the full spectrum of the source simultaneously. There is a relationship in Fourier space between the interference pattern sampled in wavenumber and the depth location of scatterers creating the interference pattern. An inverse Fourier transform can be applied to the spectrally sampled interference pattern to generate an A-scan.

The interference pattern can be spectrally sampled either on the source side or detection side. In the first approach, a frequency scanning light source such as a swept source laser can be used. Swept source lasers have a very small instantaneous bandwidth that sweeps through the laser's full bandwidth as a function of time in high frequency.. In this configuration, called SS-OCT, the detector is simply a photodiode. In the second approach, detection sampling is typically done by using a grating to spectrally distribute the signal onto a line detector. This approach is typically referred to as SD-OCT. SD-OCT acquires the entire signal in a single exposure.

FD-OCT has demonstrated a clear sensitivity advantage over TD-OCT. This increased sensitivity provided by SD-OCT can be leveraged to attain a higher OCT scan acquisition rate, greater depth penetration, or a boost to the sensitivity of the various functional OCT methods. Using state of the art Fourier domain lasers for SS-OCT or detectors for SD-OCT allows for video-rate 3D imaging.

In this section, the primary types of OCT architecture are summarized in terms of how they generate an A-scan. The type of OCT system will determine the necessary type of detector and light sources as well as establish general speed and sensitivity ranges. In order to build an optical probe OCT system, a few additional system characteristics need to be considered. The central wavelength and bandwidth of the source will determine the axial resolution. However, the light-

tissue interactions are also essential to consider in the choice of wavelength, as this will impact penetration depth. The distal optics in the sample arm will determine lateral resolution and scanning geometry for image reconstruction.

1.3.2.1 Transverse Resolution and Depth of Field

The distal focusing optics determine transverse resolution, depth of field (DOF) and scanning geometry. The diffraction limited spot size of the focused optical beam determines the transverse resolution, which is inversely proportional to the numerical aperture (NA). The transverse resolution Δx is: [25]

$$\Delta x = 0.64 \frac{\lambda_0}{NA} \quad (1.1)$$

where λ_0 is the center wavelength of the beam. High transverse resolution can be obtained by using a large numerical aperture that focuses the beam to a small spot size. However, there is a trade-off between increased transverse resolution and decreased DOF. The transverse resolution is related to the DOF via the confocal parameter b, which is two times the Rayleigh range (z_R): [25]

$$b = 2z_R = \frac{\pi \Delta x^2}{\lambda_0} \quad (1.2)$$

Thus, increasing the transverse resolution produces a decrease in the DOF. In general, OCT imaging systems use low numerical aperture-focusing optics to allow for a large DOF.

It is also possible to perform OCT with high NA-focusing optics and achieve high transverse resolutions, which is called micro-OCT. Micro-OCT has the advantage of achieving extremely high transverse image resolution, on the order of 1–2 μm, and allows for cellular level examination

of tissue. However, this results in a decreased DOF. If very high transverse resolution imaging is desired, then it is more efficient to perform *en face* imaging, rather than cross-sectional imaging because of the limited DOF. However, using a non-diffractional beam like a Bessel beam would improve DOF compared to a Gaussian-shaped spectrum. [32] Recently, a new technique known as few-mode interferometry micro-OCT has been developed which overcomes the DOF limitation of conventional high NA objectives and enables cross-sectional cellular-resolution with significantly extended DOF (EDOF). This technique is based on mirror-tunnel optical probe design (single mode fiber (SMF) to multimode fiber (MMF) to focusing optics) that generates coaxially focused modes has been shown to enable EDOF for endoscopic micro-OCT applications. A MMF as a circularly cylindrical waveguide is placed at the output of a SMF. The waveguide wall reflects the SMF output light an angle-dependent number of times, creating multiple coaxial propagation modes. Each mode diverges and is focused by a lens to a mode-dependent focal depth. [33][34][35] Figure 1-4 shows the principle behind the mirror tunneling effect.

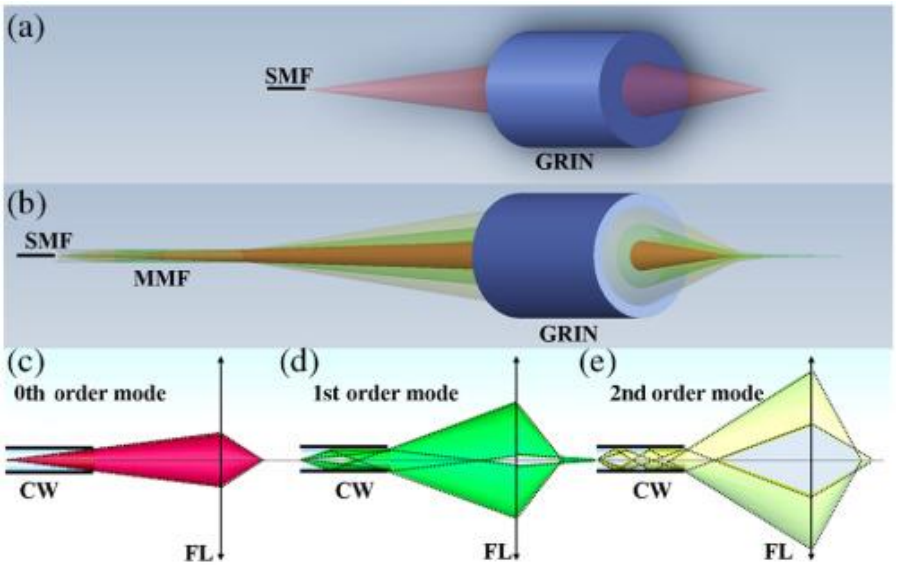

Figure 1-4: (a) Schematic of a conventional single spatial mode and focus. (b) The schematic of multiple spatial modes focused at different distances from the lens. (c), (d), and (e) show the marginal ray tracing for the 0th-, 1st-, and 2nd-order mode of the CAFM beam, respectively. SMF: single-mode fiber; MMF: Multimode fiber; GRIN: graded index lens; CW: circular waveguide; FL: focusing lens. [33]

1.3.2.2 Axial Resolution

In OCT imaging, axial resolution is independent of the beam focus and spot size. Axial resolution is a result of coherence gating, which is defined by the coherence length of the light source. For a light source with a Gaussian spectrum, the coherence length and therefore the axial resolution is given by:

$$\Delta z = l_c = \frac{2ln2}{\pi}\frac{{\lambda_0}^2}{\Delta\lambda} \quad (1.3)$$

where Δz is axial resolution or the full width at half maximum (FWHM) of the autocorrelation function, l_c is coherence length, Δλ is the FWHM of the power spectrum, and λ_0 is the center wavelength of the light source. Figure 1-5 shows a plot of axial resolution vs. bandwidth for light sources at different wavelengths. Since the axial resolution is inversely proportional to the bandwidth of the light source, broad bandwidth light sources are required to achieve high axial resolution.

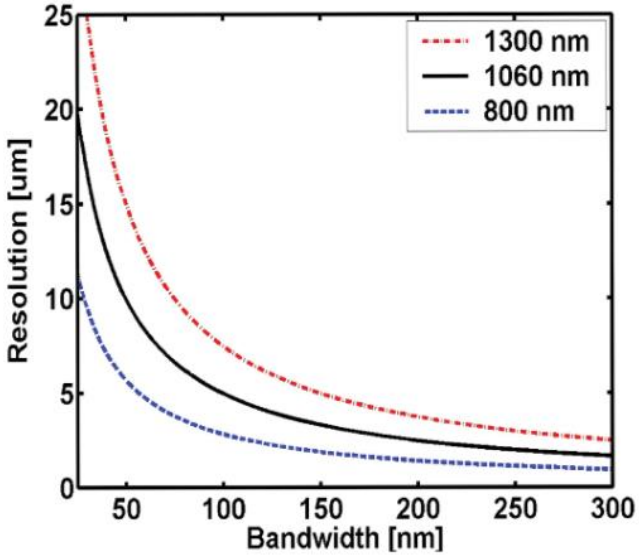

Figure 1-5: Axial resolution vs. bandwidth of light sources for center wavelengths of 800, 1,000, and 1,300 nm.

1.3.2.3 Light Tissue Interaction

For biological applications of OCT systems, the system's wavelength must minimize absorption and scattering to maximize imaging depth. Figure 1-6 shows the optical properties of chromophores as a function of wavelength, demonstrating that absorption is minimized between 700 and 1300 nm for biological tissues, where the scattering coefficient is often decreased with wavelength. OCT research has concentrated on the wavelengths around 800nm known as visible

OCT (vis-OCT) and 1300 nm known as NIR-OCT because of the light sources available. Scattering coefficients of biological tissue dominate light propagation in tissue. Although absorption is lower at 800nm than at 1300 nm, scattering is higher in biological tissue; the higher scattering coefficients provide better imaging contrast while decrease imaging depth. Another factor that influences wavelength choice is resolution. In general, systems with shorter wavelengths have better resolutions at the cost of reduced penetration depth. [12][34][28][35]

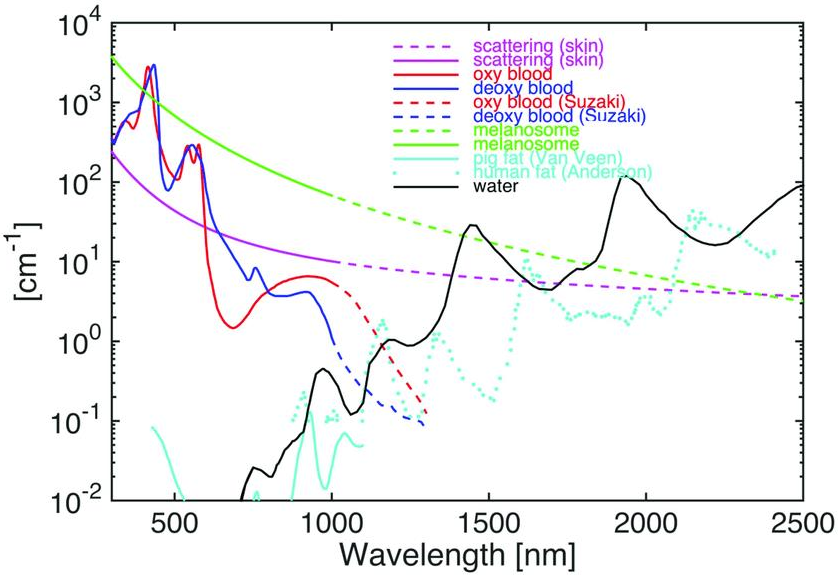

Figure 1-6: Absorption coefficient spectra of chromophores (water, oxygenated hemoglobin, deoxygenated hemoglobin, melanin, and fat) as a function of optical wavelength. [34]

Conventional OCT uses NIR light sources around 1300 nm where imaging depths of 1-2 mm in tissue are typical. Recent technological advancement in supercontinuum light sources has facilitated the development of vis-OCT for biomedical applications, which can achieve much higher resolution than NIR-OCT with comparable spectral bandwidth. [12][28] There is a trade-off in a greater tissue penetration depth at 1300 than at 800 nm compared to higher resolution.

1.3.2.4 Scanning Geometry and Fiber-Based Implementation

In order to reconstruct an image, the OCT beam must be scanned relative to the sample. By scanning the focused beam of the sample arm in a direction orthogonal to the A-line axis, a two-dimensional (2D) cross sectional image of the sample can be created known as a B-scan. By additionally scanning in a third axis orthogonal to both the optical axis and B-scan axis, a 3D volume can be reconstructed.

Flexible imaging probes such as catheters and endoscopes are particularly relevant to clinical applications as they allow for minimally or non-invasive access to internal structures without requiring significant increases in penetration depth. However, endoscopic applications impose size limitations which can make implementing scanning mechanisms challenging. Both side- and forward-viewing OCT endoscopes have been developed for various applications. [25][28]

A side-viewing approach, such as shown in Figure 1-7a, is preferred to image luminal organs such as the airways, coronary arteries, fallopian tube and esophagus. For side-viewing geometries, the scanning axes can typically be decomposed into rotational and longitudinal axes. A small rigid probe can easily be rotated 360 degrees to create a circular B-scan. Then the probe can be longitudinally pulled back between B-scans to create a 3D volume image. A spiral scan pattern provides Nyquist sampling of the tubal wall. In order to perform spiral scanning, the system must continuously rotate the beam while being slowly longitudinally pulled back.

One approach is to proximally rotate the optical probe using a fiber optics rotary joint on the proximal end of the sample arm (Figure 1-7b) thereby allowing the sample arm distal to the joint to freely rotate inside the endoscope while leaving the fiber on the proximal side of the joint

stationary. This approach is easy to implement and allows for small endoscopic optical probes; however, it often suffers from non-uniform rotational distortion (NURD) artifacts due to the tortuous passage taken to reach the region of interest in the body. [36][37][38][39][40] The twists,turns and friction within the walls of the sheath encapsulating the fiber probe create these artifacts, hence there is a need for correction of these NURD artifacts to accurately reconstruct the imaged tissue.

A second approach is distal scanning of the optical beam by attaching an angled mirror or prism to a micromotor placed on the distal tip of the endoscope to divert the beam sideways out of the probe (Figure 1-7c). This has the advantage of isolating the rotation from the fiber and focusing optics which could decrease the NURD artifacts; however, it requires a slightly larger diameter probe and the electronic connections to the motor may obscure the beam over a partial range of the full rotation.

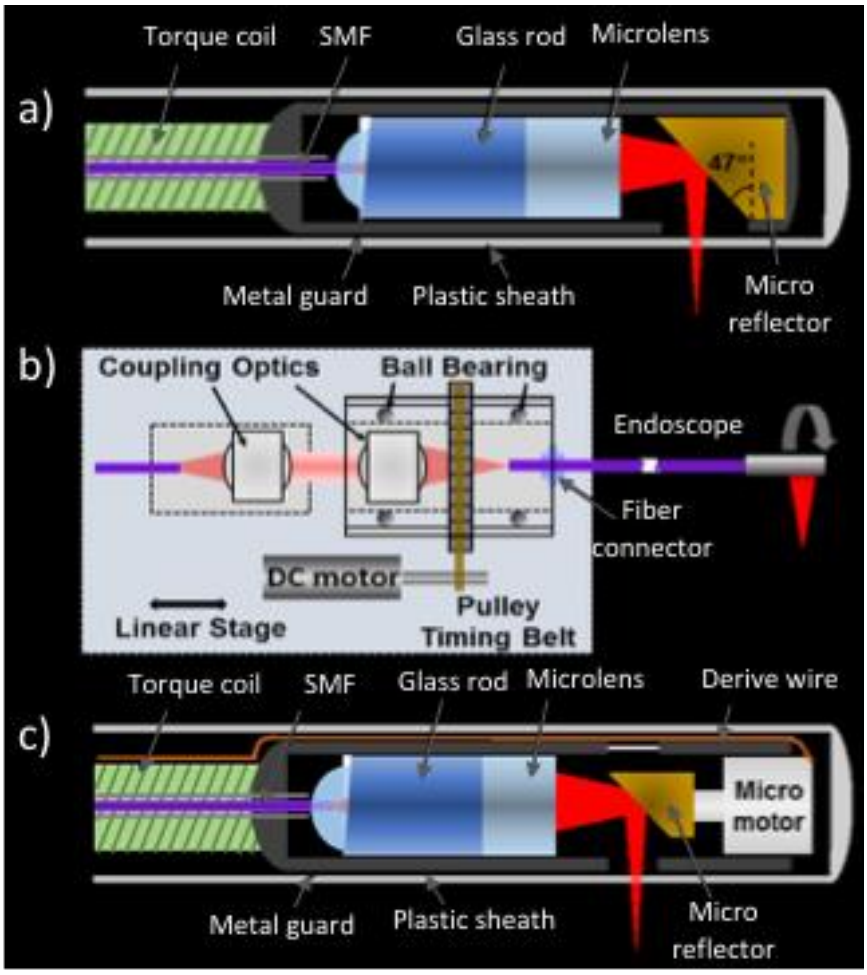

Figure 1-7. Schematics of (a) side-viewing OCT endoscope; (b) proximal scanning with a fiber-optic rotary joint. 3D imaging is performed by pulling back the rotating endoscope; (c) distal-scanning endoscope with a micromotor [41]

Not all clinical applications benefit from side-viewing approaches. Large, nontubular organs such as the stomach and ectocervix benefit from forward-viewing endoscopes that are compatible with traditional screening views. Scanning mechanisms for forward-viewing endoscopes are most commonly micro-electromechanical systems (MEMS) mirrors and scanning fiber endoscopes (SFE).

MEMS mirrors used in this application can be a pair of very small tip and tilt mirrors that provide raster scanning. MEMS devices have been demonstrated for OCT scanning in forward viewing endoscopes which are considerably larger in diameter or of rigid length.

SFE makes use of the mechanical resonance frequency of a fiber for scanning. As shown in Figure 1-8, a fiber is placed inside a quartered piezoelectric tube with the fiber fixed to one end. A cantilevered length of fiber then extends from the fixed location. The fiber can be oscillated by driving a voltage across one axis of the piezo tube at the mechanical resonance frequency of the fiber. Since the quartered piezo tube has two axes, the oscillation frequencies sent to each axis can be independently controlled to create scanning geometries. Two sinusoidal waves with 90 degree phase offset and equal amplitude will cause the fiber tip to oscillate in a circle. A spiral oscillation of the fiber is generally induced by driving the electrodes on the opposite side with opposite polarity and amplitude-modulated voltage. The voltage of adjacent electrodes has to be shifted by 90 degree to excite a circular movement. SFE-based designs have been demonstrated in endoscopes with outer diameters as small as 1.2 mm. The technology is particularly appealing as it can be adapted for both single-channel multi-modality imaging. [25][28][41][42][43][44]

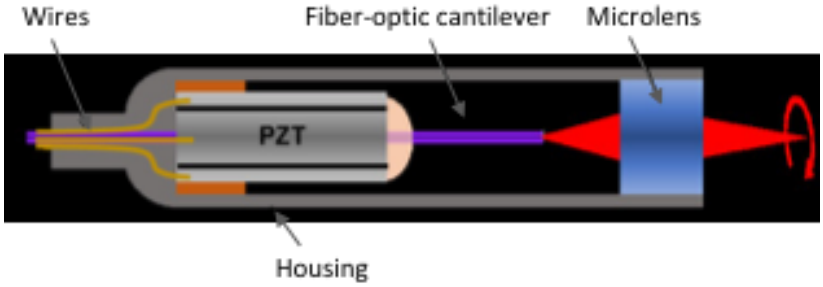

Figure 1-8. Schematics of forward-viewing endoscope. [41]

1.4 Thesis Overview

Cancer is a leading cause of death worldwide. In order to improve the survival rate and reduce the mortality rate, the unmet clinical need for early cancer diagnosis techniques must be filled. As such, this research project seeks to improve the capabilities of OCT for *in vivo* detection and localization of early cancers. Presented are processing methods to improve OCT through the correction of motion-induced artifacts, an assessment of the utility of a recently developed high resolution OCT in distinguishing *ex vivo* precancerous cervical lesions, designs for clinical imaging probes required to transition high resolution OCT to an *in vivo* setting, and an assessment of the suitability of a novel light source for such a high-resolution OCT system.

In **chapter 2**, I develop a new method for the correction of motion artifacts in OCT-AFI obtained by a proximally driven rotary pullback probe. Motion artifacts in pulmonary OCT-AFI are estimated from both modalities, and motion compensation is applied to reduce the impact of the artifacts on the reconstructed volumes. Performance of the algorithm is evaluated on images generated from motion phantoms and *in vivo* OCT-AFI of peripheral lung airways.

In **chapter 3**, I quantitatively evaluate the motion correction algorithm developed in chapter 2. I simulate motion artifacts which have been observed in the OCT and AFI in chapter 2. These simulated artifacts are applied to a motion-free image to allow comparison of a motion-corrected image to its original motion-free image. A metric is defined to quantitatively evaluate this corrected image and the performance of the correction method.

In **chapter 4**, I evaluate the application of a micro-OCT benchtop system to identify cervical lesions for early diagnosis and guided biopsy. I conduct a pilot study of micro-OCT imaging for

detection of invasive and pre-invasive cervical cancers. The *ex vivo* micro-OCT imaging of cervical samples is compared to the corresponding histopathology. Sensitivity, specificity and accuracy of this diagnostic method is assessed.

In **chapter 5**, I design a micro-OCT probe for *in vivo* cervical imaging, a necessary step for clinical translation of the benchtop micro-OCT system described in chapter 4. I present designs for a forward-viewing micro-OCT probe which will enable *in vivo* imaging of the ectocervix. This design uses a piezoelectric tube to generate the forward-viewing scan pattern. The optical design is modelled with Zemax, and analyzed for image quality and beam characterization. Chapter 5 investigates the potential of this probe and characterizes its performance for micro-OCT imaging.

In **Chapter 6**, I evaluate a supercontinuum light source supplied by Hamamatsu for a micro-OCT instrument operating in the NIR region (1300 nm). The performance of this source is compared against a supercontinuum light source from NKT Photonics at 800 nm, which is used in the micro-OCT system in chapter 4. An optimum amplifier current is identified for this source. The coherence length of the Hamamatsu source is measured to characterize the light source for micro-OCT imaging and compared to the NKT source. OCT of biological tissue is obtained using the Hamamatsu source and compared to NKT images for evaluating the anticipated deeper imaging depths.

Chapter 2: Motion Correction for Endoscopic OCT and AF Images

I have published a version of this chapter in the Journal of Biomedical Optics, 23(1). [45]

2.1 Introduction

Successful application of catheter-based OCT and AF imaging for *in vivo* pulmonary imaging requires overcoming several challenges including motion artifacts associated with the cardiac cycle, breathing, and NURD, that make identification of structures like blood vessels difficult[46]. Cardiac and breathing motion artifacts are more prominent when the heartbeat and respiratory periods are much shorter than the total data acquisition time. However, the artifacts can be reduced to some degree by decreasing the image acquisition time, but even then, there remains a need to compensate for NURD. Catheters using micromotors to directly rotate the optical assembly are expected to have less severe NURD compared to proximally-driven torque cable catheters;[37] however the miniaturization of these catheters to access the narrowest organ sites is limited by the relatively large size of the motor. Moreover, due to the difficulty in fabricating perfectly balanced micromotors, NURD can still degrade image quality.

Understanding and correcting motion artifacts may improve image quality and subsequent interpretation. Several techniques have been proposed to correct NURD in catheter-based OCT systems. Structural landmarks, or fiducial markers involving extrinsic objects, have been used to register successive frames [37][47]. Reflections from the sheath or optical components of the catheters can also be used for correcting rotational fluctuations caused by NURD[48]. In other studies, adjacent A-lines or frames have been registered by maximizing cross correlation between the speckle in adjacent search regions[46],[40]. Another method measures the rotational speed of

a catheter by determining the statistical variation in the speckle between adjacent A-lines[49]. However poor tissue apposition regions can result in inaccurate rotational speed interpolation. Yet, methods using cross correlation or phase information may be more sensitive to speckle noise, and generally require highly correlated A-line data. Finally, some methods require disabling the pullback entirely [40][48].

In this work, the motion artifacts in pulmonary OCT-AFI data sets are estimated from both AFI and OCT images based on azimuthal registration of slowly varying structures in the 2D *en face* image or the calculated *en face* image of a 3D image data set. These estimations can be used to correct or reduce such artifacts. We present a new method called azimuthal *en face* image registration (AEIR) for motion correction that is applicable to any 2D or 3D rotational catheter data with repeating angularly-varying values that correlate with physical structures. Performance of the algorithm is evaluated on images generated from NURD phantoms, *in vivo* OCT-AFI datasets of peripheral lung airways, and known images with simulated artifacts.

2.2 Materials and Methods

2.2.1 Imaging Systems

The OCT-AFI system used in this study has been previously described[7]. Briefly, the OCT subsystem employs a 50.4 kHz wavelength-swept source laser (SSOCT-1310, Axsun Technologies Inc., Billerica, MA, USA) with illumination centered at 1310 nm with a 100 nm bandwidth. The AFI subsystem uses a 445 nm semiconductor laser (CUBE 445-40C, Coherent, Santa Clara, CA, USA). The OCT and AFI modalities are combined into a single double-clad fiber (DCF) catheter. The fiber-optic catheter consists of a length of DCF (9/105/125-20PI, FUD-3489, Nufern, East Granby, CT, USA) spliced to beam-shaping fiber optics (comprised of step-index

multimode, graded-index, and angle-polished no-core fibers). A rotary-pullback drive unit allows volumetric OCT-AFI imaging of airways up to 7 cm in length. The OCT and AFI signals are collected simultaneously and custom data acquisition software collects and processes the data for immediate display.

2.2.2 Phantom and *In vivo* Imaging

The NURD phantom was a 3D printed object that contained eight parallel and evenly spaced targets that were oriented along the imaging path as it is shown in Figure 2-1a-b. Four targets are coated in IR absorbing material for ease of presentation. Deviations from the expected geometry due to NURD could be quantified.[50] This phantom can be created for catheters of various diameters and with complex imaging paths with multiple bends. Figure 2-1c-d show the important feature of the 3D printed NURD phantom which is the path can easily be manipulated to emulate the curves encountered by the imaging tip in actual use. OCT-AF image of this phantom was obtained to enable the identification of NURD artifacts.

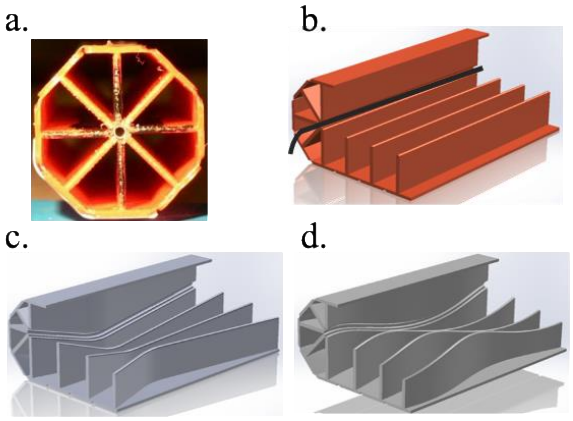

Figure 2-1: NURD phantom. a shows top view of NURD phantom, b shows cross sectional partially unwrapped with straight path, c and d show cross sectional partially unwrapped with curved path.

In vivo pulmonary OCT-AFI imaging of human subjects was approved by the Research Ethics Board of the University of British Columbia and the British Columbia Cancer Agency. Informed consent was obtained from all participants. Participants underwent conscious sedation and local anesthesia was applied to the upper airways. After a flexible bronchoscope was inserted, a fiber-optic catheter was inserted down the instrument channel before optical imaging was performed on an area of interest.

2.2.3 Motion Correction Method

The algorithm proposed here uses strips of length ($W=2w+1$)-pixels centered on each pixel along the rotational direction (p direction) as in Figure 2-2a on the *I(p,f) image* (at the beginning and end of a frame, strips reach into the neighboring *en face* image column to the temporally closest pixels). Each strip $S_{p,f+1}(W)$ from $(f+1)^{th}$ frame is compared to the corresponding $(2n+1)$ strips from the previous pullback frame f, ($S_{p-n,f}(W)$, $S_{p+n,f}(W)$); p represents the p^{th} pixel/strips in the *en face* pullback frame and n is a parameter of the algorithm determining the number of strips in the f^{th} column to be compared with them (Figure 2-2b). The strips are compared using the following equation as the measure of similarity to construct the cost matrix:

$$Cost_{f+1}(k,p) = \left(\sum_W (S_{p+k,f}(W) - S_{p,f+1}(W))^2\right)^2 \qquad (2.1)$$

where $k \in [-n, n]$ and $Cost_{f+1}(k,p)$ is the value of the cost matrix at its k^{th} row and p^{th} column between frame $f+1$ and f.

In our method, each frame is corrected one by one, and using the corrected frame as the reference of comparison to correct the next frame. In order to maintain the continuity of a frame to its next frame, the cost matrix for the $(f+2)^{th}$ frame, $Cost_{f+2}(k,p)$, is concatenated to $Cost_{f+1}(k,p)$ to

construct *Cost(k,P)* where $P \in [1,2 \times p]$.This cost matrix is resampled by stretching the vertical *k*-direction with a parameter *s* (to get subline precision) and downsampled along *P* with a parameter *m* reducing noise as well as constraining angle steps. The optimal continuous path through the cost matrix representing motion artifacts, which accounts for the continuous rotation of the catheter, can be found using DP, and then resampled to its original size. Image correction can be applied by reversing the obtained optimal path; pullback columns are aligned by replacing each pixel with one that is shifted based on the obtained path[39]. The same correction is applied to the 3D frames since each pixel in the *en face*-frame corresponds to an A-line in the 3D frame. For this work, all images were processed in MATLAB, and the interpolation methods were specified to use "bicubic" for resizing images and "Pchip" for aligning pixels or A-lines in MATLAB R2014a.

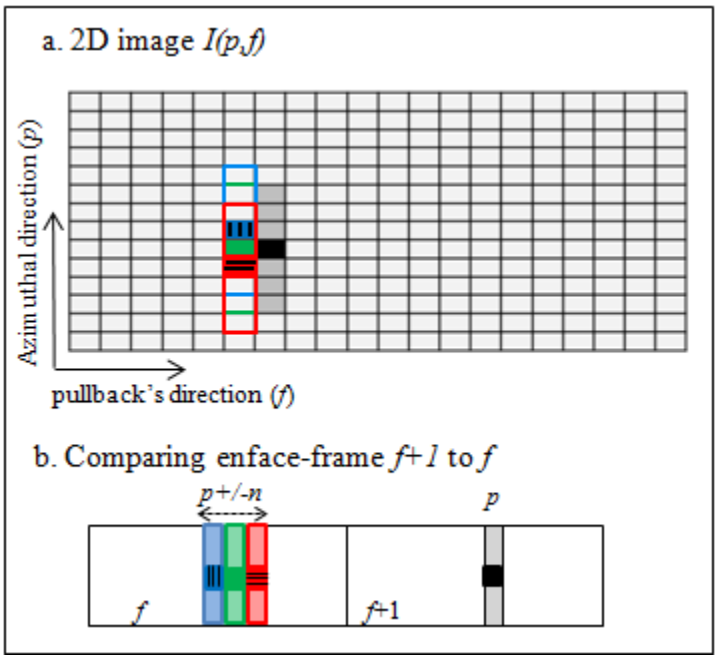

Figure 2-2: A strip of W-pixels centered on pixel *p* along the azimuthal rotation direction on the (*f+1)*th *en face*-frame. It is compared to 2n+1 neighboring strips from the previous

frame *f* to find the correlation between the patterns of pixels for each strip to determine the effect of motion artifacts. (For the example displayed w=3 and n=1, which are colored in blue, green, and red).

For our system, the AFI and OCT images are obtained simultaneously and are therefore subject to the same motion artifacts. For motion correction of 3D OCT images, we can use corrections from either the AFI or *en face* OCT image and apply it to the 3D OCT frames. These two different correction options are denoted as (OCT-AEIR$_{meanProj}$) and (OCT-AEIR$_{AF}$). We have applied our technique to the AFI and OCT images of a NURD phantom and *in vivo* clinical pulmonary images.

Van Soest *et al* [40] previously used dynamic programming for correction of NURD artifacts in OCT images called azimuthal registration of image sequences (ARIS). They used the L2 norm to measure similarity and calculated the cost matrix from full A-lines of OCT frames being aligned. In order to compare the corrections based on full A-lines in the OCT frame and the W-pixel strip in the *en face* image, we also applied a similar method to construct the cost matrix based on full A-lines using Eq. 2.1. The result of the correction from this method is denoted as OCT-ARIS$_{OCT}$.

2.3 Results and Discussion

Performance of the correction methods on the 3D images was visually examined using the *en face* images. Different sets of parameters (w, n, s, m) were evaluated to apply correction where the parameters were allowed to vary between $10 \leq w \leq 100$, $10 \leq n \leq 60$, $1 \leq s \leq 10$, and $1 \leq m \leq 5$ with step size 20 for w and n, and 1 for s and m. The optimal parameters for the OCT-AEIR$_{meanProj}$ method on our datasets were found to be w=20, n=20, s=5, and m=1 based on the visual assessment of correction performance and the average run-time normalized to a per frame value. The correction

parameters were selected to be 20-20-5-1 by considering the run-time. (All subsequent figures in this chapter were processed using these optimized parameters).

The $ARIS_{OCT}$ method also using n, s, and m parameters, was applied on the OCT images with the same parameter as AEIR methods (the optimal parameters were also the same, n=20, s=5 and m=1). Although the optimized parameters were selected as n=20, s=7, and m=4 by Van Soest *et al*[40]., we could not visually detect any difference between the corrected results of these two sets of parameters. To achieve the best correction results for this method, the 3D OCT data also had to be smoothed. We used a 3x3 pixels median filter to do intraframe filtering (along the A-line and azimuthal direction on each frame) and a mean filter of size 5 frames for interframe averaging.

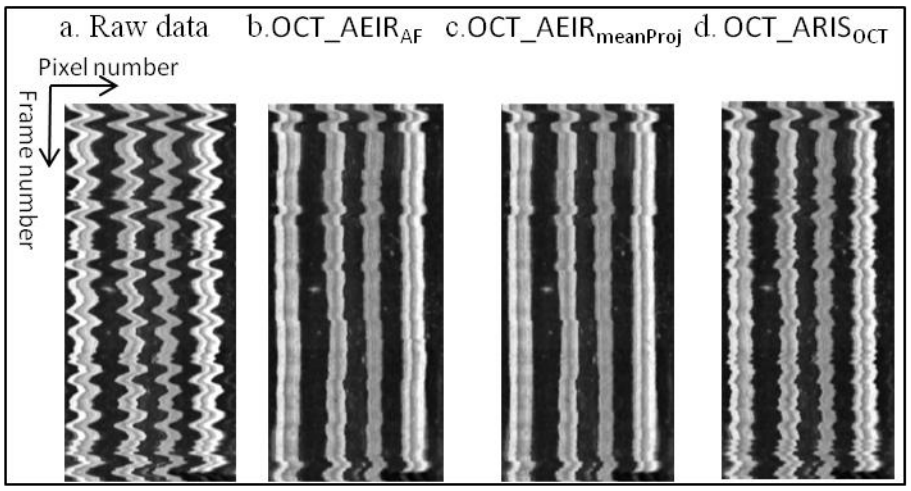

Figure 2-3: Mean *en face* projection for 3D OCT image (pullback rate=0.5mms^{-1}, pullback length=10mm, and frame rate=49fps). (a) original raw OCT image with NURD artifacts, (b) OCT-AEIR$_{AF}$, (c) OCT-AEIR mean$_{Proj}$, and (d) OCT-ARIS$_{OCT}$ methods.

Figure 2-3 compares the results of applying the three correction methods on the same NURD-phantom OCT image; we have presented the mean projection *en face* image of the corrected 3D

images to show the performance of correction methods on the 3D images. As seen in Figure 2-3, motion correction with our technique appears much more effective than the previously published method[40] using full A-lines. Results from OCT-AEIR$_{meanProj}$ and OCT-AEIR$_{AF}$ corrections are comparable to each other. The AF image and *en face* OCT images from the NURD-phantom are similar, so we present only the results applied to OCT images in Figure 2-3.

The AEIR$_{AF}$ method was applied to an *in vivo* 2D AF image in Figure 2-4. This technique demonstrates significant correction of both NURD (as seen by the reduction of the high frequency oscillations in image (b)) and cardiac/breathing artifacts (reduced large lower frequency oscillations). There is noticeable motion correction in Figure 2-4 due to the AF-AEIR$_{AF}$ correction method.

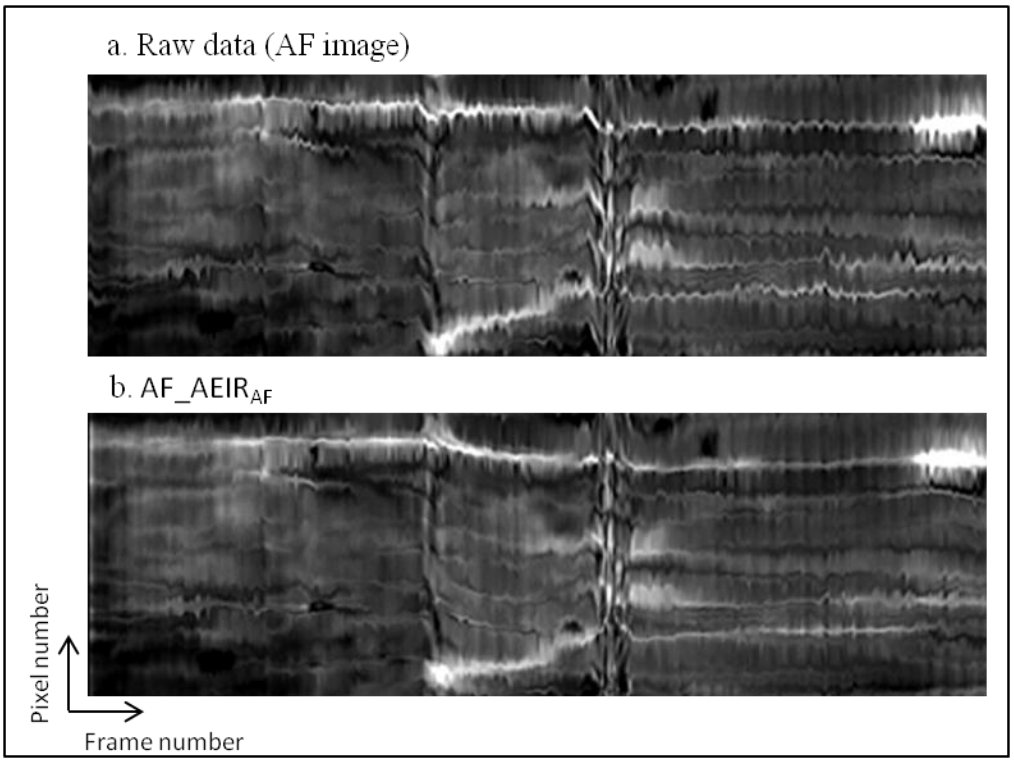

Figure 2-4: AF correction method applied to an *in vivo* 2D AF image (pullback rate=0.2mms-1, pullback length=10mm, and frame rate=12.5fps. (a) raw AF image, and (b) corrected image by the OCT-AEIRAF method.

Results of the three different methods on an *in vivo* 3D OCT image are shown in Figure 2-5. We also present the corresponding AF images with the same corrections as its *en face* OCT counterpart for better visual evaluation. Motion artifacts including NURD cause wavy patterns in the *en face* image as well as deformation of structures. After applying our correction method to the images, it is noticeable that performance of OCT-AEIR$_{AF}$ and OCT-AEIR$_{meanProj}$ are much better for reducing the wavy patterns than using the previously published method on 3D OCT guided by A-line correlations. These techniques demonstrate significant correction of both NURD (as seen by the reduction of the high frequency oscillations in the enlarged orange box in Figure 2-5 sections (b))

and cardiac/breathing artifacts (seen as reduced high-amplitude, lower frequency oscillations in enlarged black box in Figure 2-5 sections (a) and yellow arrow on Figure 2-5 sections (b)).

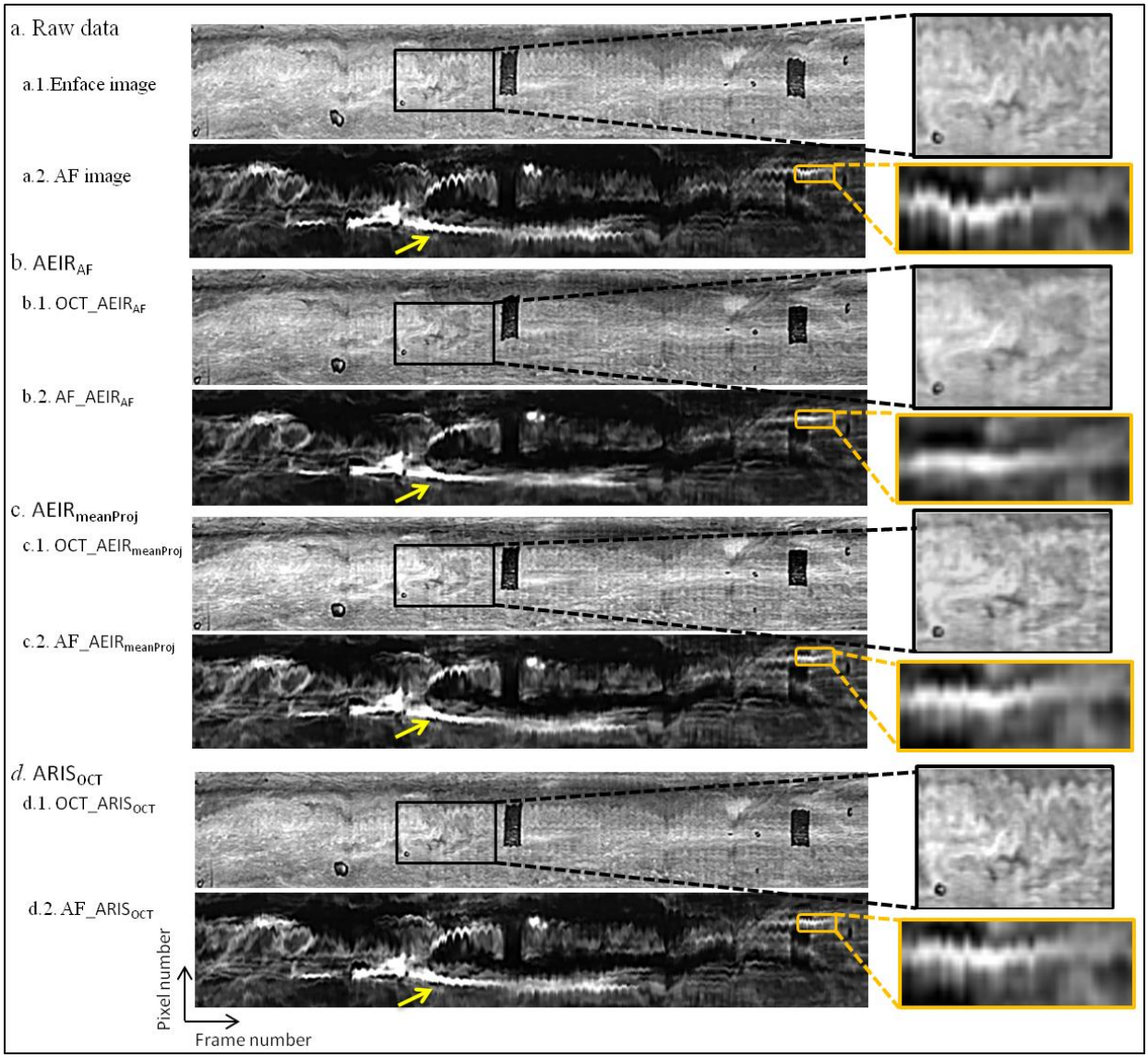

Figure 2-5: *En face* OCT image shows correction of different methods on an *in vivo* image (pullback rate=0.4mms^{-1}, pullback length=30mm, and frame rate=50fps). (a) raw data and (b), (c), and (d) are OCT-AEIR$_{AF}$, OCT-AEIR$_{meanProj}$, and OCT-ARIS$_{OCT}$ methods, respectively. (a.1) and (a.2) are *en face* and AF images obtained simultaneously. The black

box is enlarged for better visualization, and the yellow arrows emphasize on the same regions before and after correction between different methods for cardiac artifacts (frequency ~1-2 Hz). The orange box is enlarged for better visualization of NURD artifacts and its correction.

In Figure 2-6, dashed rectangles are showing where the OCT-AEIR$_{meanProj}$ method seems to have corrected the motion artifact best. The OCT-AEIR$_{AF}$ method did poorly in these areas. The yellow arrows show a region where OCT-AEIR$_{AF}$ did better with correction as there were contrast between structures to find artifacts and its correction.

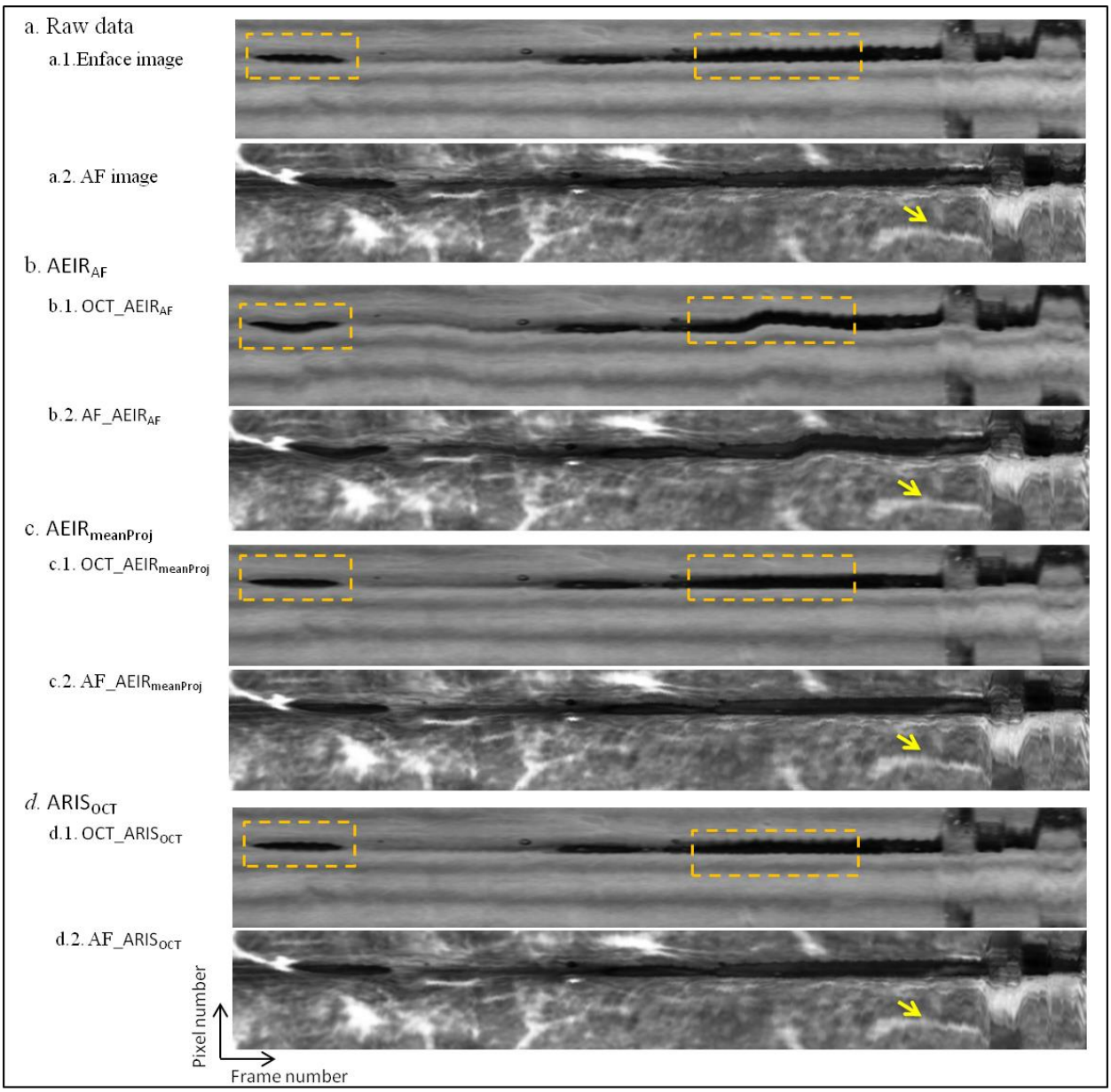

Figure 2-6: *En face* OCT image shows correction for different methods on an *in vivo* image (pullback rate=0.4mms^{-1}, pullback length=30mm, and frame rate=25fps). a) raw data and (b), (c), and (d) are, OCT-AEIR$_{AF}$ OCT-AEIR$_{meanProj}$, and OCT-ARIS$_{OCT}$ methods, respectively. (a.1) and (a.2) are *en face* and AF images obtained simultaneously.

The run-time is the average time required to apply the correction to all frames of one image. The average run-time was 0.10, 0.10, and 0.25 s per frame for OCT-AEIR$_{AF}$, OCT-AEIR$_{meanProj}$, and OCT-ARIS$_{OCT}$, respectively.

Our procedure allows for correcting motion artifacts in rotary-pullback 2D and 3D image modalities along the azimuthal direction. For 3D images, motion artifacts along the radial direction (A-lines) are not detected nor corrected with our method. Our method corrects and aligns images along the azimuthal direction using the mean projection of A-lines for better registration of the calculated cost matrix from *en face* contrast within its strips than the full A-lines data. On the other hand, there are no radial artifacts originating from NURD, but possibly from *in vivo* cardiac and breathing motions, which could be reduced by shorter scan times.

Performance of the correction methods on the *en face* image of 3D images was visually examined and we concluded the AEIR methods are correcting for motion artifacts and improving visual image quality. The OCT-AEIR$_{AF}$ correction performs more artifact removal than the OCT-AEIR$_{meanProj}$ method for images that have strong AF signals. The AF-guided method performs poorly when there is no AF signal from tissue, e.g., lumen. The OCT-AEIR$_{meanProj}$ method needs the *en face* image projection to have structures with good contrast to enable a good correction of motion artifacts. In addition, the correction may be misled when a feature is not parallel to the pullback direction and also when there are no features present (e.g., lumen), artifacts may not be found and corrected.

Van Soest *et al*. applied a DP method to stationary 3D OCT images for NURD corrections and compared full A-lines in B-scans to construct a cost matrix using the L2 norm. However, we used the formula in Eq. 2.1 to construct the cost matrix, which is not a norm, and it more strongly

penalizes cost paths with non-optimal intermediate steps. We have also tried using the L2 and L1 norms to construct the cost matrix; however, our method did not converge on the optimal continuous path using these norms for all images. We have found that comparing full A-lines are not sufficient due to reduced or absent feature correlation between A-lines in the data collected. Motion correction with our technique, using the *en face* contrast within the strips appears much more effective since each strip is a mean projection of W A-lines which were compared to each other. Although the full A-line had more pixels, it was depth information, which was not used for azimuthal registration and motion correction.

In this chapter, I have evaluated the correction methods visually both on *in vivo* images and NURD phantom images. It would be advantageous to quantitatively evaluate each correction methodin order to do comparisons. There is a need to define a metric that can measure the corrections applied on a 3D or 2D rotary pullback image. In the next chapter, I will define a metric to quantitatively evaluate the correction methods and compare their efficiency in correcting *in vivo* images.

2.4 Conclusion

Our method calculated the correction of motion artifacts about 2-3 times computationally faster than the OCT-ARIS$_{OCT}$ method since we were using the *en face* image for correction rather than the full 3D stack/OCT-volume. It may be applied in real time since it only needs two frames, one to be corrected and its previous frame. We have applied this method to multiple pullback catheter images and have shown that our methods can be guided by either OCT-AEIR$_{AF}$ or OCT-*AEIR*$_{meanProj}$ on *in vivo* images. We have concluded that OCT-AEIR$_{AF}$ and OCT-AEIR$_{meanProj}$ can be complimentary to each other when we have both modalities because they may be more effective in different parts of the pullback, and there is a greater likelihood of strong contrast existing in at

least one of the modalities compared to when just one is used. An improved version of this algorithm could conceivably be constructed by making use of correlations in both modalities simultaneously for estimating motion artifacts. In the case of dual modality imaging, e.g., OCT-AFI, these two methods could be combined to provide more complementary and efficient corrections.

Based on our visual evaluation of the corrected images, we conclude that overall OCT-AEIR$_{AF}$ and OCT-AEIR$_{meanProj}$ appear to correct a larger fraction of the visible artifacts than does ARIS$_{OCT}$. Our method allows applying the motion correction to 2D images. Motion corrections of 2D AFI were obtained by the AF-AEIR$_{AF}$ method, and it may be generalized to other 2D images for motion corrections.

Chapter 3: Quantitative Evaluation of Correction Methods

I have published a version of this chapter in the Journal of Biomedical Optics [45] as well as presented it at the Medical Image Understanding and Analysis (22nd Conference) [51].

3.1 Introduction

OCT and AFI systems are often catheter-based for *in vivo* clinical imaging and have been developed for cardiology, gastroenterology, and pulmonology[52],[53],[54],[46],[11]. Successful application of catheter-based systems for *in vivo* imaging is challenging since motion artifacts associated with the cardiac cycle, breathing, and NURD degrade image quality and make identification of biological structures difficult[46]. Cardiac and breathing motion artifacts may be reduced to some degree by decreasing the image acquisition time, but even then, there remains a need to compensate for NURD artifacts. Several techniques have been investigated to correct NURD in catheter-based OCT systems. [46],[37],[47],[48],[49], [40] In Chapter 1, I have developed a correction algorithm to correct these motion artifacts to improve image quality and subsequent interpretation. I have developed a motion correction algorithm in chapter 1 which is called azimuthal *en face* image registration (AEIR), and it is applicable to any 2D or 3D rotational catheter data (for details of the algorithm refer to the previous chapter). [38]

In order to evaluate the motion correction methods, I need a metric for the quantitative assessment of the motion correction methods. One study used the angle standard deviation and fiducials for measuring the angular deviation. [37] In another study, they also used the angle deviation to quantitatively evaluate their own correction method; however their method was applied to 2D OCT images and used standard deviation over the assumed first aligned frame. [40]

In this chapter, I have developed a metric to quantitatively evaluate the motion correction methods developed in chapter 2. I also modeled and simulated the motion artifacts based on the observed artifacts on *in vivo* and NURD phantom OCT and AF images in chapter 2. By applying these simulated motion artifacts on *in vivo* images, I determined the actual artifacts that need to be compensated by the motion correction method. These artificial artifacts may be applied on a ground truth image to create an image with known artifacts. Since there may be some non-visible motion artifacts on the ground truth image, a correction method was applied before adding the simulated artifacts. However, there is no guarantee this process converges to a motion-free scan. It is more likely that the corrected image is distorted dependant on the alignment algorithm. From this stable point, it is expected that the same algorithm, based on the same data, is more likely to return to its previous stable state. The other correction methods, for whom different stable states are expected, have a non-optimal error metric even if no motion artifact is applied, which puts these methods at a disadvantage. Therefore, I have studied the ground truth image used for the quantitative analysis and the tendency of different correction methods on ground truth image on the quantitative metric. I present quantitative evaluations performed on ground truth images of an *in silico* phantom, a NURD phantom and *in vivo* endoscopic pulmonary OCT and AF datasets of peripheral lung airways and applied simulated artifacts.

3.2 Materials and Methods

3.2.1 Phantom and *In vivo* Imaging

The OCT and AFI data in this chapter are similar to the data in chapter 2. Here, I briefly describe the imaging system. A combined endoscopic OCT-AFI instrument using a DCF catheter was used

in this study to collect OCT and AFI signals simultaneously and custom data acquisition software collects and processes the data for immediate display. The OCT subsystem employs a 50.4 kHz wavelength-swept source laser (SSOCT-1310, Axsun Technologies Inc., Billerica, MA, USA) with illumination centered at 1310 nm with a 100 nm bandwidth. The AFI subsystem uses a 445 nm semiconductor laser (CUBE 445-40C, Coherent, Santa Clara, CA, USA). A rotary-pullback drive allows 3D OCT-AFI imaging of airways up to 7 cm in length.[7]

OCT and AF imaging of a NURD phantom and human subjects were collected. The NURD phantom was a 3D-printed object containing eight evenly-spaced parallel features oriented along the pullback direction. It quantifies NURD artifacts during imaging as deviations from the expected geometry.[50] *In vivo* pulmonary imaging of human subjects was performed during flexible bronchoscopy. It was approved by the Research Ethics Board of the University of British Columbia and the British Columbia Cancer Agency.

3.2.2 Quantitative Analysis

In order to quantitatively characterize the correction for each method, I have evaluated the correction using two approaches.

In the first approach, I have quantitatively evaluated the correction on the NURD phantom images. Each image contains 4 gray and black strips that create 8 edges in total. Motion artifacts make the length of the edges longer than an ideal straight edge. I detected the edges in each image and measured their lengths by calculating the Euclidean distance between each pixel along the edge. The measured lengths were normalized by length of an ideal strip with no motion artifacts. The average normalized length (L_N) was calculated for phantom images.

The second approach for quantitative analysis of motion corrections was evaluated on both phantom and *in vivo* images. To perform a quantitative analysis of the amount of correction needed for each image and the amount of correction applied by each of the methods, one needs to know the ground truth image, that is, the starting image without any detectable motion artifacts. A known amount and type of motion artifact is then added to the ground truth image. It is then corrected by the algorithm and the correction adjustments are compared to the known applied artifact. In other words, we need to know the artifacts in the image in order to compare against the applied correction. For this purpose, I have simulated motion artifacts in endoscopic OCT and AF images with frequencies similar to those observed in our NURD phantom and *in vivo* image data sets. I observed motion artifacts in these images to be noisy sinusoidal patterns along the pullback direction with different frequencies depending on the type of artifact; [37],[49], [50], [55] e.g., heartbeat (frequency 1-2 Hz) and breathing artifacts (~0.2Hz) are generated with their respective frequencies, while non-biological NURD artifacts can have high and/or low frequencies as seen in figures in chapter 2 (Figure 2-3-6a).

I created a model to simulate these motion artifacts that consists of a combination of wavelets for each respective type of artifact along the pullback direction. Each wavelet $A_i(f)$ can be calculated simply by placing a Gaussian envelope over a sine wave with the corresponding frequency for each artifact type.

$$A_i(f) = a_i \sin(freq_i \,.\, f) \,.\, e^{\frac{-(f-f_{0,i})^2}{\sigma_i}} \qquad (3.1)$$

where a_i is the amplitude of the artifact to be applied, $freq_i$ is the frequency of the artifact to be applied, f is the position (frame) of the wavelet along the pullback direction , $f_{0,i}$ is the position of artifacts centered along the pullback, and σ_i is the artifacts' length along the pullback direction.

Artifact matrix *A(p,f)* is the same size as the 2D image *I(p,f)*, where each $A_i(f)$ displaces pixel, $p_{i,}$ along the rotation direction, and other pixels in between these displaced pixels are interpolated considering wrapping of each frame to its next frame. This *A(p,f)* is the output of our artificial motion artifact simulation which determines the displacement of each pixel in the ground truth image to generate a ground truth image with artifacts as shown in Figure 3-2 to 3-6 (g). Two simulated artifacts were applied to a NURD phantom, and *in vivo* images as shown in Figure 3-2 to 3-6 (b).

A 3D digital phantom with no artifacts, a NURD phantom, and an *in vivo* image with limited observable artifacts were the ground truth images used in this study. I generated a digital 3D phantom with four circular targets at the same depth in each frame. Each circular target had a different radius and intensity, which is similar in pattern to the NURD phantom's image. For the NURD phantom and *in vivo* image, I chose a scan/pullback with little visible motion artifacts. I applied our OCT_AEIR$_{AF}$ method iteratively to correct for unobservable artifacts (those detectable by the algorithm) until there was little change between corrections. The *en face* (linear mean) projections of the digital phantom, pre-corrected NURD phantom and *in vivo* image were used as the ground truth images. Two simulated artifacts were applied to these images to generate ground truth images with artifacts. These were then corrected using three different correction methods. Each correction method generated a correction matrix (C) representing the artifacts detected and to be corrected. This correction matrix was compared to the artifact matrix to quantitatively evaluate the degree of correction achieved by each of the methods.

Two parameters were defined to quantitatively evaluate the amount of correction each method accomplishes: 1) correlation coefficient (r) and 2) average compensated difference ($\overline{D}_{comp}$). The

correlation coefficient was calculated between the correction and artifact matrixes using the following equation:

$$r = \frac{\sum_f \sum_p (C(f,p)-\overline{C})(A(f,p)-\overline{A})}{\sqrt{(\sum_f \sum_p (C(f,p)-\overline{C})^2)(\sum_f \sum_p (A(f,p)-\overline{A})^2)}} \qquad (3.2)$$

where $C(f,p)$and $A(f,p)$ are the pixel shift values at pixel p of frame f in the correction and artifact matrixes, and $\overline{C}$ and $\overline{A}$ represent the respective matrix averages.

The difference between C and A was defined as the difference matrix (D). In the correction method, each frame was compared with its previous frame thus an error in a frame can propagate to all subsequent frames. To compensate for this possible accumulation of errors and to localize the mistake to its original frame, a subtraction of the previous D frame values was calculated for frame two and above and denoted as the compensated difference matrix (D_{comp}). The average of D_{comp} was named $\overline{D_{comp}}$.

$$D(f,p) = A(f,p) - C(f,p) \qquad (3.3)$$

$$D_{comp}(f,p) = D(f,p) - D(f-1,p)\,, \;\; f \geq 2 \; and \; D_{comp}(1,p) = D(1,p) \qquad (3.4)$$

$$\overline{D}_{comp} = \overline{|D_{comp}(f,p)|} \qquad (3.5)$$

3.3 Results and Discussion

In the first quantitative analysis approach, I calculated L_N (line length) for the NURD phantom images in Figure 3-2, which are reported in Table 3-1.

Table 3-1: Average normalized length for raw image and corrected images with 3 different methods.

	Raw image	OCT-ARIS$_{OCT}$	OCT-AEIR$_{AF}$	OCT-AEIR$_{meanProj}$
L_N	1.599	1.141	1.042	1.036

For an ideal strip L_N= 1, and a L_N closer to one indicates better NURD correction. Using a Student's t test to compare the edge lengths between the four images, I found that all corrections resulted in edge length data (shorter) that was highly significantly different ($p<0.0005$, two-tailed test) from the raw image data. Similarly, the method presented here resulted in edge data that was highly significantly different ($p<0.0005$, two-tailed test, shorter) than the edge length data from the previously published algorithm (OCT). I expect the OCT-AEIR$_{meanProj}$ and OCT-AEIR$_{AF}$ methods have the same correction since the *en face* and AF image for the phantom are similar, however, there is a small difference between them due to differences in their image contrast. The detected edge lengths for the two methods (OCT-AEIR$_{meanProj}$ and OCT-AEIR$_{AF}$) were not found to be significantly different as the t-test p-value was found to be 0.386.

In the second approach, quantitative analyses of motion corrections on the NURD phantom and *in vivo* images were evaluated using two parameters: the correlation coefficient and the average compensated difference. These two parameters together, evaluated the performance of the correction methods. Different artifacts have been applied to the same images, and restoration was attempted with the different correction methods to evaluate reproducibility. Figure 3-1a shows the eight motion artifacts I simulated and then applied to a NURD phantom and an *in vivo* image. These images and applied simulated motion artifacts were then corrected by the three correction methods. Figure 3-1b-c shows the discussed two metrics evaluated on a 3D OCT *in vivo* image

with the eight artifacts. The reproducibility of each method across the eight simulated motion artifacts can be analyzed by comparing the results of the correction methods as seen in the box plots of Figure 3-1b-c.

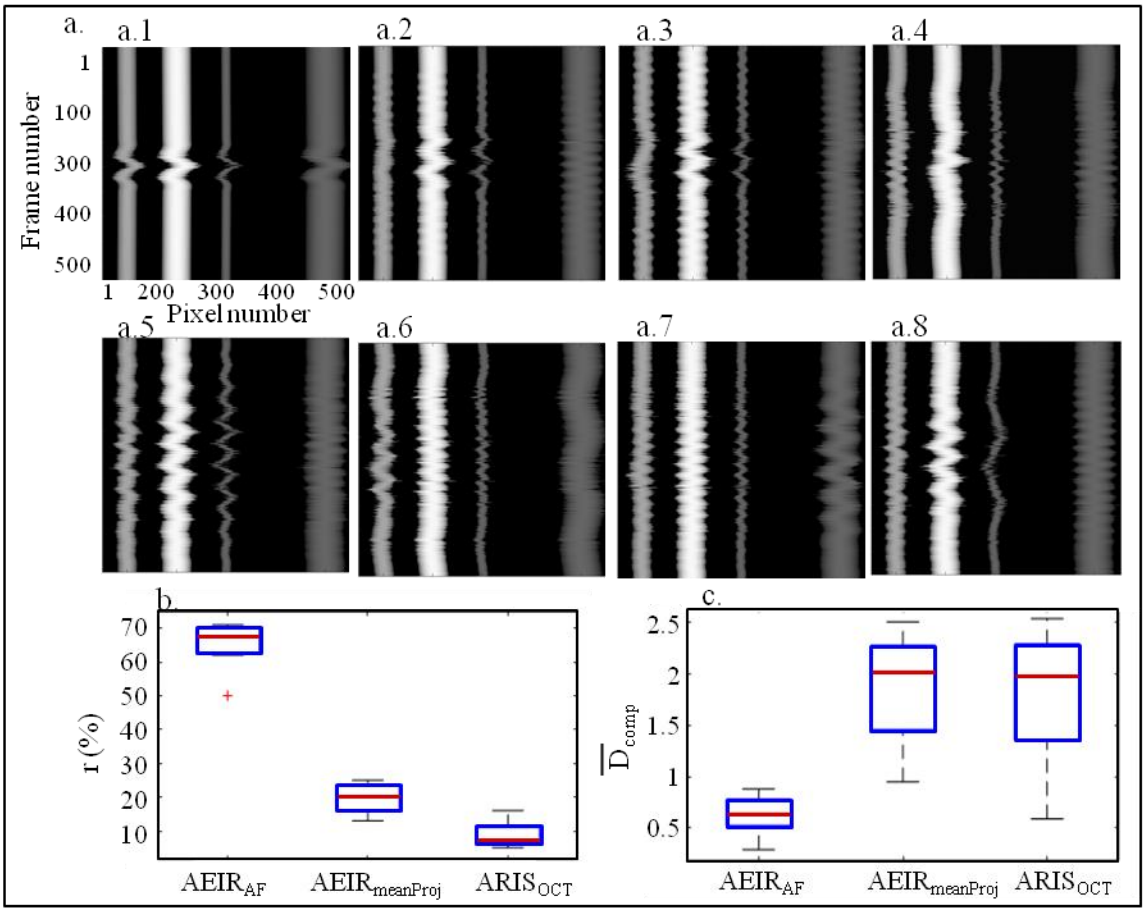

Figure 3-1: Simulated artifacts results. (a) eight simulated artificial artifact results on a digital phantom. (b) and (c) are r and $\overline{D}_{comp}$ metrics, respectively, for these eight artifacts on the *in vivo* image.

A more detailed examination of artifacts a.1 and a.2 from Figure 3-1 and the quantitative analysis of motion artifacts to correct them are further presented. Figure 3-2 to 3-6 show results of the artificial artifacts 1 and 2, their correction, and the comparison between the artifacts and the corresponding three correction methods. The results of the application of the artifacts a.1 and a.2 and their corrections on a NURD phantom image are shown in Figure 3-2 and Figure 3-4, respectively, and on an *in vivo* image in Figure 3-3 and Figure 3-5, respectively. Figure 3-6 shows artifacts a.1 and a.2 on the corresponding *in vivo* AF images.

In Figure 3-2 to 3-5, the original image is shown in (a). The artificial artifact was applied to this image and the result shown in (b). The corrected images using $AEIR_{AF}$, $AEIR_{meanProj}$, and $ARIS_{OCT}$ methods are shown in (c-e). The artifacts and three correction matrices, where each pixel represents the corresponding pixel shift in each matrix, are shown in (g-j). For an excellent correction method, the correction matrix should be the same as the artifact matrix; in other words, the correlation of these two matrices should be 100%. $\overline{D}_{comp}$ is shown in image sections (l-o), where l has a correction matrix identical to the artifact matrix. The average compensated difference is calculated based on matrices in sections (l-o). The average pixel shift for each frame (row) of the artifact and correction matrices is shown in section (f). The difference between the average pixel shifts of the artifact matrix and the correction matrices are shown in (k).

The two correction evaluation parameters for the NURD phantom and *in vivo* images are shown in Table 3-2 and Table 3-3, respectively. The performances of the correction methods were evaluated considering both parameters. The r-value is larger for OCT-$AEIR_{AF}$ and OCT-$AEIR_{meanProj}$ compared to $ARIS_{OCT}$ indicating more similarity between the correction and artifact matrices. $\overline{\boldsymbol{D}}_{\boldsymbol{comp}}$ is closer to zero for OCT-$AEIR_{AF}$ in all cases. Although $\overline{\boldsymbol{D}}_{\boldsymbol{comp}}$ is smaller for

OCT-AEIR$_{meanProj}$ than ARIS$_{OCT}$ in phantom images, it is bigger in the *in vivo* ones. One reason might be due to some uncorrected imaging artifact still present in the corrected ground truth image even after multiple iterations of the correction process. As an example, there are two leaps in average pixel shift at frames 322-323 and 343-344 that cause OCT-AEIR$_{meanProj}$ to perform less optimally than OCT-AEIRAF (Figure 3-4f). This might arise from the corrected ground truth image which is distorted dependent on the alignment algorithm (the AF data). It would be reasonable to assume that the same algorithm, based on the same data, is more likely to return to its previous stable state. The other two methods would likely have different stable states, and a non-optimal error metric even if no motion artifact is applied; this could put them at a disadvantage.

Table 3-2: Two parameters were calculated for quantitative and reproducibility analysis of the correction methods for artifacts 1 and 2 on the NURD phantom image shown in Figure 3-2 and Figure 3-4.

Parameter	Correction Matrix Based On							
	Artifact		OCT-AEIR$_{AF}$		OCT-AEIR$_{meanProj}$		OCT-ARIS$_{OCT}$	
	#1	#2	#1	#2	#1	#2	#1	#2
r (%)	100	100	74	71	81	55	62	46
$\overline{D}_{comp}$	0	0	0.19	0.35	0.63	1.17	0.5	1.09

Table 3-3: Two parameters were calculated for quantitative and reproducibility analysis of the correction methods for artifacts 1 and 2 on the *in vivo* image shown in Figure 3-3 and Figure 3-5.

Parameter	Correction Matrix Based On							
	Artifact		$OCT\text{-}AEIR_{AF}$		$OCT\text{-}AEIR_{meanProj}$		$OCT\text{-}ARIS_{OCT}$	
	#1	#2	#1	#2	#1	#2	#1	#2
r (%)	100	100	63	62	22	18	14	5
$\overline{D}_{comp}$	0.00	0.00	0.29	0.49	0.95	1.37	0.59	1.20

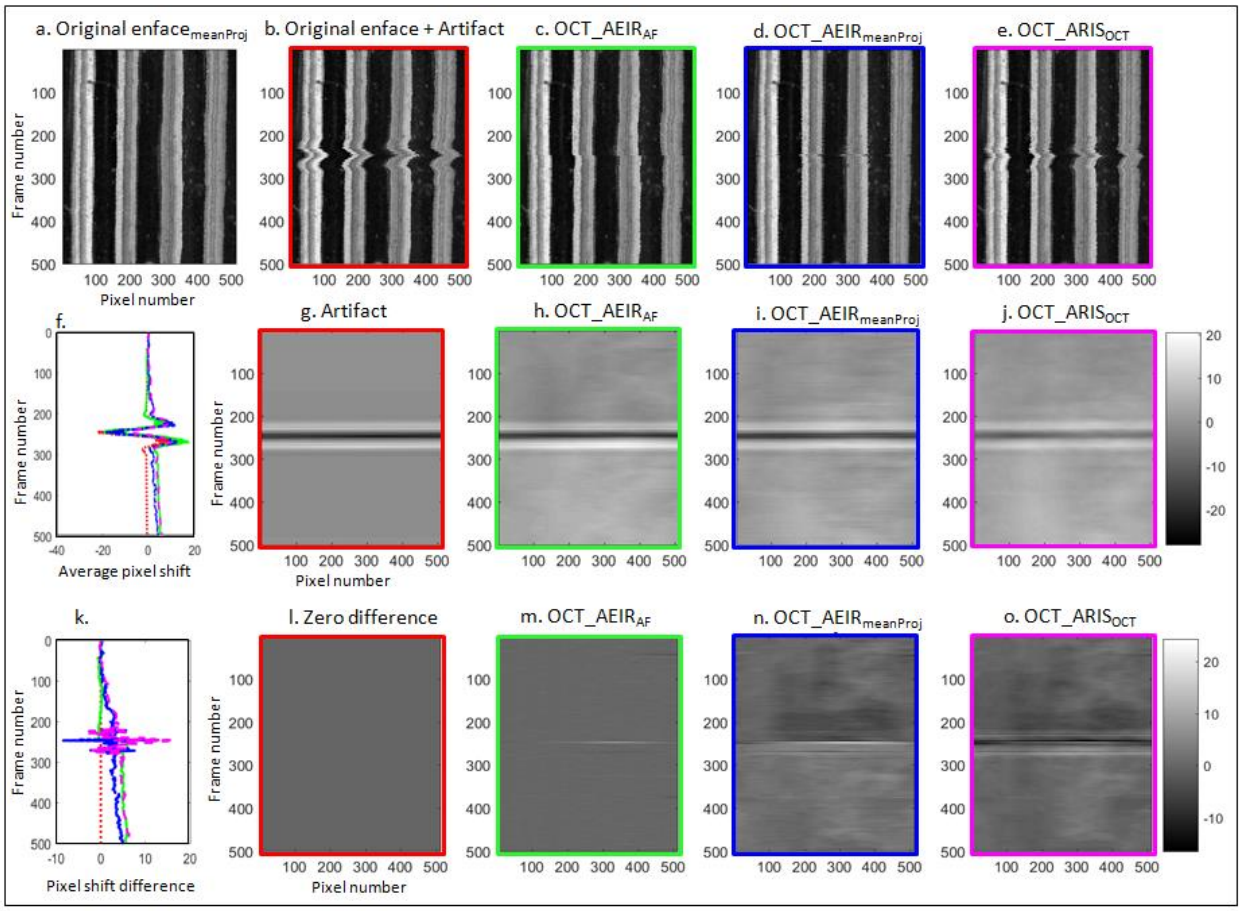

Figure 3-2: An analysis of the correction methods on a NURD phantom with artifact #1. (a) original image, (b) original image with artifact. (c), (d), (e) corrected images using the different methods. (f) average pixel shift plot. (g), (h), (i), (j) artifact and the three correction matrices, respectively. (k) difference of average pixel shift between correction methods and artifact. (l), (m), (n), (o) zero-difference's reference and difference between the correction matrices and artifact, respectively. Each color box is the same color as the curve in (f) and (k).

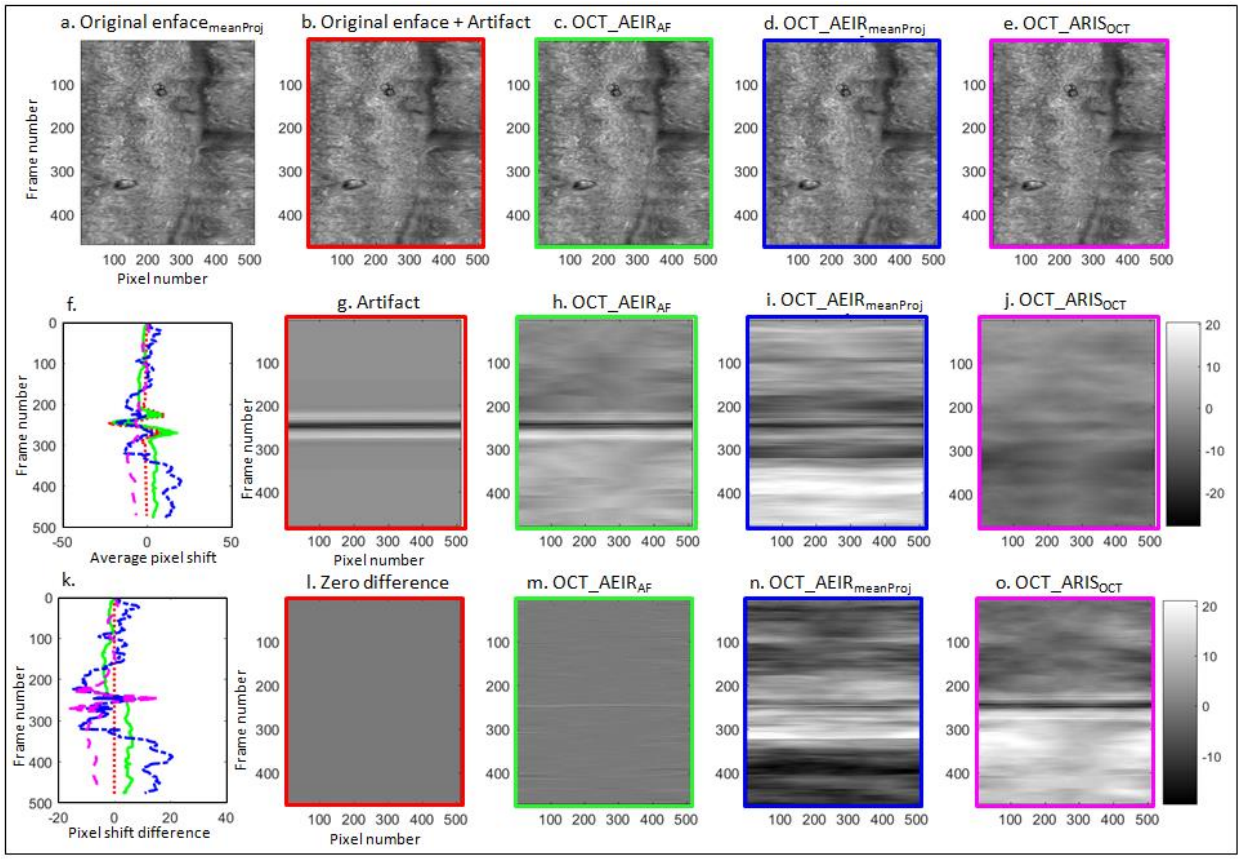

Figure 3-3: Results of analysis of correction methods on an *in vivo* image with artifact #1. (a) original image, (b) original image with artificial artifact. (c), (d), (e) corrected images with different methods. (f) average pixel shift plot. (g), (h), (i), (j) artifact and three correction matrices, respectively. (k) difference of average pixel shift between correction methods and artifact. (l), (m), (n), (o) zero-difference's reference and difference between the correction matrices and artifact, respectively. Each color box is the same color as the curve in (f) and (k).

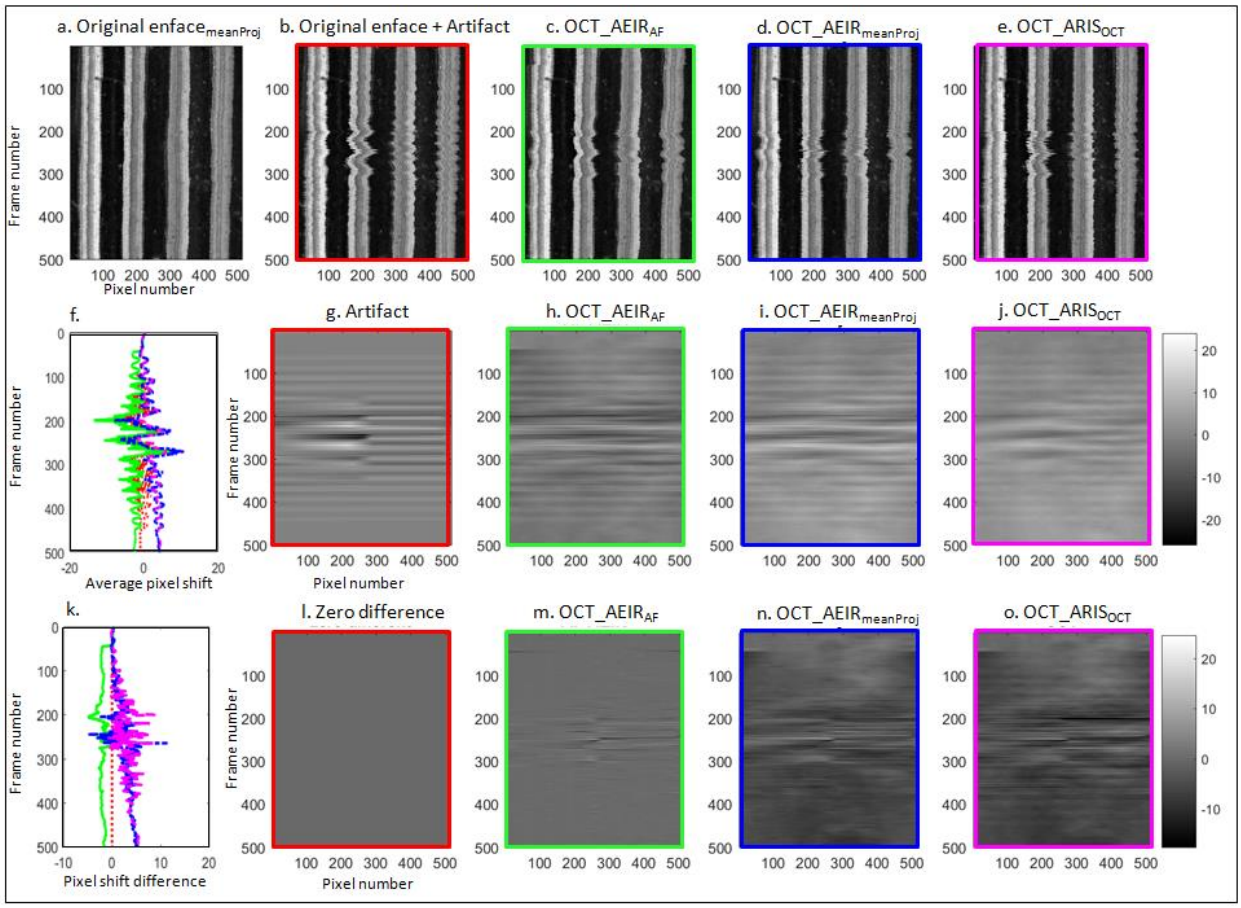

Figure 3-4: Analysis of the correction methods on a phantom image with artifact #2. (a) original image, (b) original image with artificial artifact. (c), (d), (e) corrected images with different methods. (f) average pixel shift plot. (g), (h), (i), (j) artifact and three correction matrices, respectively. (k) difference of average pixel shift between correction methods and artifact. (l), (m), (n), (o) zero-difference's reference and difference between the correction matrices and artifact, respectively. Each color box is the same color as the curve in (f) and (k).

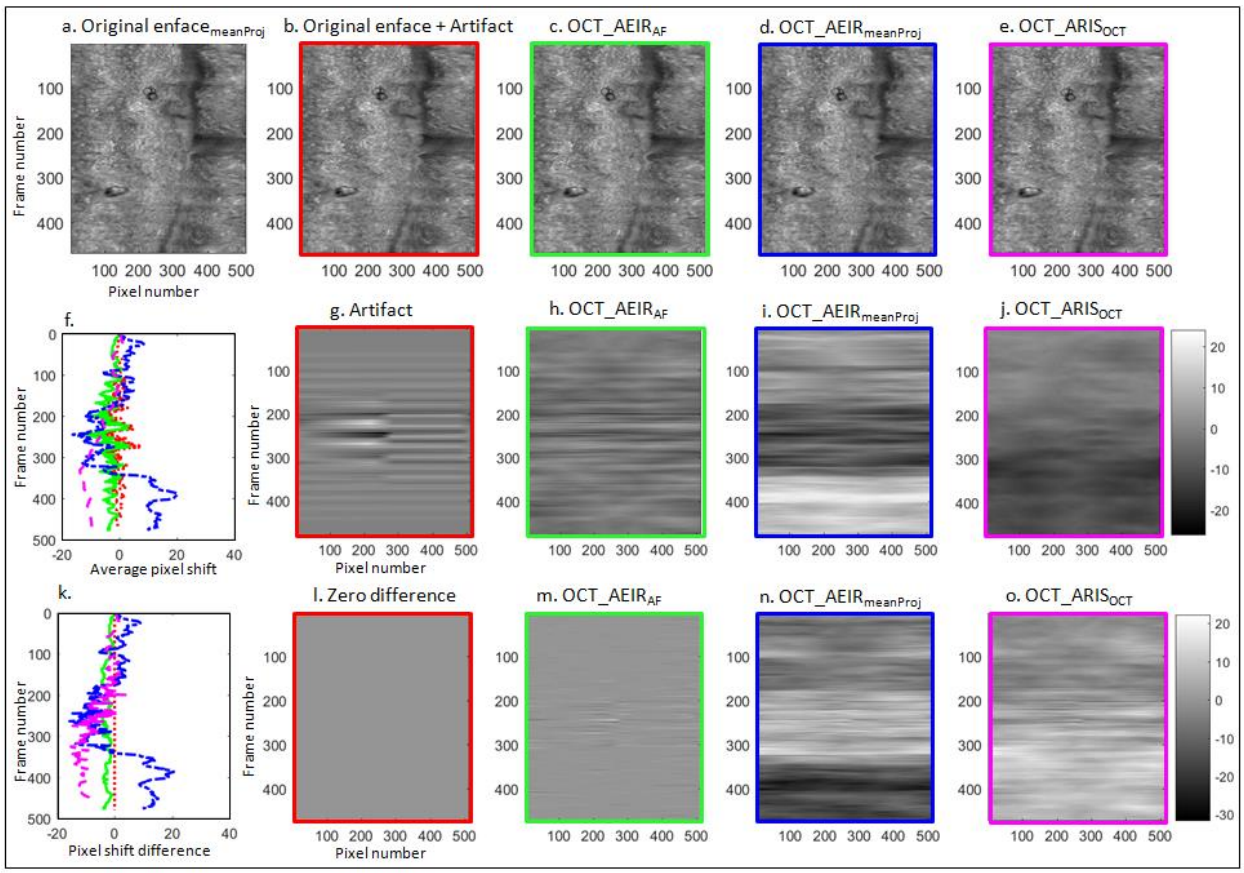

Figure 3-5: Analysis of correction methods on an *in vivo* image with artifact #2. (a) original image, (b) original image with artificial artifact. (c), (d), (e) corrected images with different methods. (f) average pixel shift plot. (g), (h), (i), (j) artifact and three correction matrices, respectively. (k) difference of average pixel shift between correction methods and artifact. (l), (m), (n), (o) zero-difference's reference and difference between the correction matrices and artifact, respectively. Each color box is the same color as the curve in (f) and (k).

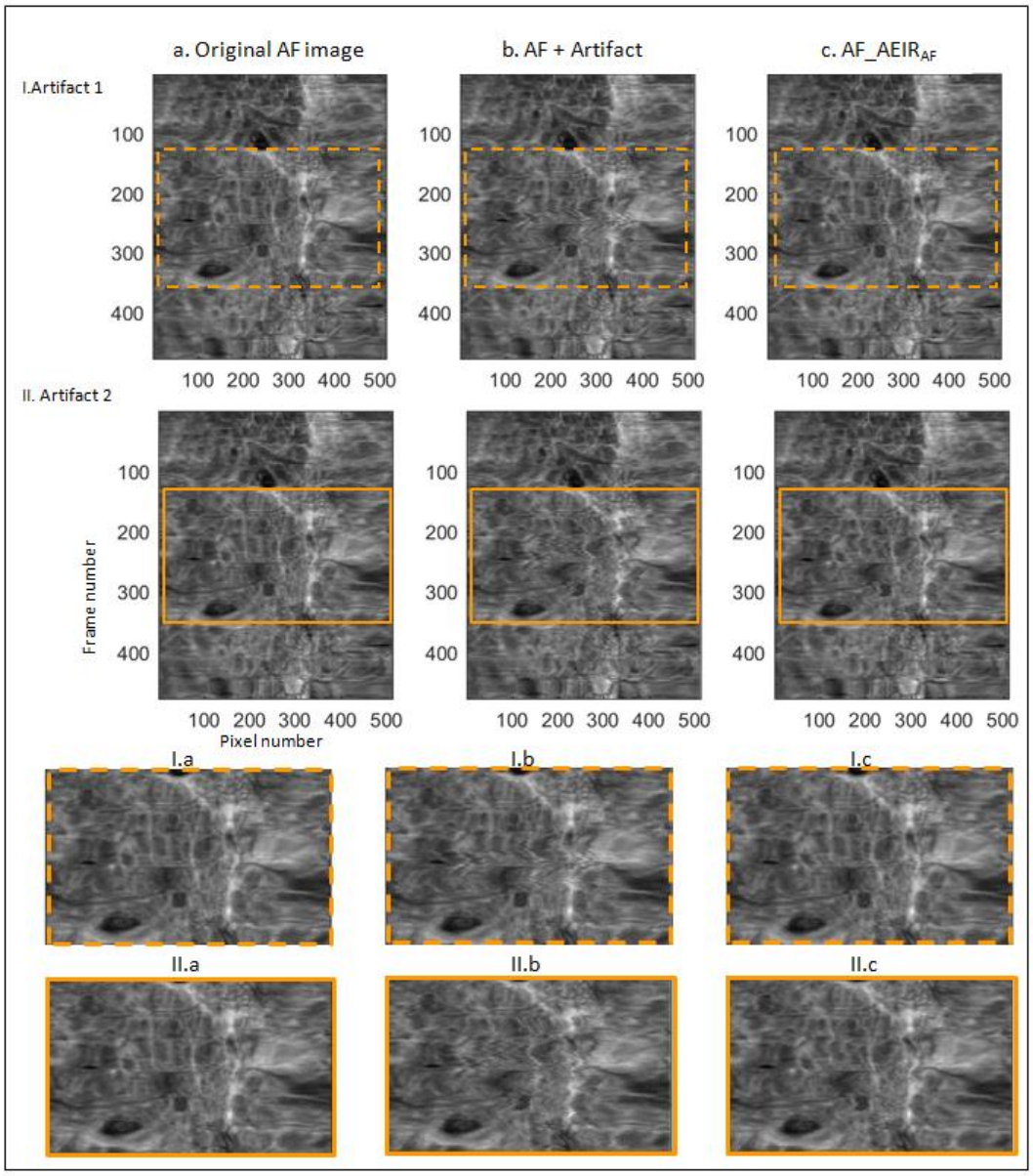

Figure 3-6: AF image with two different artifacts and corrected with the AF-AEIRAF method. (I) Artifact 1 and its correction. The dashed-orange box is the same area in the ground truth image, ground truth image with artifact, and in the corrected image. (II) Artifact 2 and its correction, where the solid-orange box is the same area in the ground truth image, ground truth image with artifact, and its corrected image. I.a-c and II.a-c are showing the enlarged dashed and solid box in (I) and (II).

I also quantitatively evaluated the choice of the optimized correction parameters (w,n,s,m). The same set of correction parameters were evaluated while applying simulated motion artifacts on both the NURD phantom image and the *in vivo* image. The quantitative results for four sets of parameters on a NURD phantom is in Figure 3-7. As shown, the quantitative metrics also confirm the visualized optimization set of w=20, n=20, s=5, and m=1 to have equal or better performance than the other sets while having the lowest computational cost. Although r and $\overline{D}_{comp}$ values are comparable for the four sets, they are more similar for 20-20-5-1 and 100-60-5-1.

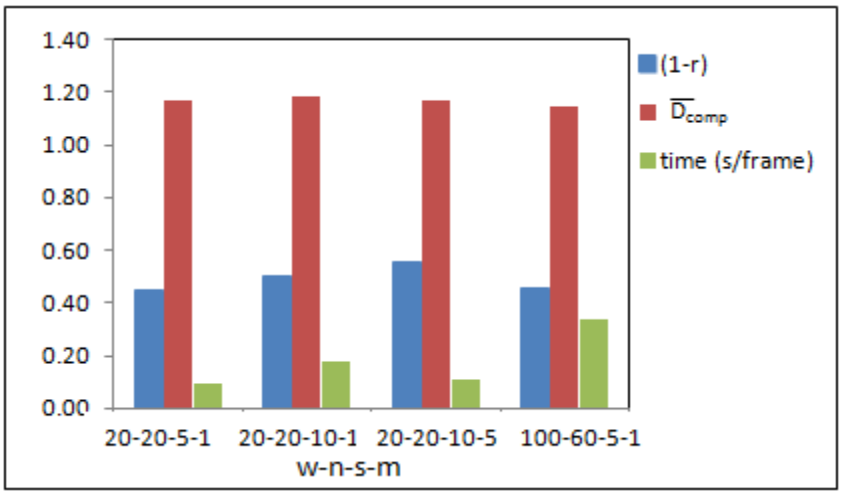

Figure 3-7: Quantitative evaluation for optimization of correction parameters. The reproducibility of each method was analyzed by comparing results of the correction methods for different artificial artifacts. The reproducibility of the correction methods depends on the artifacts needing to be corrected.

Based on quantitative analysis using the two metrics, I conclude that overall, OCT-AEIR$_{AF}$ and OCT-AEIR$_{meanProj}$ appear to correct a larger fraction of the visible artifacts than does ARIS$_{OCT}$.

3.4 Conclusion

In summary, I have presented a quantitative study based on the ground truth image and artificial motion artifacts and its correction using the AEIR method. Motion artifacts in *in vivo* imaging make identification of features and structures like blood vessels challenging. Correction of distortions of tissue features resulting from motion artifacts may enhance image quality and interpretation of images. In this chapter, I have described a simulation of motion artifacts for 3D or 2D rotational catheter data and two quantitative metrics (r and $\overline{D}_{comp}$) for evaluation of the motion correction methods. Our simulated artifacts may be applied on a ground truth image to create an image with known artifacts for the quantitative evaluation of performance of the correction methods. Since there might be some non-visible motion artifacts in the original ground truth image, I needed to apply the correction method before applying the simulated artifacts. However, there is no guarantee that this process converges to a motion-free scan. Also, the pre-corrected ground truth image is subjected to the correction method for further quantitative analysis. In conclusion, I have presented the quantitative evaluation of a ground truth image of an *in silico* phantom, a NURD phantom and *in vivo* OCT and AF images.

Chapter 4: *Ex vivo* micro-OCT Imaging of Cervical Lesions

4.1 Introduction

Cervical cancer is the fourth most frequently diagnosed cancer and the fourth leading cause of cancer death in women, with an estimated 604,000 new cases and 342,000 deaths worldwide in 2020. Cervical cancer is especially concerning in low-income and middle-income countries (LMIC). Incidence rates are 7-10 times higher in LMIC, with mortality rates reaching up to 18 times those of high-income countries (HIC). Cervical cancer can be curable in the early stages and more challenging to treat in the later stages. [2]

There has been a paradigm shift in cervical screening and detection due to increasing understanding of the human papillomavirus (HPV) as a causal agent. The vast majority of cervical HPV infections resolve on their own, but persistent infections with carcinogenic HPV types cause virtually all cases of cervical cancer. Persistent infections cause cervical intraepithelial neoplasia (CIN), which in turn, develops into invasive cancer if left untreated. [57][53][6][5]

Cervical cancer is considered preventable. Primary prevention with HPV vaccines is underway in HICs, though it will take years for the impact of these vaccines to be realized. As such, the secondary preventative measure of regular HPV screening is being conducted in HICs. [1][2] However, vaccines and screening programs have not been equitably implemented across the world. Less than 30% of LMICs have an implemented national HPV vaccination program. Only 44% of women in LMICs have ever been screened for cervical cancer. [1]

Cytology testing with Papanicolaou (Pap) smears in combination with the high-risk HPV test constitutes the basic cervical cancer screening system. Pap tests have a sensitivity of 40.3% and a specificity of 97.9%. [58] HPV testing has a sensitivity of 95.2% and a specificity of 62.5% for the detection of CIN2 and CIN3, both of which are considered high-grade lesions. [59] Other testing methods such as visual inspection with acetic acid (VIA) and colposcopy have also been recommended.[60] While VIA can offer real-time assessment, it is more subjective and has a lower sensitivity of 62% and specificity of 59%, for detecting CIN2 and CIN3 [61]. Hence, colposcopy-directed biopsy with histopathological confirmation is followed for diagnosis of cervical diseases. Although this approach is time-consuming, invasive and costly, it is highly successful with a sensitivity of 86.7% and a specificity of 90.4% [62]. Due to the invasive nature of biopsies, only a few biopsies may be taken for investigation which this increases the chance of missing lesions and diagnoses. Histopathological interpretation of loop electrosurgical excisional procedure (LEEP) is a gold standard for cervical dysplasia diagnosis.

There is a need for an inexpensive, efficient, and easy-to-use approach for cervical cancer management that can be implemented in LMICs to diagnose and treat patients in as few visits as possible. Several non-invasive technologies are currently under investigation for use in cervical cancer screening procedures. Cervical dysplasia and cancer often result in changes in the structure of cervical epithelium and nuclear morphology. Many novel non-invasive techniques focus on measuring nuclear size and eccentricity. Confocal microscopy can produce high-resolution images with molecularly-specific information. [63] Preliminary studies show that the nuclear/cytoplasmic ratio calculated from confocal images can be used to classify cervical cancer and dysplasia with a sensitivity of 92% and specificity of 48% [64] Autofluorescence microscopy has also been used to detect cervical precancer and cancer by

measuring chemical changes in tissue and epithelial fluorescence intensity [65]. Multispectral Digital Colposcopy (MDC) has also been used to measure multispectral autofluorescence and reflectance images of the cervix using fluorescence and reflectance wide field imaging. [66] All of these techniques are either limited by penetration imaging depths or low-resolution power to resolve the cellular structure of the cervical epithelium.

Optical coherence tomography (OCT) is another imaging modality that has been widely investigated in different biomedical fields, such as dermatology, endoscopy, dentistry, and oncology [67]. OCT was also investigated *ex vivo* and *in vivo* cervix and has shown its potential to detect and differentiate grades of precursor and cancerous lesions [68], [69]. However, OCT images obtained in these studies have low resolution (10-20 μm) and cannot visualize microarchitectural and cellular features. Micro-OCT is similar to conventional OCT which captures images of three-dimensional (x, y, z) cellular and sub-cellular biological structures with isotropic ~1μm spatial resolution and 10 ms temporal resolution. Micro-OCT is SD-OCT that relies on broad bandwidth supercontinuum sources as well as new software and optics. [32] Studies have shown that micro-OCT is capable of resolving individual subcellular features and their function, including beating respiratory cilia, inflammatory cell organelles, and individual bacteria – all without requiring exogenous contrast. [32],[70] The unprecedented microscopic imaging capabilities of micro-OCT make it a valuable tool for examining small pre-cancerous lesions.

In this chapter, I study normal and abnormal *ex vivo* human cervical tissue specimens using a benchtop micro-OCT device.

4.2 Methods

4.2.1 Imaging System Description

The schematic of the benchtop micro-OCT system used in this study is shown in Figure 4-1. [32] Briefly, light from a broadband supercontinuum light source is transmitted through a beam splitter (BS), and then coupled into a single mode fiber (SMF) using a collimator. Light from the SMF is then passed through another collimator. The central portion of the collimated light is reflected using a 45-degree angled rod mirror beam splitter and used as reference light. The reference light is focused using a lens onto the reference mirror, which is placed on a translational stage. The light transmitted around the rod mirror beam splitter is focused onto the sample using a lens. The focused sample arm light is scanned over the sample using a galvanometer-based scanner. The reflected reference and sample light are combined back at the rod mirror beam splitter and coupled back into the SMF. A 50/50 BS reflects part of the light from the single mode fiber towards a spectrometer which consists of a 900 lines-per-mm dispersion grating, 80 mm focal length lens, and a 4096-pixel line scan camera. The spectrometer records the wavelength-dependent interference signal, which is then transferred to a computer using a camera link cable, to a frame grabber, and then processed using custom-designed software.

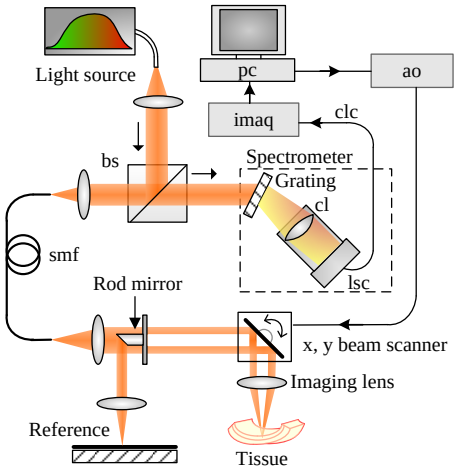

Figure 4-1: Micro-OCT instrumentation. ao: analog output board; bs: beam splitter; imaq: image acquisition board; cl: camera lens; lsc: line scan camera; smf: single mode fiber; pc: personal computer; clc: Camera Link cables. [32]

The light source employs a broad bandwidth light source 800±150 nm to achieve 1 µm axial resolution. A relatively high NA=0.12 lens in the sample arm provides high lateral resolution of the system to be ~2 µm. An annularly apodized light using rod mirror instead of regular beam splitter provides extended depth of focus to be approximately 200 µm.

4.2.2 Study Protocol and Imaging Procedures

The study was approved by the Institutional Review Boards of the Massachusetts General Hospital (MGH), Kings County Hospital (KCH), Brookdale Hospital Medical Center (BHMC), University of British Columbia and BC Cancer Research Center. All patients referred for colposcopy, LEEP treatment, cryosurgery, or laser surgery for any cause were eligible for this study. Non-pregnant women aged 18 years and older who have normal and abnormal Pap smears were invited to participate in this study; patients who previously had surgery to remove their cervix were excluded. 58 patients, between 23-68 years old, with abnormal Pap or HPV test results were recruited (12 at

the KCH and 46 at the BHMC). Informed consent was obtained from all participants and/or their legal guardians. Fresh cervical specimens were collected via colposcopic biopsy. Before imaging, cervical specimens were placed in phosphate buffered saline (PBS) on ice to keep the tissue fresh while transferring them to MGH for micro-OCT imaging. Micro-OCT imaging was typically performed within 24 hrs of excision. 2D and 3D micro-OCT images were acquired for each specimen, then acetic acid was applied and imaging was repeated. Gross photographs were taken of all the samples before micro-OCT imaging. Subsequently, samples were placed in formalin to be fixed and prepared for sectioning and H&E staining. Figure 4-2 shows the steps from a biopsied sample (A), then obtaining 2D and 3D micro-OCT images (B) and (C) respectively, and finally the H&E histology slide (D).

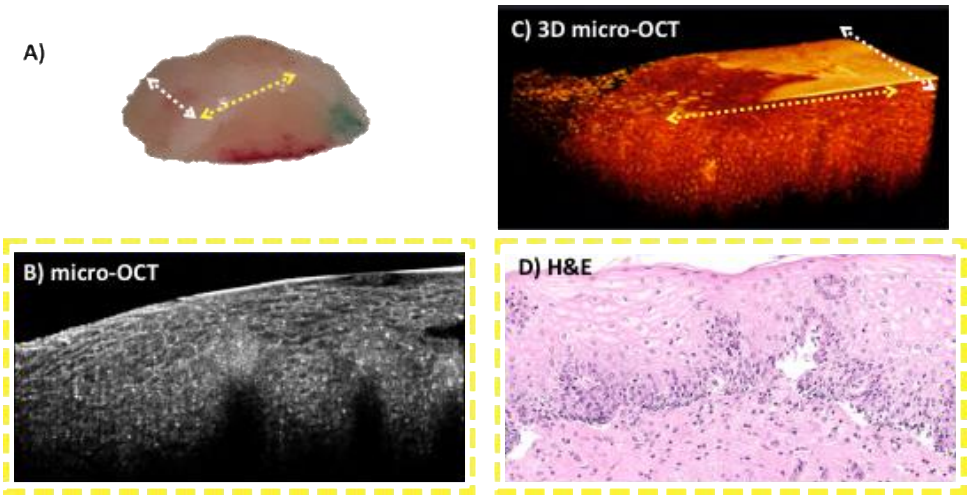

Figure 4-2: Micro-OCT imaging for cervical cancer diagnosis. A) Cervical biopsy gross photograph with micro-OCT imaging directions, B) 2D micro-OCT image, C) Representative 3D micro-OCT image, D) Cervical tissue H&E slide.

4.2.3 Image Processing and Analysis

Micro-OCT images were processed in MATLAB and visualized in ImageJ (http://rsbweb.nih.gov/ij/download.html, Bethesda, MD). Micro-OCT images were compared and matched regarding histological slides of the corresponding samples which were scanned with a Nanozoomer scanner (Hamamatsu Inc.) and visualized in NDP.view2 viewer software (Hamamatsu Inc.). Micro-OCT images were rescaled in ImageJ to be at 1:1 aspect ratio in the axial and transverse direction to be comparable to corresponding histological slides. Optical features differentiating cervical dysplasia and useful for cervical disease diagnosis were distinguished and summarized to be used for grading cervical micro-OCT images.

4.2.4 Image Classification and Statistical Analysis

A training dataset of 12 2D cross-sectional micro-OCT images were thoroughly reviewed to determine useful diagnostic criteria for image interpretation. Using these micro-OCT diagnostic criteria, the pathologist was asked to provide a diagnosis for 46 2D cross sectional micro-OCT images. The pathologist was provided with the blinded corresponding H&E histological slides in digital form to make a diagnosis for each cervical tissue sample. He was blinded to the patient information and the screening test status information and results.

Diagnostic sensitivity, specificity and accuracy were calculated using histological diagnosis of each micro-OCT image as the ground truth. The 95% confidence interval (CI) for each statistical parameter was calculated.

$$Sensitivity = \frac{TP}{TP+FN} \quad (4.1)$$

$$Specificity = \frac{TN}{TN+FP} \quad (4.2)$$

$$Accuracy = \frac{TP+TN}{TP+FN+TN+FP} \quad (4.3)$$

4.3 Results

4.3.1 Micro-OCT diagnostic features

Figure 4-3 shows micro-OCT images and corresponding H&E histologic sections of human cervical *ex vivo* tissue, which includes normal cervix, low-grade squamous intraepithelial lesions (LSIL) and high-grade squamous intraepithelial lesions (HSIL). LSIL includes CIN1 and HSIL includes CIN2 and CIN3. In normal tissue (Figure 4-3(A-B)), stratified squamous cells form a mesh-like pattern. Stratified squamous epithelium and stroma exhibit well-organized layered architecture in the micro-OCT image. The interface between epithelium and stroma may be clearly observed.

Figure 4-3C shows LSIL. Although densely packed cells cause the lower epithelium to exhibit hypo-scattering characteristics, the superficial epithelium maintains its mesh-like structure. Koilocytic cells are visible as enlarged nuclei and perinuclear halos which are representative features of low-risk HPV infections. In a typical micro-OCT image of LSIL, unstructured hypo-scattering regions in the lower third of the epithelium can be identified. The interface between the epithelium and the stroma may be less clear than in normal tissue.

Figure 4-3D shows a micro-OCT image and corresponding H&E histologic section of HSIL. Micro-OCT shows unstructured hypo-scattering features, matching well with hyperplasia observed throughout the whole epithelium in H&E sections. I observed that the epithelium and stroma are hyper-scattering, and epithelial brightness typically increases with the degree of dysplasia, but decays more quickly with depth than for normal tissue. For HSIL, epithelial architecture is lost for more than one-third of the epithelium, but the interface between squamous epithelium and stroma is still clearly delineated by the basal membrane in the micro-OCT image. Characteristic micro-OCT optical features for each group are summarized in Table 4-1. These findings were consistent with previous reports [71], [72].

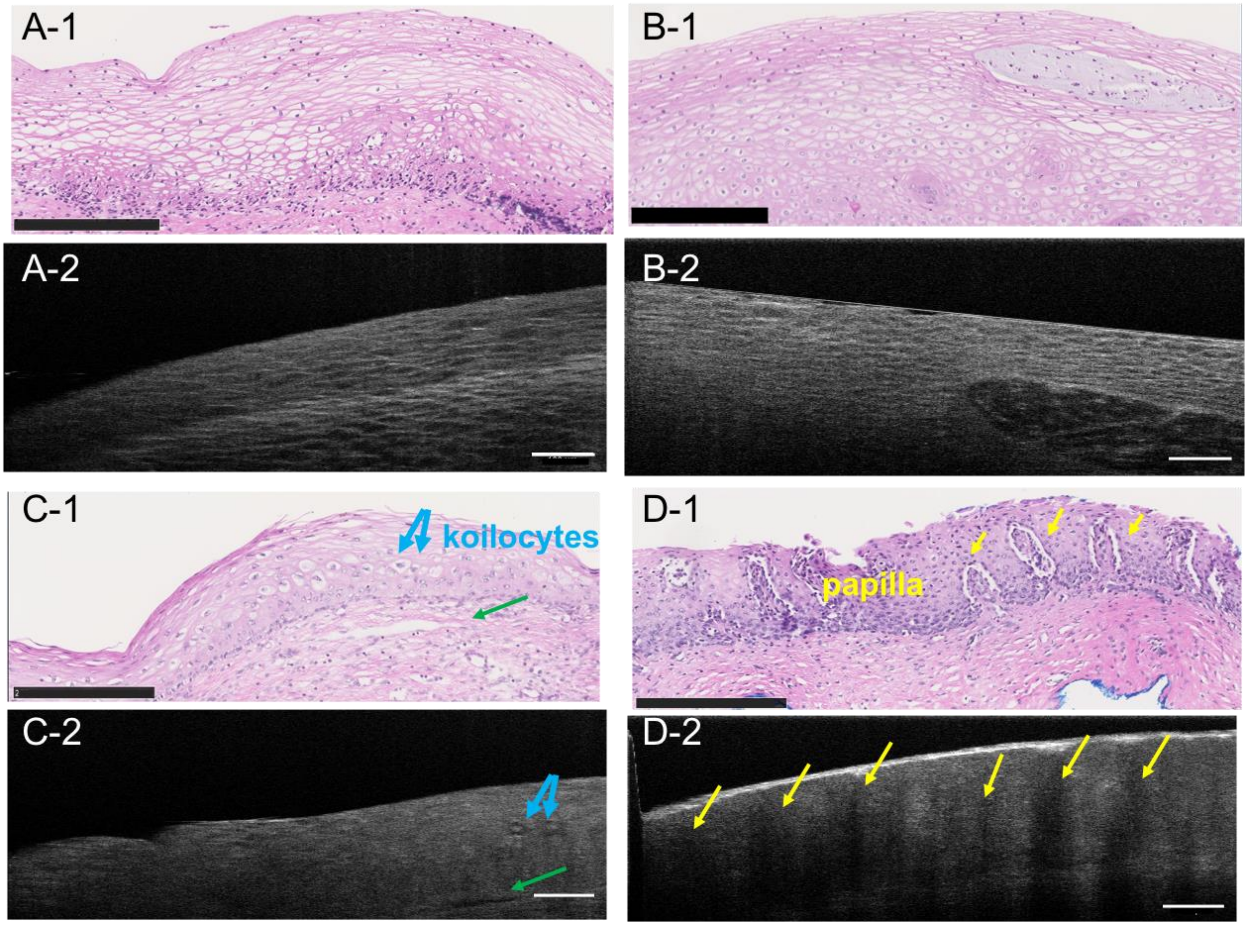

Figure 4-3: Typical micro-OCT images (-2) and corresponding H&E histologic sections (-1). (A-B) normal tissue, (C) LSIL and (D) HSIL. White scale bar in micro-OCT images is 100 µm. Black scale bar in H&E images is 250 µm.

Table 4-1: Optical features of different cervical lesions in micro-OCT imaging of human cervical tissues.

Category	Micro-OCT features
Normal	- Stratified mesh-like architecture. - Two-layered architecture representing the epithelium and stroma.
LSIL	- Characteristic koilocytes (enlarged nuclei with perinuclear halos). - Loss of regular architecture at the lower third of the epithelium. - Hypo-scattering features.
HSIL	- Loss of regular architecture over more than one third of the epithelium. - The boundary between the epithelium may be clear or less clear. - Present papillary structures with hypo-scattering boundaries.

Figure 4-4 shows micro-OCT images of cervical samples before and after adding acetic acid. Application of acetic acid on cervical samples has been observed to increase contrast of micro-OCT images. Acetic acid makes the nuclei appear bright in the micro-OCT images as can be seen in Figure 4-4A-II. In HSIL tissues, the intensity of the OCT signal is increased. As seen in Figure 4-4B-II, there is no architecture over the epithelium and a uniform bright intensity indicating a high density of nuclei.

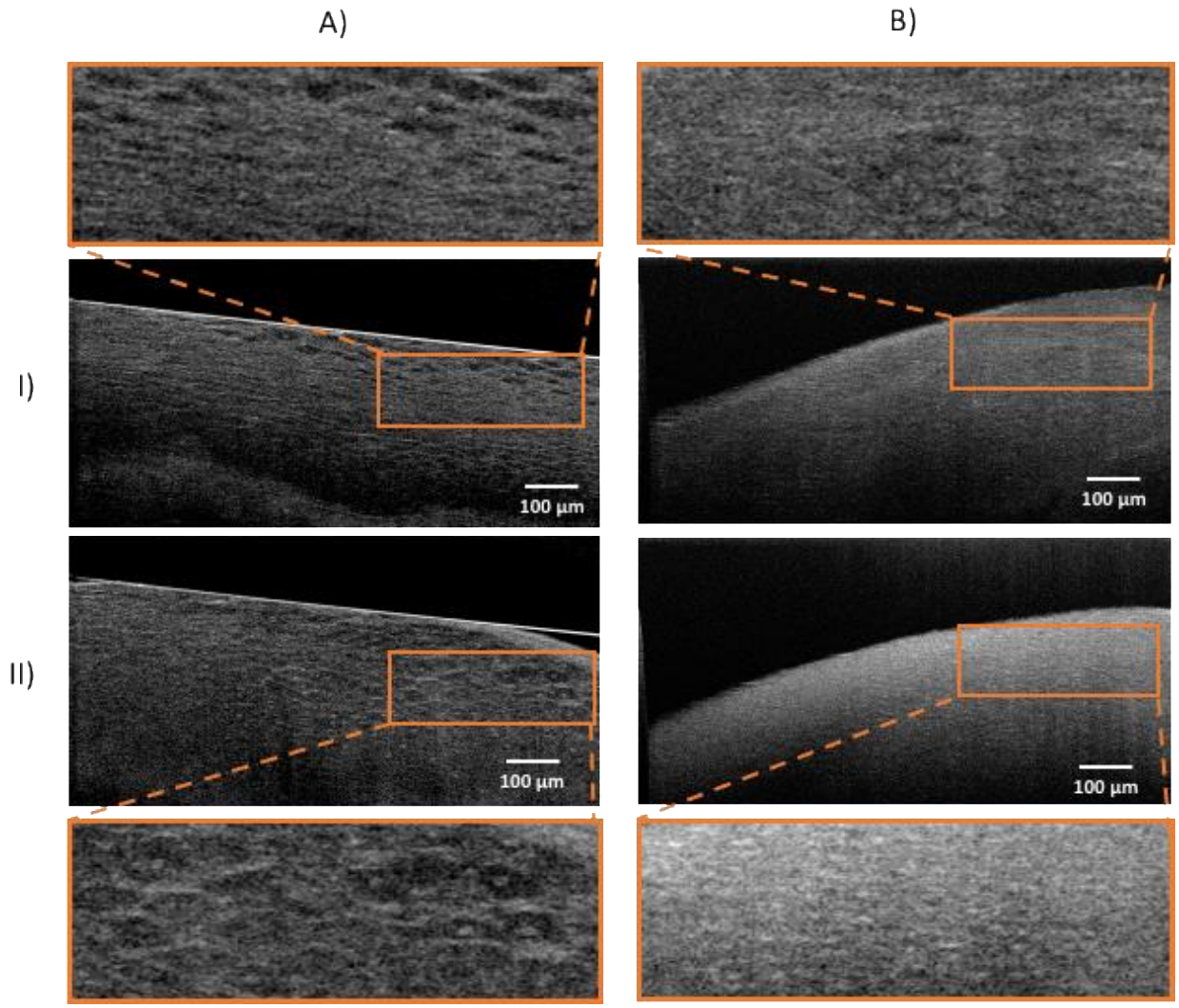

Figure 4-4: Acetic acid on micro-OCT imaging. A) normal tissue and B) HSIL tissue. Row I and II show before and after acetic acid applied on cervical samples, respectively. The orange rectangles show the zoomed in regions.

4.3.2 Image Classification and Statistical Analysis

Image classification was performed based on the protocol described in Methods. Micro-OCT obtained without acetic acid application were used to assess the diagnostic utility of this approach. The pathologist was asked to diagnose each 2D micro-OCT dataset based on the optical features

shown in Table 4-1. An overview of the blinded diagnoses made by the pathologist is shown in Table 4-2. Normal and LSIL specimens were classified as low-risk, while HSIL and invasive lesions were classified as high-risk. Table 4-3 summarizes the classification statistical results. Overall diagnostic accuracy for the investigator was 85%. A sensitivity of 100% and a specificity of 83% was achieved. A sensitivity of 100% may be attributed partially to the small dataset.

Table 4-2: Diagnosis of samples based on histology slides and a pathologist reading.

		Histology diagnosis	
		Normal/LSIL (low-risk)	**HSIL (high-risk)**
µOCT diagnostics	**Normal/LSIL (low-risk)**	33 (TN)	0 (FN)
	HSIL (high-risk)	7 (FP)	6 (TP)

Table 4-3: The classification statistics for classifying normal/LSIL vs HSIL on the test dataset.

Sensitivity	100% (95% CI, 54% - 100%)
Specificity	83% (95% CI, 67% - 93%)
Accuracy	85% (95% CI, 71% - 94%)

CI: Confidence Interval

4.4 Discussion and Conclusion

In this chapter, I have studied and evaluated a micro-OCT bench-top system [32] as a diagnostic tool for cervical dysplasia. Cervical micro-OCT images show detailed and characteristic cellular

features useful in distinguishing between low-risk and high-risk abnormal changes in human cervical tissue. Our findings were consistent with previous reports [71]. This is a significant improvement upon past studies using conventional OCT or confocal imaging systems.

Conventional OCT with low resolution (10-20 μm) uses features such as thickness of the epithelium, brightness and contrast between the epithelium and stroma, status of the basement membrane, and brightness intensity profile of the epithelium for diagnosis [73], [15], [17]. A sensitivity of 80%-86% and specificity of 60-64% was reported with a threshold at CIN 2 [15]. Even though these features are diagnostically useful, they are not entirely consistent with diagnostic features observed in gold standard H&E histological sections.

Confocal endomicroscopy reveals changes in nuclear to cytoplasmic area ratios. It can enhance visualization of nuclear morphology, a clinically relevant feature for the detection of cervical precancers. Vital dyes are topically applied to the cervix to provide high optical contrast. For example, proflavine, a fluorescent DNA label, is used for *in vivo* diagnostic evaluation of cervical epithelial cells which distinguishes nuclei from the cytoplasm of the cell. [74],[20] Quantitative high resolution confocal endomicroscopy achieved a sensitivity of 86% and specificity of 87% with a threshold at CIN 2. [20]. Long-term follow-up studies with larger sample sizes are required to assess the impact of topical use of proflavine on the cervical epithelium, though it is suggested that cervical proflavine exposure is not associated with acute disease progression. [75]

VIA is used with white light colposcopy to identify abnormal areas and guide cervical biopsy. [60] 5% acetic acid is applied and the cervix is visually examined for acetowhitening of the tissue, since dysplastic tissue appears white after application. [20] The application of acetic acid enhances the scattering coefficient of precancerous tissue to approximately three times that of normal

epithelium, thereby making abnormal tissue appear whiter as a result of altered nuclear morphology, optical density, and changes in chromatin texture. [9] Similarly, in this work I applied acetic acid to *ex vivo* cervical samples to evaluate its effect on micro-OCT. As expected, the nuclei become apparent and manifested as bright dots in the cervical micro-OCT images. The contrast of micro-OCT images was also increased. In HSIL tissues, the intensity increased as the density of nuclei is greater than is in normal and LSIL tissue. From this initial examination, it appears that micro-OCT assessment of cervical tissue may benefit from the application of acetic acid as a means to increase the image quality and increase the intensity in HSIL tissue. However, due to incomplete data collection, we were unable to conduct the same diagnostic assessment as described in 4.3.2. It would be worthwhile to examine diagnostic utility of micro-OCT in examining cervical tissue post-application of acetic acid in future studies.

The micro-OCT system, with an axial resolution of ~1 μm and lateral resolution of 2 μm, clearly revealed microstructures of squamous epithelium, basement membrane and invasive tumors, which matched well with their corresponding H&E histological slides. The ability to resolve cellular features with micro-OCT enabled us to make low-risk versus high-risk diagnosis of human cervical lesions with high accuracy (e.g., sensitivity of 100%, specificity of 83%, and an overall accuracy of 85%).

I showed that high-risk lesions can be identified, such as homogeneous hyper-scattering features and heterogeneous characteristics which are consistent with previous reports. [61],[68],[76] These unstructured features are likely caused by increased nuclear size, increased nuclear-to-cytoplasmic ratio, hyperchromasia, and binuclear or multinuclear cells. Hyper-scattering desmoplastic reaction,

a valuable feature for identifying high-risk tissue in H&E sections, as well as the koilocytotic cells, were observed in our micro-OCT images, which is consistent with a previous report [61].

One of the key advantages of micro-OCT is that it can provide real-time imaging without removing or processing tissue. Micro-OCT can be integrated into small diameter probes which enables micro-OCT to be used in the clinic for *in vivo* cervical imaging and screening. However, as a new developing technique, micro-OCT has some limitations in the clinic. It may be challenging for pathologists and gynecologists to learn to make diagnoses based on micro-OCT images as it is a new imaging technology.

In summary, I characterized diagnostic micro-OCT features of different types of human cervical lesions, ranging from normal cervix, LSIL, to HSIL. A sensitivity of 100% (95% CI, 54% - 100%), a specificity of 83% (95% CI, 67% - 93%) and accuracy of 85% (95% CI, 71%-94%) were achieved to differentiate low-risk and high-risk cervical lesions. In order to implement micro-OCT imaging for *in vivo* cervical imaging, it is necessary to design and develop a forward-viewing micro-OCT probe. This would allow for screening and imaging of the ectocervix in real time in clinic. With further development and improvement, micro-OCT has the potential to become a complementary tool for cervical cancer screening and management.

Chapter 5: Forward-Viewing Micro-OCT Probe for Cervical Screening and Imaging

5.1 Introduction

As discussed in the chapter 4, micro-OCT imaging is a potential and efficient imaging modality for cervical cancer screening. The micro-OCT bench top system could differentiate low-risk and high-risk cervical lesions with high sensitivity and accuracy. Therefore, micro-OCT is a promising complementary tool for cervical cancer screening suitable for clinical application. This chapter describes the design and process of developing a clinically suitable optical imaging probe.

In a colposcopy clinic, a speculum is used for cervical examination. It is inserted into the vaginal canal and opened to allow visualization the ectocervix as shown in Figure 5-1. [77] The Cusco vaginal speculum is usually about 80 mm in length and 22 mm in width. [78] The micro-OCT probe must fit within the speculum.

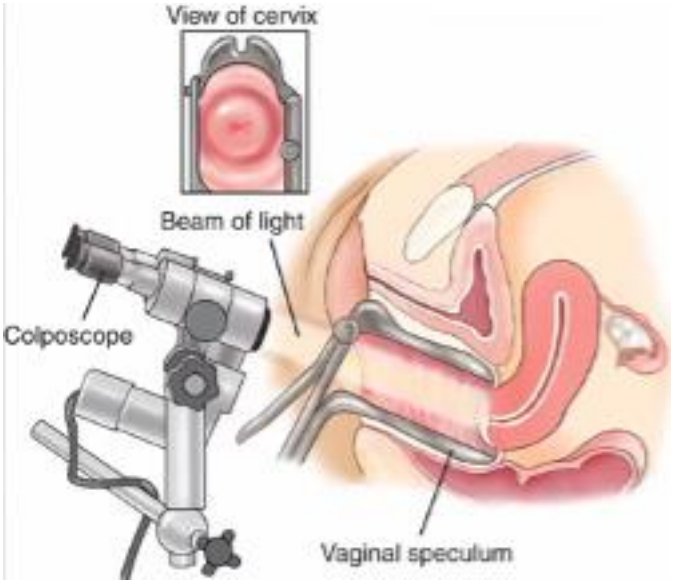

Figure 5-1: Colposcopy and use of speculum for cervical examination [77]

Endoscopic OCT using minimally invasive probes is an emerging imaging modality for gastrointestinal tract and coronary artery imaging [79],[80],[81],[41]. This approach is constrained by limited probe diameter (<1 mm) and the requirement of a flexible endoscopic probe. OCT probes may be designed for side- or forward-viewing. Side-viewing probes enable imaging of luminal organs, and rely on either rotating fibers that scan the OCT beam through proximal rotary and pullback actuation of a torque cable [82] or employ a distal rotary scanning micromotor. [83][84]. Forward-viewing OCT probes are used in non-luminal clinical applications and can examine small regions of interest (ROIs) at high resolution. This approach uses microelectromechanical systems (MEMS) [85][86] or piezoelectric actuators [43][87] to enable distal 2D scanning. MEMS are considerably larger in diameter or a rigid length. A piezoelectric tube excites a single-mode fiber to oscillate in a spiral configuration. Figure 5-2 shows the piezoelectric tube and spiral scan illumination for 2D scanning. A lens would be placed in front of the scanning fiber to focus the light into the tissue.

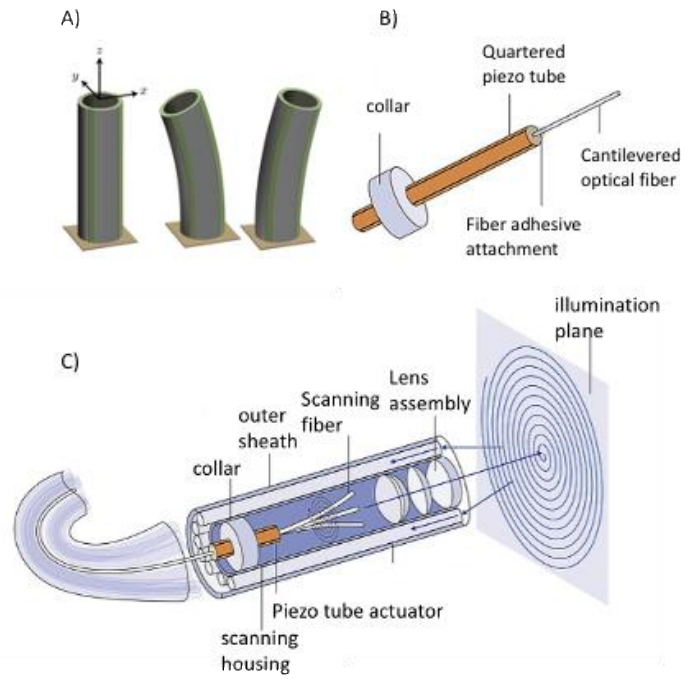

Figure 5-2: (A) Piezoelectric tube with a fixed base and free end. [88] **(B) The resonant SMF is centered to a miniaturized tubular piezo actuator.** [89] **(C) piezoelectric tube excites a single-mode fiber to oscillate in spiral configuration.** [89]

In micro-OCT, a high numerical aperture lens is used to focus the light onto the tissue in order to achieve high lateral resolution. However, due to the inherent trade-off between resolution and depth of field, micro-OCT is unable to provide cross-sectional images at this resolution through conventional OCT probe optics. An intravascular imaging system and a catheter based on few-mode interferometry enables 3D cellular-resolution intravascular imaging *in vivo* via a sub-millimeter diameter flexible catheter that can have a larger DOF. The few-mode interferometry imaging system for extending DOF imaging is shown in Figure 5-3. A segment of a multimode fiber is spliced with a single-mode fiber as a single-mode-multimode (SMM) fiber element, which generates few-modes which corresponds to the number of circular propagation modes supported by the multimode fiber. [90]

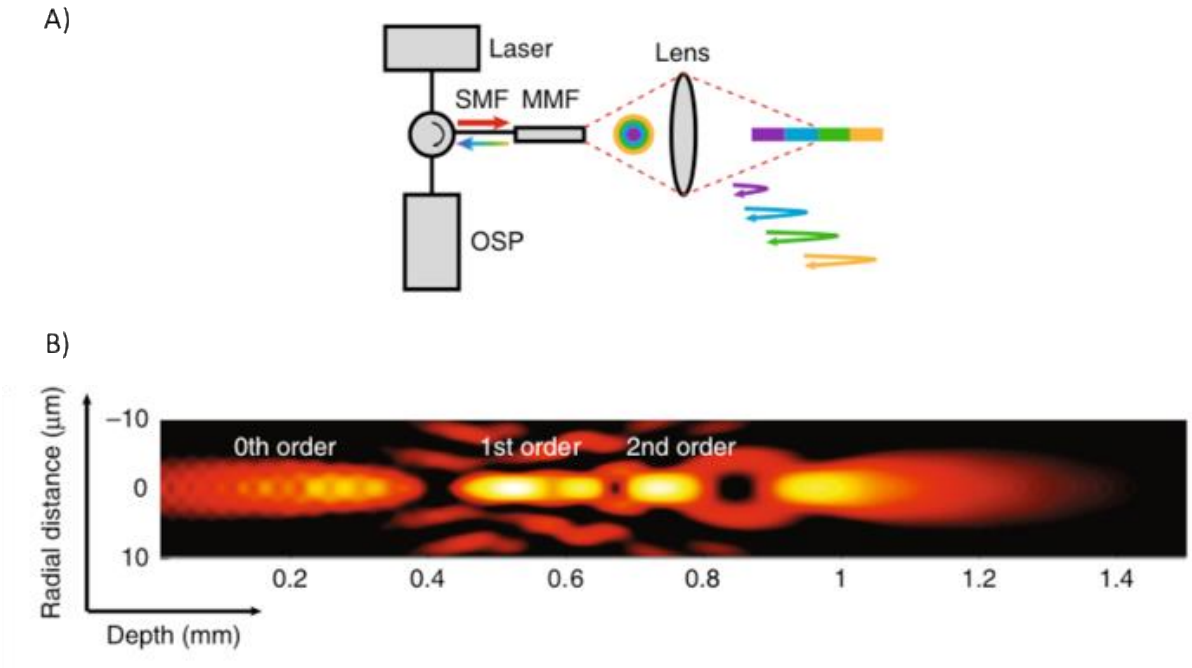

Figure 5-3: The concept few-mode generation processes of an SMM fiber system for extension of DOF. A) Colour pattern corresponds to different propagation modes. A system wavelength of 800 nm is assumed. B) Simulations of the focused field intensity distribution in the image space. SMF single-mode fibre, MMF multimode fibre, OSP optical signal processing unit. [90]

In this chapter, I integrate the piezo tube actuator and SMM fiber systems in a forward-looking high-resolution micro-OCT probe suitable for cervical and colposcopy applications. This probe design will subsequently be integrated into the micro-OCT bench top system used in chapter 4, a SSD-OCT system illuminated with a broadband supercontinuum light source.

5.2 Material and Method

5.2.1 Optical Probe Modeling

I model the proposed optical probe design in Zemax (OpticStudio) based on compact off-the-shelf components such as the C-Lens. I used the non-sequential mode in Zemax to model the SMM fiber element. Since the fiber would be scanned in a linear mode configuration, the beam would be on-axis and off-axis to the C-Lens optical axis. Therefore, I modeled the off-axis beam configuration and compared it to the on-axis configuration to characterize the beam spot size and lateral resolution over the field of view.

Scanning the fiber results in tilting the fiber by a small angle with reference to the C-Lens optical axis, which can affect the beam focusing characteristic. I modeled the off-axis fiber scanning in two configurations. In the first configuration, I have modeled the off-axis fiber considering small angle approximation as the scanning fiber actuation is very small. Moreover, a model simulating the off-axis beam entering the C-Lens would be suitable to characterize the off-axis resolution. In this configuration, the fiber can be modeled as moving perpendicular to the optical axis instead of tilting. From an optical modeling point of view, this situation is equivalent to moving the C-Lens the same amount in the opposite direction. In the second configuration, the fiber is tilted itself by a small angle. Figure 5-4 shows the 3D layout of the Zemax modeling for on-axis and off-axis models.

I analyzed the spot size and lateral resolution of the optical probe using the Zemax Z-detector and detector view tools in non-sequential mode. The Z-detector is defined to be 0.16 mm in width and 4 mm in depth with 160 and 100 pixels, respectively when placed 2.25 mm from the C-Lens. [91] These dimensions provide 1 μm resolution along the width for spot size and lateral resolution

measurements. The number of pixels along the depth is set to 100 to only provide the imaging range and not the resolution. As the beam is off-axis in both configurations, the Z-detector should be moved synchronously, which defines the field of view for imaging. The length of MMF fiber is optimized at 3.235 mm. [91] The distance between the MMF and C-Lens entrance plane is 3 mm.

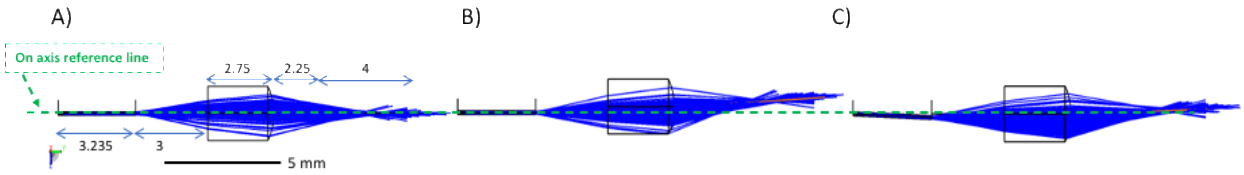

Figure 5-4: 3D layout of Zemax modeling of optical probe. A) on-axis configuraiton, B) off-axis configuration #1 by moving the C-Lens 0.2 mm perpendicular to optical axis. C) off-axis configuration #2 by tilting the MMF fiber 2-degrees.

The Z-detector and detector view tools in non-sequential mode in Zemax allows for analysis of the field intensity distribution along the imaging-depth as shown in Figure 5-5A. I have analyzed the Z-detector data in MATLAB (R2017b, Mathworks, Natick, Massachusetts, U.S.). Figure 5-5B shows the intensity distribution along the imaging-depth where 0 μm refers to the end of the Z-detector and 4000 μm is the detector window close to the C-Lens. I plotted the profile at different depths as shown in Figure 5-5C to obtain a focus size by measuring a full width at half-maximum (FWHM).

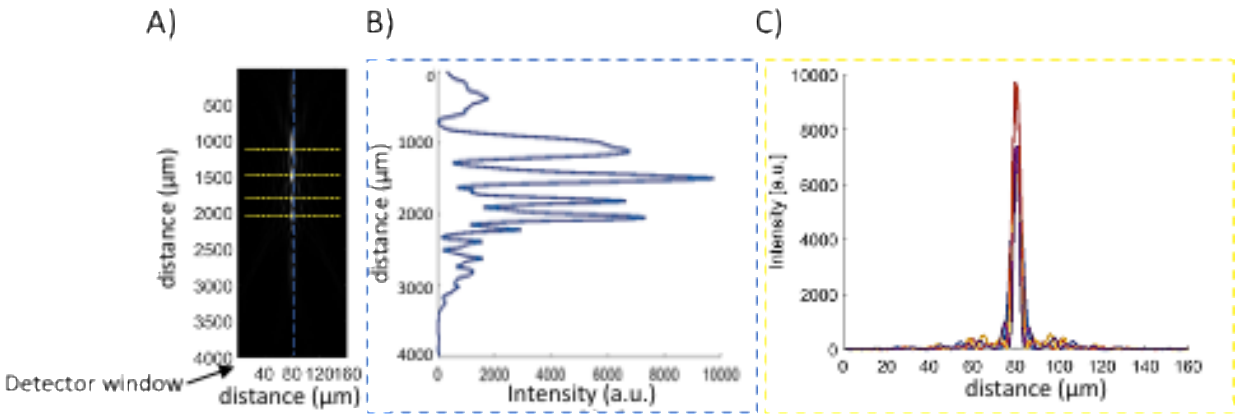

Figure 5-5: A) Z-Detector viewer, B) intensity profile along depth-imaging, C) profiles at different depths along depth-imaging to measure FWHM as spot size at different depths.

5.2.2 Probe Design

The probe design consists of a quartered piezoelectric tube to scan the fiber and generate linear scanning of the optical beam on tissue. The piezoelectric tube, optical fiber, and a lens are housed inside a stainless-steel tube that can be inserted into the speculum to access the cervix.

The piezo tube (Pi Ceramic, Lederhose, Germany) is made from a lead zirconate titanate ceramic (PZT) with an inner diameter (ID) of 0.9 mm, an outer diameter (OD) of 1.5 mm, and a length of 13 mm. On the outer circumference, four radial electrodes are attached which excite and create oscillations of the fiber cantilever in the corresponding two orthogonal directions. However, only one pair of electrodes is used to produce a linear-mode scanning trajectory. The PZT tube is fixed with a 3D printed non-conductive ring of polymethyl methacrylate with an ID and OD of 1.5 and 1.8 mm, respectively, centered in the stainless steel tube. The fiber is centered in the tube with a ring jewel bearing (Swiss Jewel, Philadelphia, Pennsylvania) and fixed with UV epoxy for optimal rigidity. The piezoelectric actuator is driven by a waveform using one channel from a three-

inverting and non-inverting channels amplifier (TD250-INV, Micromechatronics, State College, USA). The output voltage after amplification is at a maximum of 40 V peak amplitude A.C., within the recommended limit from the International Electrotechnical Commission medical electrical apparatus standards [44].

The fiber deflection is measured using a consumer webcam CCD sensor fitted with a microscope objective to measure the field of view (FOV). Here, I assume the probe reaches a maximum FOV of 0.8 mm. The line scan camera in the micro-OCT system has an acquisition speed of $F_{ALine} =$ 80 kHz, so the maximum resonant frequency f to achieve sufficient sampling is given by [42]

$$f = \frac{F_{Aline} . \Delta x_{min}}{FOV} \quad (5.1)$$

Where $\Delta x_{\min}$ is the minimum sampling distance. To avoid undersampling, the pixel spacing has to satisfy the Nyquist criterion. The maximum detectable spatial frequency depends on the NA of the optics and the center wavelength λ which determine the lateral resolution (δx) of the imaging system. I have used the FWHM value from the Zemax modeling of the optical probe to calculate $\Delta x_{\min} \sim \delta x/2$. In addition, the scanning resonance frequency of the fiber cantilever is calculated using Eq. 5.2 based on fiber length, diameter and mechanical properties estimated using the fixed-free cantilever formula [44],[92] where E is Young's modulus, ρ is mass density of the fiber, R is radius and L is the length of fiber cantilever.

$$f = \frac{3.52}{4\pi} \sqrt{\frac{E}{\rho}} \frac{R}{L^2} \quad (5.2)$$

For the 600-950 nm wavelength bandwidth of the micro-OCT system, a single-mode fiber (SMF) (S630-HP, Thorlabs, Newton, New Jersey, USA) is used for light delivery. A segment of a

multimode fibre (FG105LCA, Thorlabs, Newton, New Jersey, USA) is spliced with the SMF as a single-mode-multimode (SMM) fiber element, which extends the depth of focus and increases the depth-imaging capabilities of the probe by more than one order of magnitude. [90] Both SMF and MMF fibers are composed of fused silica with E = 73 GPa and ρ = 2.2 Mg/m^3.

The fiber is aligned to a 1.8 mm diameter C-Lens (CASIX, Fuzhou, Fujian, China) with a focal length of 3 mm and NA of 0.29. The entire device is encapsulated in fluorinated ethylene propylene tubing and sealed using medical epoxy to attach a glass window top with a thickness of ~170 μm, such that it is watertight and there are no exposed conductive surfaces.

5.3 Results

5.3.1 Optical probe Modeling

I modeled the optical probe for both on-axis and off-axis configurations in Zemax and the 3D layouts are shown in Figure 5-4. In configuration #1, the C-Lens was moved 200 μm which resulted in the Z-detector moving about 400 μm and tilting about 3-degrees. In configuration #2, I tilted the fiber 2-degrees resulting in the Z-detector moving about 120 μm and tilting 2-degrees.

The Z-Detector tool works as a camera along the depth-imaging (z) axis and visualizes the field intensity distribution along the depth-imaging path as it is shown in Figure 5-6A-C. Figure 5-6D-E show the depth intensity profile along the z-axis to analyze the intensity distribution for on-axis and off-axis configurations. The intensity profile shows the depth-imaging range along the Z-detector. I plotted the profile perpendicular to the z-axis at different depths as shown in Figure 5-6G-I to measure the FWHM, which defines the spot size and lateral resolution along the depth-

imaging. The FWHM measurements at different positions along the Z-detector are shown in Table 5-1, Table 5-2 and Table 5-3 for both on-axis and off-axis configurations.

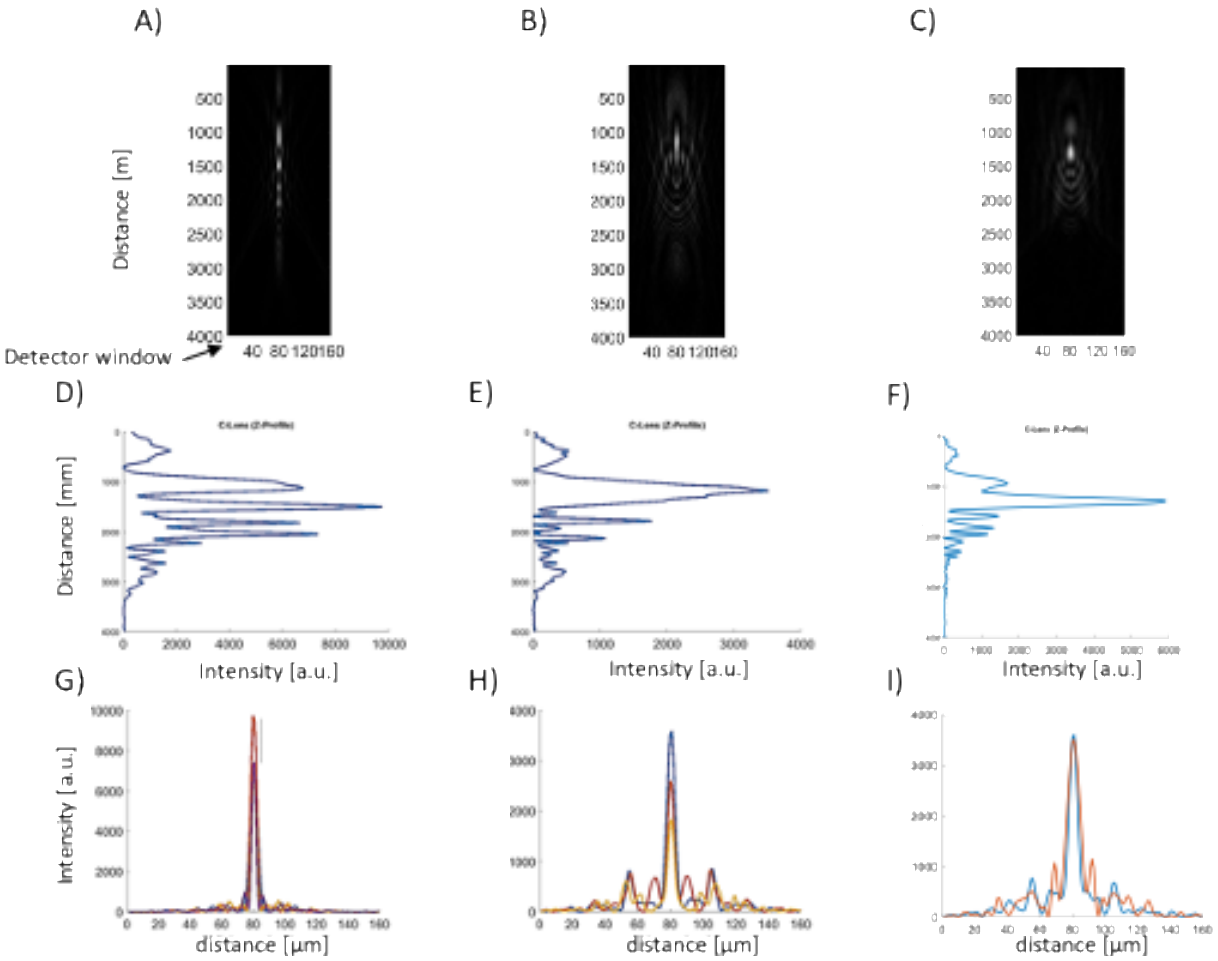

Figure 5-6: Modeling optical probe in Zemax. Z-Detector viewer for on-axis modeling (A), configuration 1 off-axis modeling (B) and configuration 2 for off-axis modeling (C). D-F show intensity profile along the Z-detector, G-I) plots profile along x-axis at different depths to measure the FWHM.

Table 5-1: FWHM measurements at different depths for on-axis optical probe

Depth (um)	FWHM (um)
1121	5
1498	3
1818	3
2048	3

Table 5-2: FWHM measurements at different depths along Z-detector for off-axis configuration #1

Depth (μm)	FWHM (μm)
1177	4
1288	3
1778	3

Table 5-3: FWHM measurements at different depths along Z-detector for off-axis configuration #2

Depth (μm)	FWHM (μm)
1210	5
1379	8

5.3.2 Probe Design

The schematic design of the forward-viewing cervical micro-OCT probe is shown in Figure 5-7A, the figure is not to scale. Figure 5-7B shows the SolidWorks design of the probe. In this chapter, I designed and modeled the probe to be used for cervical imaging applications.

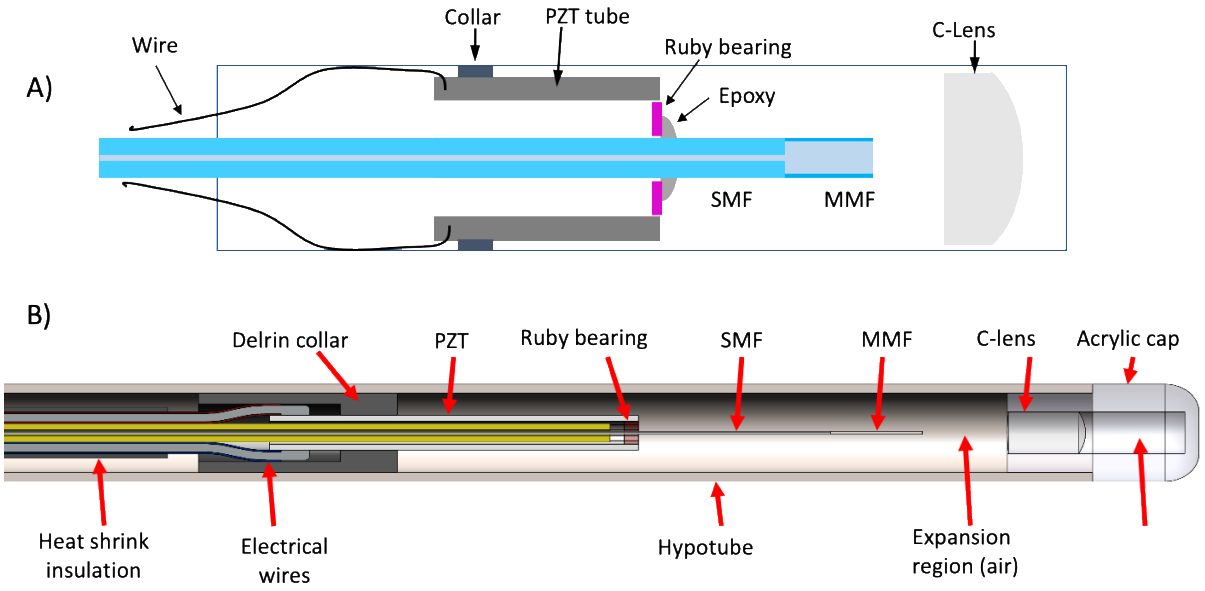

Figure 5-7: A) Schematic diagram of the forward-viewing cervical probe (not to scale), B) SolidWorks design of the probe (to scale).

The length of the fiber cantilever depends on the resonant frequency which is dependent on the camera speed, FOV and lateral resolution. The calculated resonant frequency and length of the fiber cantilever based on Eq. 5.1 and Eq. 5.2 for FOV = 800 μm, δx = 5 μm at two camera speed s of 80 kHz and 200 kHz, is shown in Table 5-4.

Table 5-4: Camera speed and fiber scanning parameters

Camera speed (kHz)	Resonant frequency (kHz)	L (mm)
80	0.25	20.5
200	0.625	13

The probe has a minimum length of 31 mm based on the length of the piezoelectric tube, fiber cantilever, C-Lens, and the distance between the fiber and C-Lens. The piezoelectric tube, optical fiber, and a C-lens can be housed inside a stainless-steel tube with an ID of 1.8 mm. A longer rigid length of probe may be employed to help maneuver the probe for cervical imaging.

5.4 Discussion and Future Directions

I provided a micro-OCT probe design optimized for cervical imaging during colposcopy. Zemax modeling of this design shows a lateral resolution of 3 to 8 μm, which is comparable to side-viewing micro-OCT probes. [90],[93],[94] The DOF is about 900 to 200 μm for on-axis and off-axis imaging respectively, which provides a good imaging depth for cervical assessment. These results were obtained at 800 nm. I have repeated the simulation in Zemax for seven wavelengths to cover the broadband supercontinuum range of the light source. The field intensity distribution along the depth-imaging on the Z-detector are shown in Figure 5-8A-G for wavelength values of 650, 700, 750, 800, 850, 900 and 950 nm. Figure 5-8E shows the overlaid field intensity distribution along the depth-imaging on the Z-detector from these seven wavelengths values. Although the broad bandwidth light source has a Gaussian spectral shape, it is not considered in overlaying the seven wavelengths intensity distribution in Figure 5-8E. As the wavelength

increases it will penetrate further into the tissue, focus deeper, and will have more modes for each wavelength. As such, it is expected the DOF will be improved.

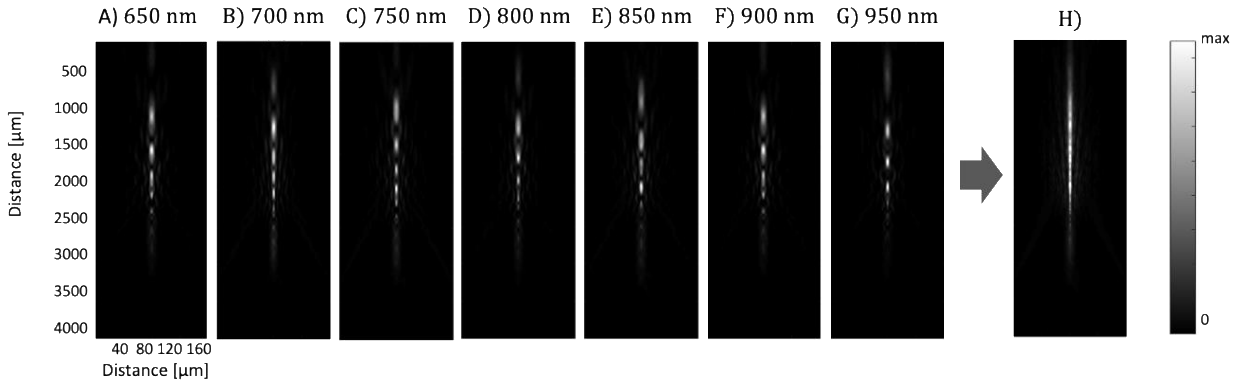

Figure 5-8: Z-Detector viewer for on-axis model at different wavelength values (A-G). H shows the overlayed field intensity distribution along the depth-imaging on the Z-detector from all seven wavelengths values.

I have repeated the seven wavelengths' measurement for the two off axis configurations. Figure 5-9A-G show field intensity distribution along the depth-imaging on the Z-detector for wavelength values of 650, 700, 750, 800, 850, 900 and 950 nm, and Figure 5-9E shows the overlaid field intensity distribution along the depth-imaging on the Z-detector. As the wavelength increases it should penetrate further into the tissue and focus deeper while the resolution should remain the same. For off axis configurations, it looks the expected DOF improvement is not the same as on axis configuration. In addition, resolution is also degraded for off-axis configuration which would

result a part of the image field be blurred. Degradation of the focus may limit the resolution at the edges of the FOV or limit the size of the usable FOV.

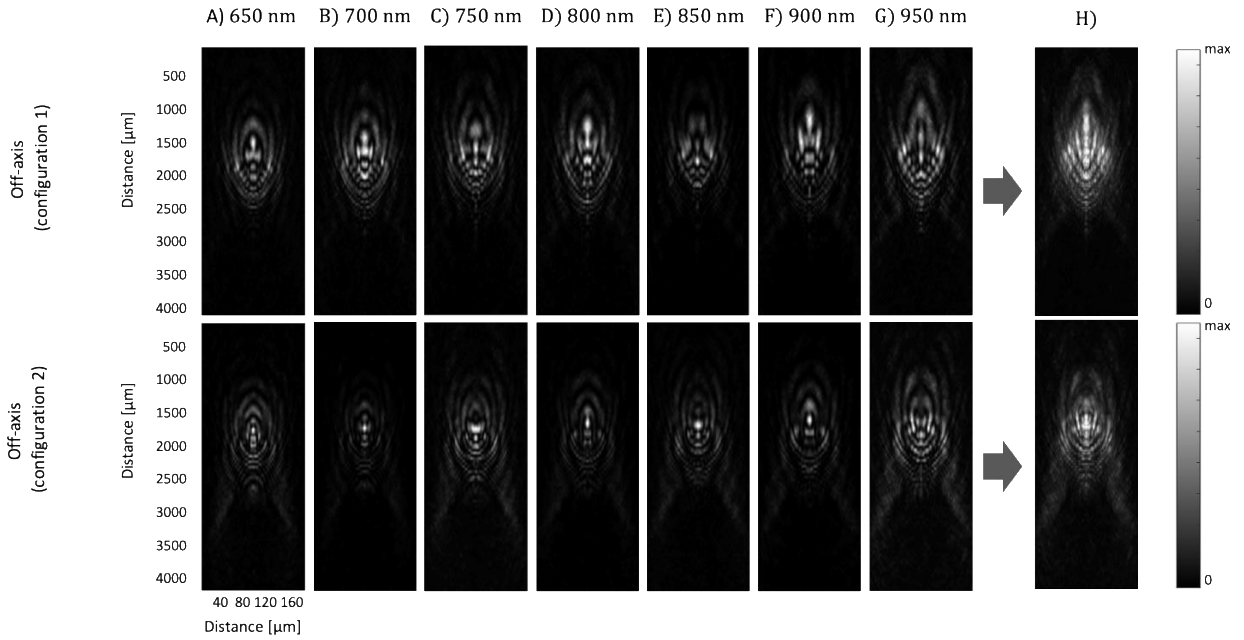

Figure 5-9: Z-Detector viewer for off-axis configurations 1 and 2 at different wavelength values (A-G). H shows the overlayed field intensity distribution along the depth-imaging on the Z-detector from all seven wavelengths values.

There are forward-viewing OCT probes using a piezoelectric tube for scanning fiber based on SS-OCT. [44]**,** [42] These approaches allow for high-speed 3D OCT; however, their resolution is limited. I modeled and designed a forward-viewing micro-OCT probe based on SD-OCT. The SD-OCT imaging speed is limited by the camera speed, which in turn, limits the FOV. In my design, I set the scanning fiber to be 1 dimensional (1D) scanning where it can generate a circular or linear scan pattern as shown in Figure 5-10. A circular scan would allow a much wider scanning range compared to the linear scan. However, the circular scan may be confusing to interpret, and our collaborating clinician preferred the linear mode. The cervix morphology changes between the

ectocervix which is lined with stratified squamous epithelium and the endocervical canal which has only simple columnar epithelium. In a circular scan pattern, it is challenging to tell where the scan is obtained from and thus harder to interpret the images. Hence, the linear scanning mode is preferred. This configuration also allows for dynamic micro-OCT, which enables cross-sectional images of intracellular dynamics with dramatically enhanced image contrast. [95] This approach solves the aforementioned issues for the SD-OCT system. Lastly, linear scans are more readily compared to H&E histological slides.

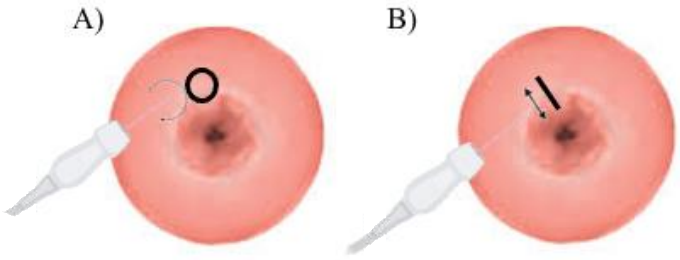

Figure 5-10: 1D scanning: A) a circular and B) linear scanning mode.

The optical design presented may have significant utility for future endoscopic applications. Experimental verification remains necessary to validate the theoretical work presented here. Spliced SMF and MMF fiber has been successfully used for micro-OCT with a spacer and GRIN lens as focusing optics [90]. Here, we have selected the C-Lens over a GRIN lens in order to maintain the lateral resolution for off-axis scanning fiber. The C-Lens approach has other advantages including low cost, low insertion loss in long working distance, and wide working distance range. After initial proof of concept testing, the design may be modified in terms of size and optical characteristics as needed for specific applications. This could include using a smaller

piezoelectric tube or smaller focusing optics in order to make a smaller probe. A handheld probe casing would also be needed to ensure compatibility and manoeuvrability within the speculum.

5.5 Conclusion

In conclusion, I have demonstrated a new design for a forward-viewing fiber scanning micro-OCT probe. Using a high speed, A-Line rate camera would allow for faster image acquisition, which might allow for *in vivo* 3D micro-OCT, or shortening the fiber and the rigid length of the probe. In the future, the forward-view imaging micro-OCT probe will be built, tested, and further developed for implementation in cervical imaging. *In vivo* clinical trials will be required to assess the final design.

Chapter 6: A NIR Supercontinuum Light Source for NIR Micro-OCT Imaging

6.1 Introduction

Optical coherence tomography (OCT) is a non-invasive, rapid, imaging technology based on the principles of white-light interferometry that generate depth-resolved cross-sectional volumetric images of complex structures such as biological tissue. The imaging performance of an OCT system is dependent upon the sensitivity of the system and the achievable imaging resolution in both the lateral and axial dimensions. [96] Both sensitivity and resolution are, to a large extent, determined by the spectral characteristics of the light source. The key performance criteria of an OCT source are spectral bandwidth, spectral line shape or structure, power level, intensity stability, spatial and temporal coherence. A thorough discussion of these performance criteria has been reviewed by Fercher. [97],[98] Super-luminescent diodes (SLDs) are commonly used in commercial OCT instruments because the amplified spontaneous emission from the SLD produces temporally stable, low-coherence light with low intrinsic noise and high sensitivity. Since the axial resolution is inversely proportional to the optical bandwidth, the narrow bandwidth produced by SLDs limits the axial resolution to approximately 10 μm. Since higher bandwidth sources are able to achieve greater axial resolution, supercontinuum sources are being increasingly used in spectral-domain OCT (SD-OCT) due to their high spectral powers and large bandwidths resulting in ultrahigh-resolution OCT. [32] Moreover, It has been seen that the NIR-OCT at 1300 nm has advantages over visible-OCT in terms of the penetration depth into scattering media such as biological tissues. To achieve greater imaging depth in the biological tissues, light sources in the 1300 nm spectral band are commonly used for conventional OCT because the light scattering is reduced at 1300 nm compared to the visible OCT. [99],[100],[101],[102] A supercontinuum light

source in the 1300 nm spectral band is needed in order to allow for high resolution micro-OCT as well as deep tissue imaging.

Most commercially available supercontinuum sources generate octave-spanning bandwidths by a cascade of nonlinear processes that may also generate strong phase and amplitude dependences during soliton formation.[103] Consequently, supercontinuum sources are inherently noisy in contrast to other common lower bandwidth OCT sources such as ultrafast laser sources and SLDs and their noise characteristics are inherently difficult to predict and must be measured directly.[104],[105],[106]

Hamamatsu recently developed a broad bandwidth supercontinuum light source centered in the 1000-2000 nm NIR region that may significantly improve the imaging depth while maintaining a high axial resolution, resulting in new applications for clinical imaging. I report findings on the spectral intensity fluctuations, degree of coherence in the spectrum and OCT image quality by acquiring images from a solid validation standard and fresh tissue while using the Hamamatsu source. The performance is compared to the 800 nm supercontinuum source used to acquire high-resolution OCT images in the Tearney laboratory [32] and a low-noise, low-coherence SLD source commonly used for OCT imaging.

6.2 Methods

6.2.1 Broadband OCT Sources

I compared the OCT performance of the Hamamatsu supercontinuum source (L150977MOD2, Hamamatsu) to those of a super luminescent diode and NKT source (SuperK Extreme EXR-1, NKT Photonics). SLD sources are well characterized low-coherence sources with narrower

bandwidths resulting in a lower axial resolution. The NKT source produces a large bandwidth (500-2000 nm) at 80 MHz with 200-300 picosecond pulses. Using the bandwidth spanning 650-925 nm, the Tearney laboratory has previously demonstrated the NKT source can achieve a high axial resolution of 1-2 μm in air [32] and have used the μOCT system for imaging tissue *ex vivo* [107],[70] and in clinical studies [93],[94]. Spectral data from the Hamamatsu supercontinuum and SLD are acquired using the same instrumentation and parameters. Since the region of the NKT source used for OCT images is 650-925 nm, spectral data was collected on an instrumentation described previously. [32]

6.2.2 Characterization of OCT source metrics

To evaluate the performance of each OCT source, the spectral output is directed into a NIR spectrometer (C1300-1300/500-147-SG2K, Wasatch Photonics Inc.) via a single-mode fiber (P3-SMF28E-FC-2, Thorlabs) as shown in Figure 6-1.

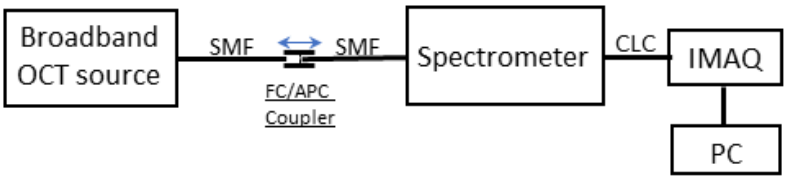

Figure 6-1: Schematic of OCT source spectral measurement. Output from a broadband width source is coupled into a spectrometer via a single mode fiber (SMF). The spectral intensity is adjusted by varying the coupling of the FC/APC connection to avoid saturation of the camera.

The OCT spectrometer is equipped with an InGaAs linear array detector (GL2048R, Sensors Unlimited) with 2048 pixels having a maximum sampling rate of 147 kHz. The detected signals

are digitized at 12-bit resolution and transferred to a personal computer through a camera link interface and image acquisition frame grabber board (Bitflow Axion CL, PCIe Gen 2.0 x4). The spectrometer grating was chosen to give a 500 nm spectral window (950-1450 nm) which translates into a spectral resolution of ~0.24 nm/pixel. The sensor's bit depth is 12-bit (4096). To avoid saturation of the camera's intensity, the SMF-to-SMF coupling is adjusted to reduce the intensity. After changing the amplifier current, the Hamamatsu source is allowed to stabilize for several minutes before collecting a set of spectral data. A dataset consists of 1024 continuously recorded spectra acquired at an A-line rate of either 147 kHz or 20 kHz.

6.2.3 Spectral-Domain OCT instrumentation

A spectral-domain OCT instrument with a centre wavelength of 1300 nm was constructed to acquire high-resolution OCT images. A schematic of the SD-OCT system is shown in Figure 6-2 and is based on the optical design principles described previously for a 1-μm resolution SD-OCT system having a central wavelength of 800 nm. [32] Briefly, the SD-OCT system is based on a Michelson interferometer design were the light source is delivered via a single-mode fiber (P3-SMF28E-FC-2, Thorlabs) and directed to a non-polarizing 50/50 beam splitter (Thorlabs BSW29R). The collimated beam, having a diameter of 6.7 mm, is split into two wavefronts by a 45° rod mirror (#54-092, Edmund Optics Inc.). The central circular wavefront is directed to the reference arm and the annular wavefront is sent to the sample arm. The reference arm path consists of a neutral density filter for adjusting the reference power, a focusing lens and mirror. The collimated annular beam in the sample arm is raster scanned across the sample using a pair of galvanometer scanners (GVS112, Thorlabs Inc.) driven by an analog output board. Optics in both arms are matched to balance the dispersion. Light reflected from the reference and backscattered

from the sample arms are recombined at the beamsplitter and focused into a spectrometer (C1300-1300/500-147-SG2K, Wasatch Photonics Inc) via a single-mode fiber (P3-SMF28E-FC-2, Thorlabs). The signal is digitized by an image acquisition frame grabber board (Bitflow Axion CL, PCIe Gen 2.0 x4). The speed of transverse (x,y) scanning mirrors set the frame rate of data acquisition at 20 Hz. Software written in C++ was used to acquire data and synchronize the scanning galvanometer mirrors and camera acquisition.

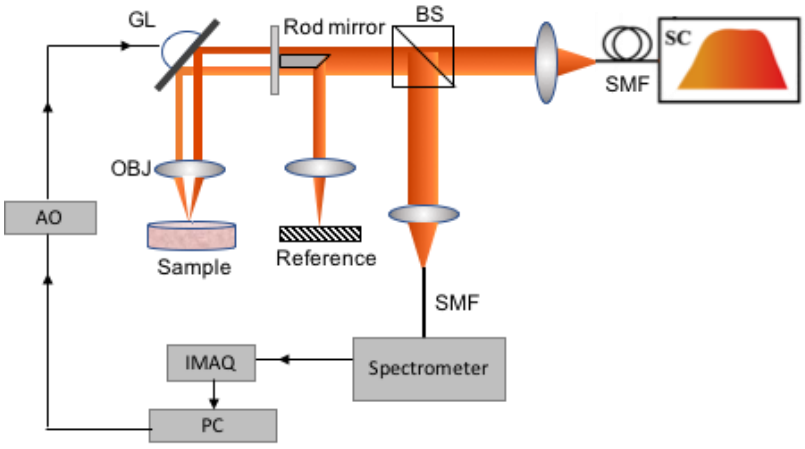

Figure 6-2: Schematic of micro-OCT system centered at 1300 nm. AO: analog output board; BS: beam splitter; GL: galvanometer; IMAQ: image acquisition board; SMF: single mode fiber; PC: personal computer.

6.2.4 OCT Processing

The post-processing of the raw SD-OCT data involves subtracting a background spectrum from all raw spectral data acquired. The background spectrum is acquired by averaging multiple spectra (n=50) while blocking the sample arm. The background-subtracted spectra are then converted from

wavelength space (λ) to the wave-vector space ($k = 2\pi/\lambda$) and corrected for spectrometer non-linearity through linear interpolation. The interpolated spectral data is then Fourier transformed to obtain the complex depth-resolved back-scattering profiles. Cross-sectional images are generated by taking the absolute value of the complex depth-resolved back-scattering profiles. SD-OCT cross-sectional gray-scale images are displayed using a logarithmic grayscale look-up table.

6.3 Results

6.3.1 Light Source Spectral Evaluation

To assess the performance of the Hamamatsu supercontinuum source, I evaluated the spectral intensity fluctuations and intra-spectral correlations operating at an amplifier current of 1640 mA and compared it to the performance of both a low-coherence, low-noise SLD and an NKT supercontinuum source that is used in the Tearney laboratory for high-resolution OCT imaging. Representative results acquired at an A-line rate of 147 kHz are shown in Figure 6-3.

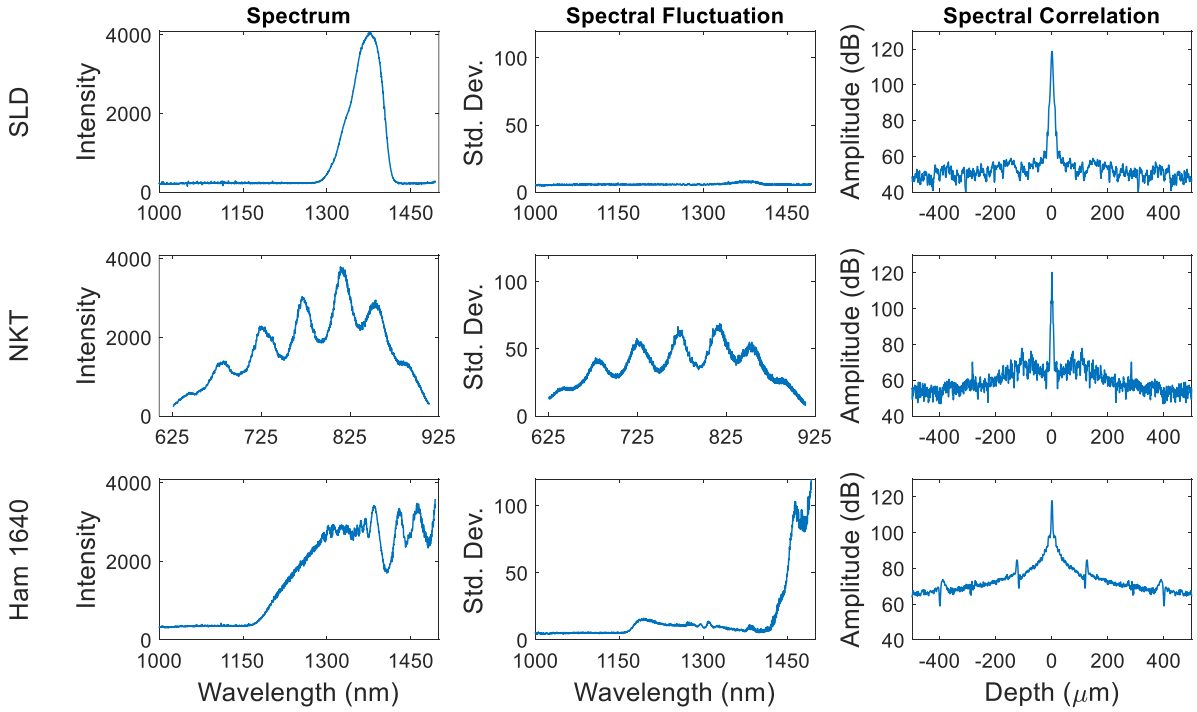

Figure 6-3: Characterisation of three light sources NKT, SLD, and Hamamatsu operating at 1640 mA amplification current are compared. The SLD and H1640 mA data were obtained at 147 kHz A-line rate. The NKT spectrum was collected by blocking the sample arm of the OCT system at a 16 kHz A-line rate.

Temporal intensity fluctuations are assessed by constructing the standard deviation from 1024 continuously acquired spectra. Most SLD sources produce a highly stable (intensity) power output that is typically better than 0.01 dB resulting in the observed low wavelength-dependent standard deviation (Figure 6-3). Since the shape of the standard deviation spectrum is similar to the SLD's intensity output spectrum, this suggests that the frame-to-frame intensity fluctuations are primarily due to detector shot noise. Similar to the SLD case, the NKT intensity and standard deviation spectra have similar shapes, however the frame-to-frame intensity fluctuations are significantly larger suggesting that the standard deviation is dominated by small fluctuations in the pump pulse

that become magnified due to nonlinear interactions. Finally, the measured standard deviation is in agreement with the power stability of ±0.5% as reported by NKT. [108] The standard deviation spectrum of the Hamamatsu source is complicated. Frame-to-frame fluctuations are low over the lower 1200-1400 nm region (even though there is high spectral intensity) and are not significantly higher (< 5x) than that of the SLD. However, the 1400-1500 nm band exhibits unexpected large temporal deviations. Examining consecutive frames reveals the spectral modulation is not time-independent over this band but rather appears to change both the spectral phase and amplitude between frames, as shown in Figure 6-4. This temporal instability results in a large standard deviation over the 1400-1500 nm band.

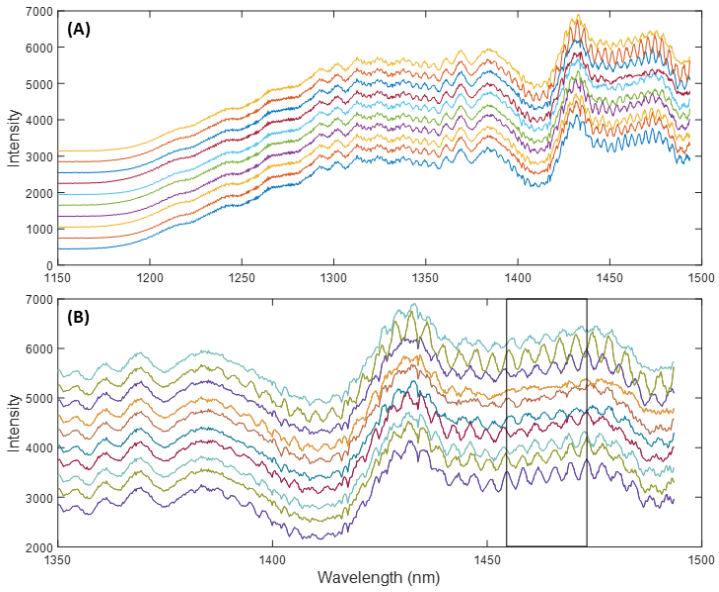

Figure 6-4: Consecutively acquired spectra from the Hamamatsu source operating at an amplifier setting of 1640 mA. Spectra (n=10) are vertically offset by 300 for visibility. A.) Spectra indicate minimal frame-to-frame intensity fluctuation in the 1200-1400 nm band. Over this region, the standard deviation has a maximum value of 10 (~1190 nm), which is approximately 5 times greater than the SLD maximum. B.) Spectra over the 1350-1500 nm

band shows strong spectral modulations that appear to change the phase and amplitude of the modulation between frames. Vertical lines are intended as a reference.

To estimate degree of spectral correlation, the spectrum is transformed via a fast Fourier transformation (FFT) from k-space to z-space, which provides a depth-resolved point spread function (PSF). If the intrinsic noise in the spectrum is white or uncorrelated, the noise floor in the z-domain would be flat and the noise level can be inferred to be a variance in the k-domain. The SLD depth profile exhibits a near-ideal behavior for a low-coherence source. There is a central DC feature centered at a depth of z=0 as the correlation function rapidly falls off to the noise floor. The width of the central peak is indicative of the coherence length of the source and is also taken as an estimate of the axial resolution. The NKT source shows an overall narrower peak with a measured coherence length of ~1.4 μm in air. However, there is a strong satellite peak at a depth of ± 17 μm and a small shoulder, likely corresponding to the ripple. Finally, the Hamamatsu source shows a slower higher noise floor (60 dB) with visible satellite peaks appearing at depths of 7, 15, 100 and 158 μm. This correlated noise will be present in OCT images as a horizontal line that cannot be easily removed via post-processing methods such as simple background subtraction without distorting the reconstructed OCT image.

The spectral output of the Hamamatsu source was examined at amplifier current settings of 1680, 1640, 1580, 1520, 1480 and 1400 mA to determine the optimum conditions for OCT imaging (1640 and 1480 mA were values suggested by Hamamatsu). The entire set of amplifer current values acquired at 147 kHz as well as 20 kHz. The spectra look similar and there were no differences between the two acquisition speeds on the spectrum. Representative data acquired at 20kHz are shown in Figure 6-5. The spectral line shape changes considerably as the power

increases and periodic spectral modulations are more apparent on the red-edge of the spectrum at higher amplifier settings. The depth point spread function has satellite peaks at all power settings distributed mostly around the center peak (z=0) at low values, however prominent satellite peaks appear at approximate depths of 100, 160 and 360 µm. Based on these results, I have collected OCT images at four amplifier currents:1480, 1580, 1640 and 1680 mA.

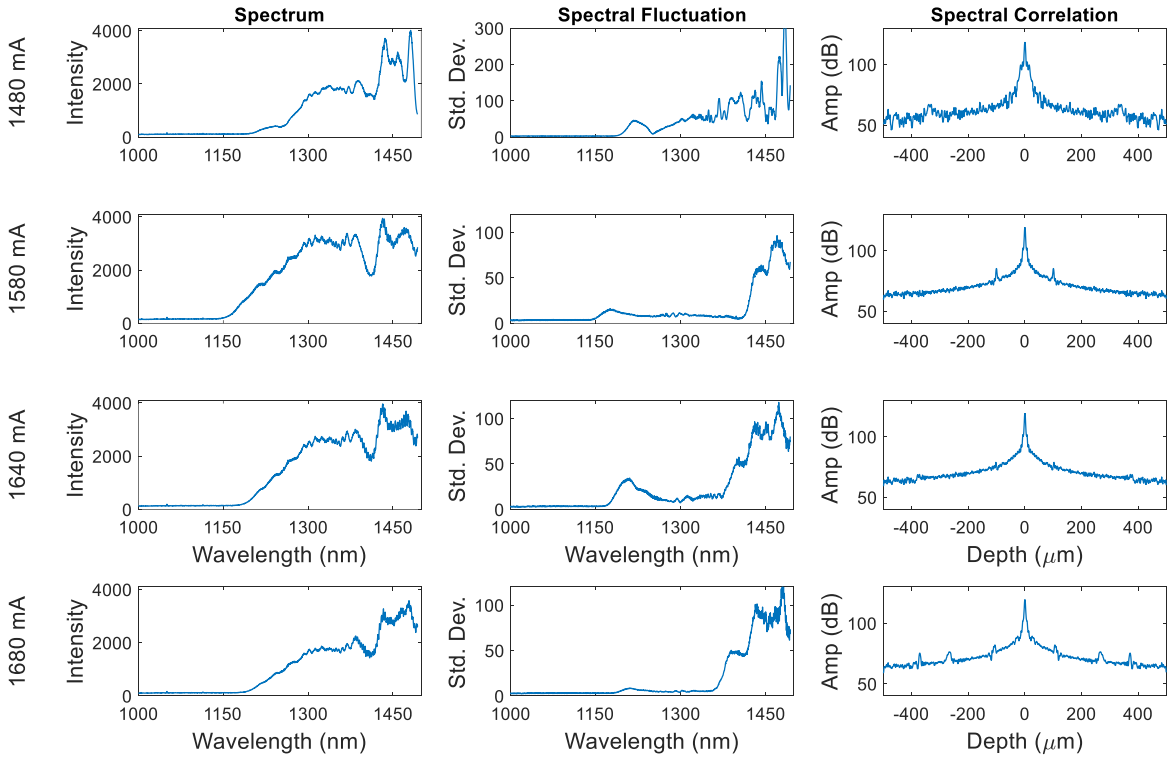

Figure 6-5: Characterization of the Hamamatsu source at different amplifier currents. Spectra obtained at 20 kHz. Note the change in the y-axis range for the 1480 mA spectral fluctuation data.

The roll-off was measured by gradually increasing the sample distance from zero delay in increments of 25 µm steps to a total depth of 350 µm in air. The roll-off value is determined where

the PSF value has dropped by 6 dB as shown in Figure 6-6. Measured results are summarized in Table 6.1.

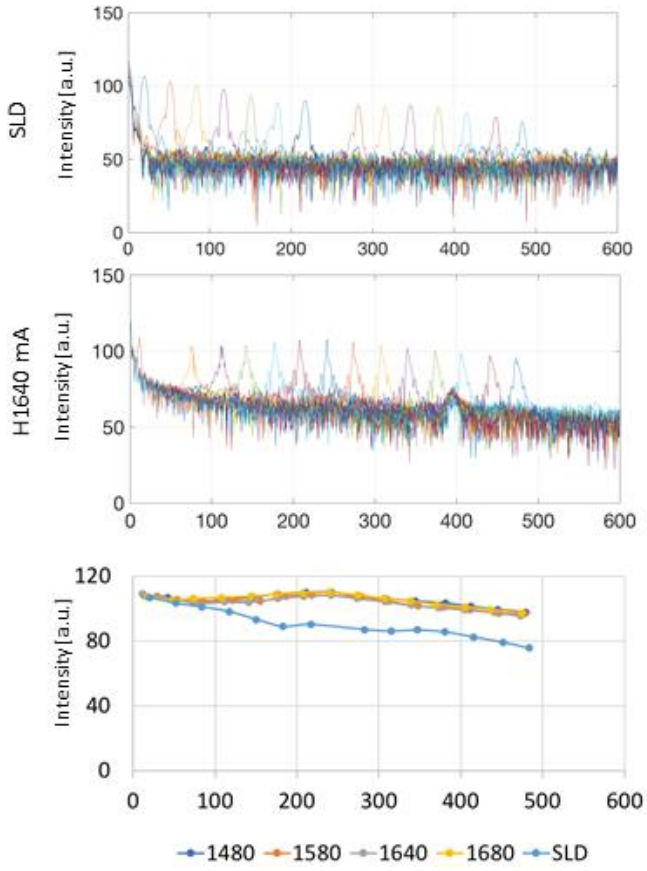

Figure 6-6: Roll-off measurement for (a) SLD and (b) Hamamatsu (1640 mA) sources at 1640 mA. c) Roll-off profiles as a function of depth for SLD and Hamamatsu at 1480, 1580, 1640 and 1680 mA.

Table 6.1 Summary of OCT source characteristics

Light sources	$\lambda 0$[a] [nm]	BW[b] [nm]	SNR[c] [dB]	Roll-off[d] [μm]	l_c[e](μm)	Satellite Peaks[f] (μm)
NKT	800	160	90	NA	1.4	
SLD	1330	65	NA	64.51	7.8	
H1480	1327	226	89	369.15	3.1	7.4(0.091), 15(0.058), 33(0.011), 53(0.004), 158(0.002), 340(0.001)
H1580	1327	226	NA	317.85	2.8	1.9(0.115), 7.4(0.060), 101(0.007)
H1640	1327	226	NA	312.43	2.8	1.9(0.161), 6.6(0.062), 12(0.024), 17(0.015), 24(0.011), 102(0.004), 158(0.003), 360(0.001)
H1680	1327	226	NA	387.81	2.8	1.9(0.210), 7.4(0.072), 12(0.024), 14(0.026), 17(0.015), 24(0.015), 27(0.014), 31(0.012), 39(0.010), 110(0.007), 268(0.003), 371(0.003)

a. Central wavelength (λ_0)
b. Bandwidth (BW) defined as full width at half maximum
c. Signal to noise ratio (SNR)
d. Roll-off: OCT imaging depth in air where the PSF drops by 6 dB
e. Coherence length (l_c) defined as full width at half maximum value of the central peak in the depth point spread function
f. Depth of satellite peaks present in the PSF profile reported with (amplitudes) relative to the central peak (1.000)

Hamamatsu and SLD spectra were recorded at 20 kHz using the same camera. NKT data was recorded at 16 kHzon a separate system.

6.3.2 OCT Image of Calibration Standard

The APL-OP01 OCT phantom (Arden Photonics Ltd, Clearwater FL) is a calibration standard that can be used to qualitatively and quantitatively characterize the imaging performance of an OCT system. [109] The phantom contains four geometrical patterns inscribed within a silica substrate

(n=1.45). The patterns are formed by inducing localized changes in the refractive index at each site. All patterns contain 8 layers separated by 75 μm with a 100 μm distance between the surface and first layer. For this evaluation, I imaged the 'distortion pattern,' which consists of an array of sites spaced 100 μm ×100 μm in the x-y plane with layers located 100 μm below the surface in the OCT image.

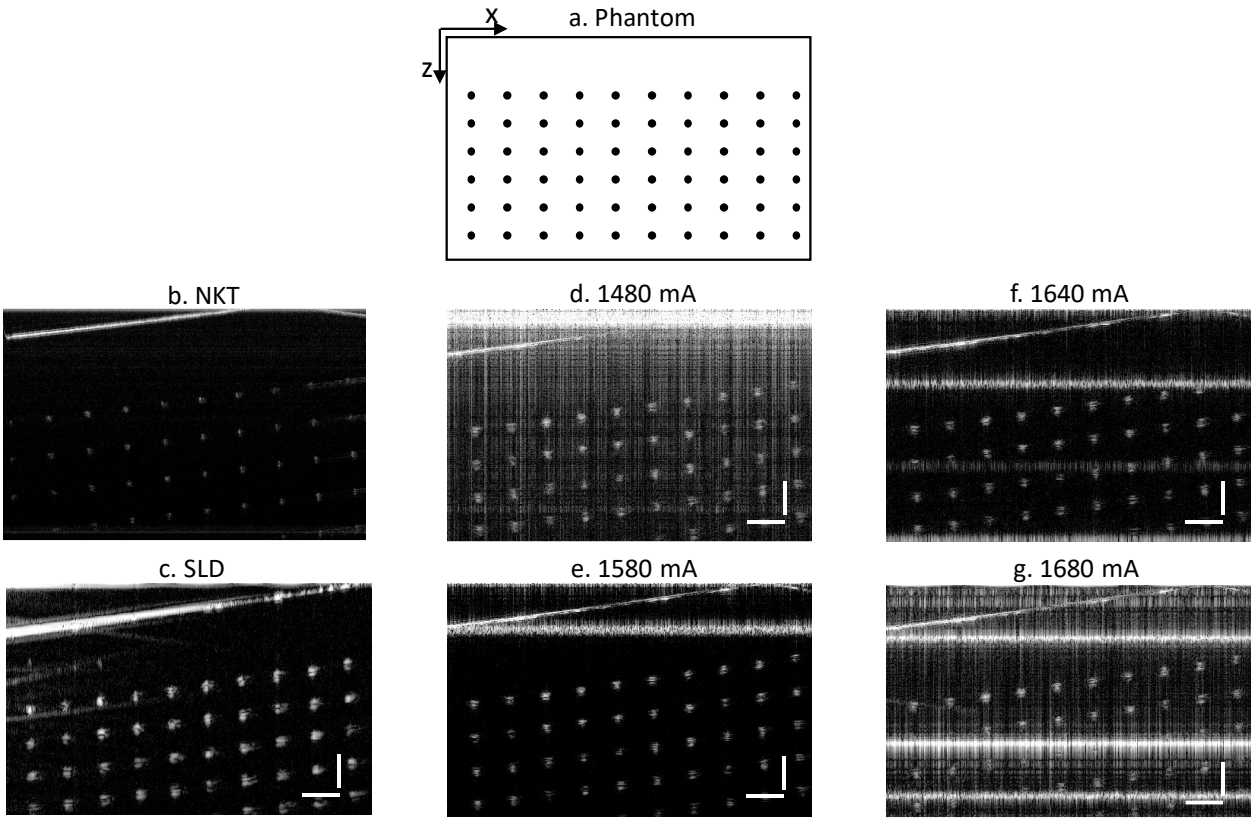

Figure 6-7: OCT images of the distortion pattern in APL-OP01 OCT phantom (a) test pattern. (b) Image from the NKT, (c) SLD and (d-g) Hamamatsu sources are shown. Images acquired at different amplifier currents are indicated. The diagonal line is the due to the top surface of the OCT phantom. Scale bars on the OCT images are 100 μm in the x- and z-directions.

OCT images of the APL phantom are shown in Figure 6-7 for all sources and at a set of amplifier currents. Hamamatsu OCT images contain artifacts that are expected based on the axial point spread function, as shown in Figure 6-5. Comparison of the scattering centers finds that the NKT image has the smallest diameter in the z-direction at ~16 μm followed by Hamamatsu (~19 μm) and SLD (~29 μm). The OCT image obtained at 1580 mA shows best combination of high contrast and minimum artifacts compared to other amplification current values.

6.3.3 *Ex vivo* OCT Imaging of Tissue

Representative OCT images have been acquired from *ex vivo* kidney, lung, adipose and esophageal tissues obtained from a swine less than 12 hours postmortem using a NKT-based micro-OCT system, and a NIR-SD system coupled to either the SLD or Hamamatsu sources. Images were taken with Hamamatsu source at amplifier settings of 1480, 1580, 1640 and 1680 mA. The NKT-based micro-OCT is the gold standard for 1 μm resolution OCT with a sensitivity of ~90 dB. The SLD-based NIR SD-OCT instrument provides an extremely low-noise source at significantly lower axial resolution. I attempted to maintain the registration of the tissue sites between sources and histology. Standard H&E histology was taken from the tissue to provide representative morphological and cellular features.

Figure 6-8-11 show images of the four tissues. Artifacts visible in the depth point spread function are present in the OCT images and result in images that are difficult, and in some cases impossible, to interpret qualitatively. There is a demonstrated increased imaging depth using the SLD and Hamamatsu sources centered at 1300 nm over the 800 nm NKT system. The lower axial resolution SLD source results in a significant loss of cellular-level resolution. Finally, the Hamamatsu OCT

images acquired, in particular at 1580 mA, show a good contrast with low background with slightly more degraded image resolution than the NKT-based system.

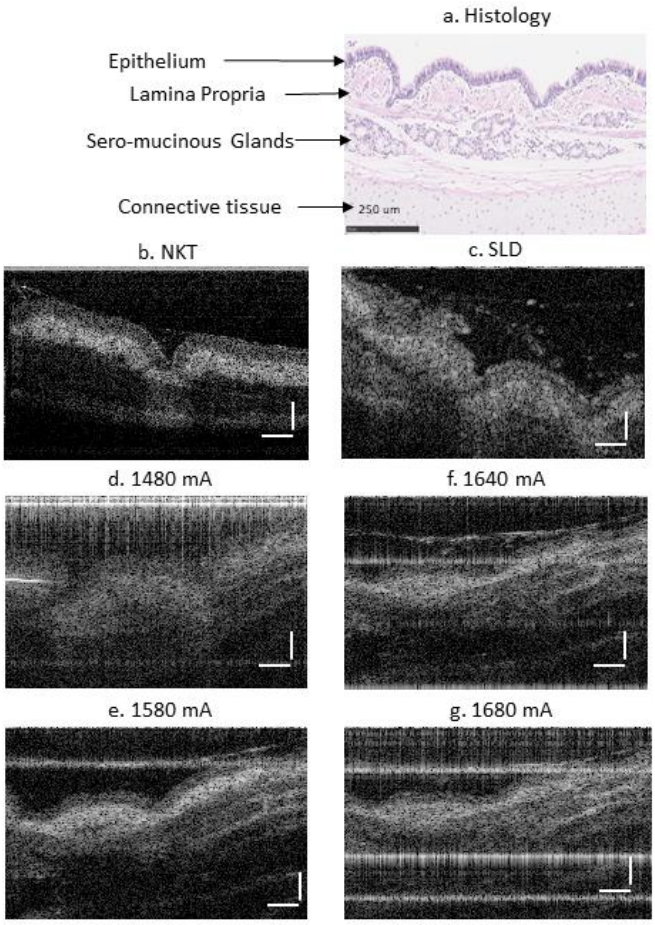

Figure 6-8: Cross-sectional OCT images from *ex vivo* lung tissue from a healthy swine acquired with the NKT, SLD and Hamamatsu sources at amplifier settings of 1480, 1580, 1640 and 1680 mA. The representative histology image shows a pseudostratified respiratory epithelium (pseudostratified ciliated columnar epithelium with interspersed goblet cells) overlying lamina propria, submucosal seromucinous glands, connective tissue. The NKT image shows distinct layers and the presence of goblet cells in the epithelium. The 1480 mA image is noisy resulting in loss of the microstructure and the 1640/1680 images are corrupted with artifacts making them difficult to interpret. The 1580 mA image is similar to the NKT in contrast and resolution while providing deeper penetration. Tissue is stained with H&E. Scale bar in images is 100 µm.

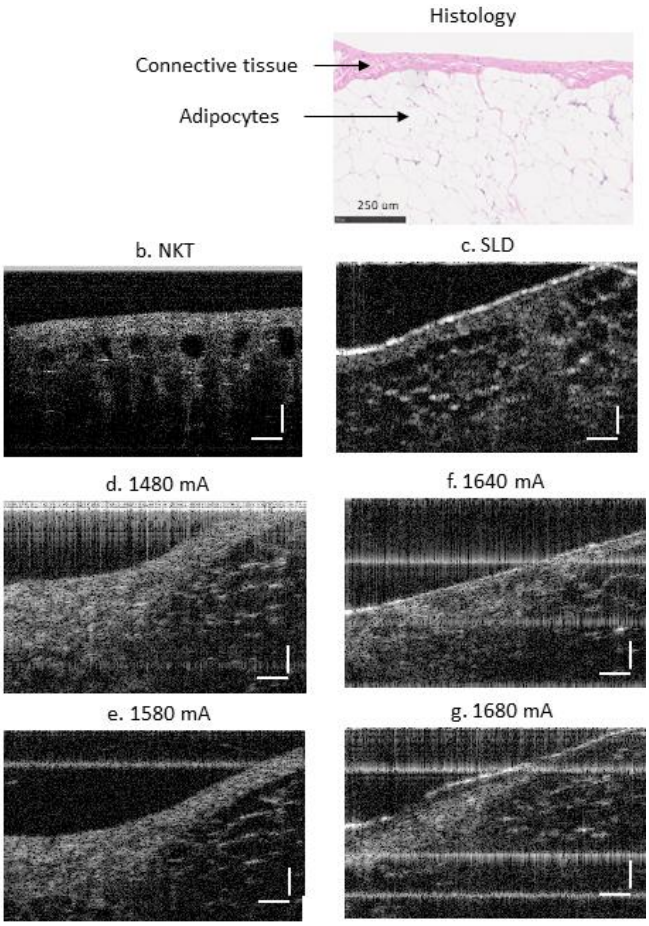

Figure 6-9: Cross-sectional OCT images of *ex vivo* skin adipose tissue from a healthy swine acquired with the NKT, SLD and Hamamatsu sources at amplifier settings of 1480, 1580, 1640 and 1680 mA. The representative histology image shows a thin fibroconnective septum overlying numerous adipocyte fat cells. NKT image clearly visualizes the connective and highly scattering adipocytes containing lipid. SLD and Hamamatsu images demonstrate the advantage of 1310 nm deeper penetration. Tissue is stained with H&E. Scale bar in images is 100 µm.

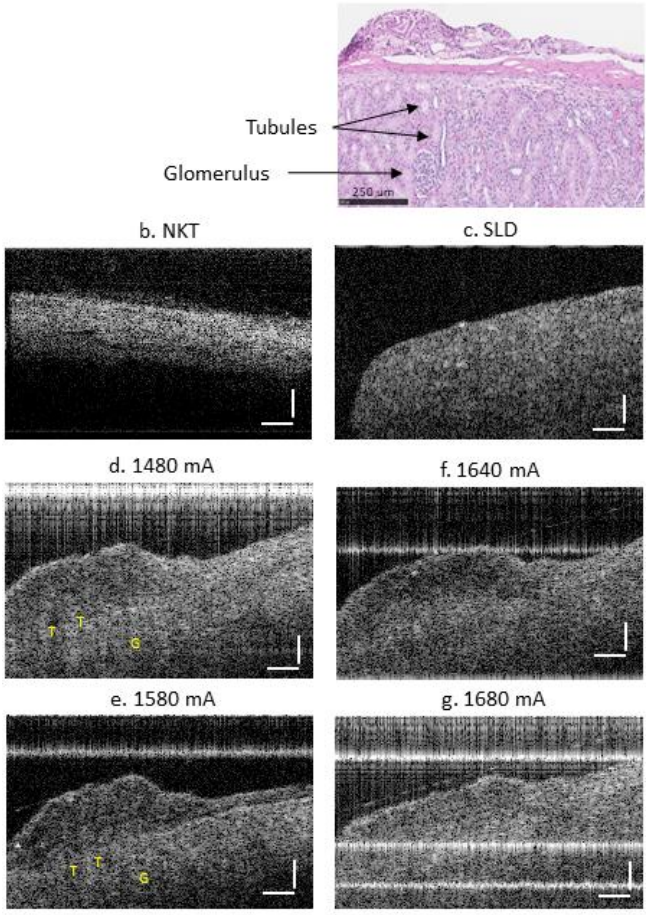

Figure 6-10: Cross-sectional OCT images of *ex vivo* kidney cortex from a healthy swine acquired with the NKT, SLD and Hamamatsu sources at amplifier settings of 1480, 1580, 1640 and 1680 mA. The specimen is imaged from the other cortex of the kidney with glomeruli (G; circular islands) and tubules (T) present. The NKT image shows a reduced imaging depth limited to 150 µm due to dense tissue structure. Morphological features, seen at greater depth, are not observed in this image. The SLD image does not have the resolution to resolve histological features. The OCT image acquired at 1480 mA lacks contrast to clearly identify features. The 1580 mA image has better contrast with possible tubules and a glomera present. Images acquired at 1640/1680 mA lack contrast and are corrupted with artifacts

making them difficult to interpret. Tissue is stained with H&E. Scale bar in images is 100 µm.

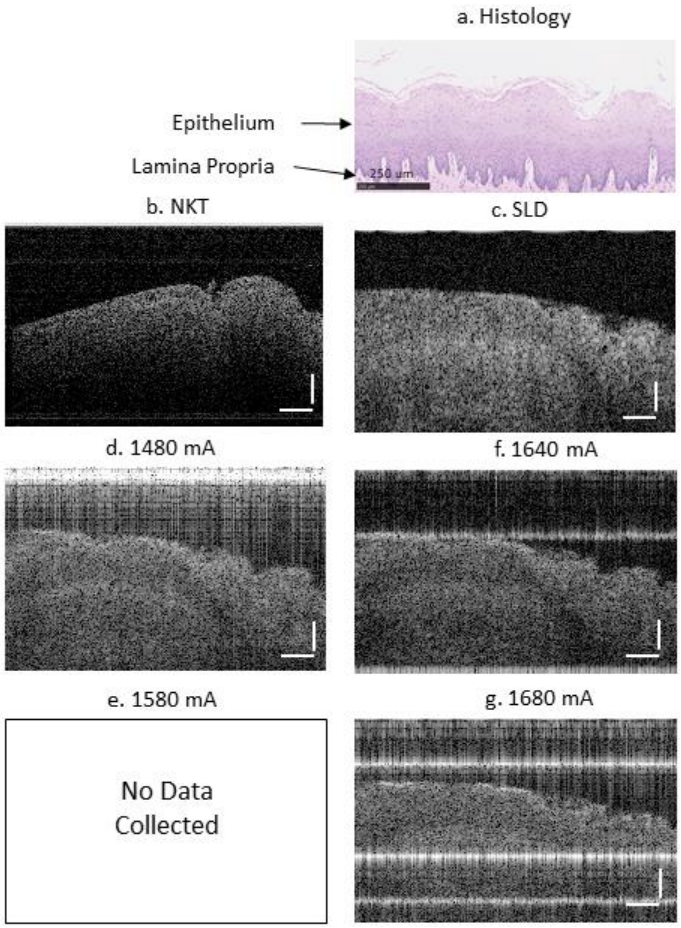

Figure 6-11: Cross-sectional OCT images of *ex vivo* esophageal tissue from a healthy swine acquired with the NKT, SLD and Hamamatsu sources at amplifier settings of 1480, 1640 and 1680 mA. All images show a lack of tissue microstructure. Tissue is stained with H&E. Scale bar in images is 100 µm.

6.4 Discussion and Future work

In this chapter, I evaluated a supercontinuum light source developed by Hamamatsu against a low-coherence SLD and the standard micro-OCT source from NKT Photonics. A supercontinuum broadband light source allows high resolution micro-OCT imaging. [32] NIR-based OCT imaging

allows deeper tissue penetration and longer imaging depth. Therefore, a NIR-based super continuum light source would allow for a high-resolution micro-OCT imaging with a longer penetration depth. [99],[100],[101],[102] A NIR-based micro-OCT system operating at 1300 nm was constructed for implementing the Hamamatsu light source and SLD light source. It can be further optimized to enhance sensitivity and resolution. The SLD spectrum exhibits the typically smooth near-Gaussian line shape. The NKT spectrum appears to be modulated by a low frequency etalon and a higher frequency ripple. The Hamamatsu source produces the expected irregular line shape characterized by low frequency etalon and high frequency ripples. The spectral performance of the Hamamatsu source showed a high degree of spectral modulation resulting in a series of satellite peaks in the depth-resolved point spread function. As the amplifier current increased, the modulations in the spectrum became more visible and the number of satellite peaks also increased. These fluctuations could be removed from the NKT OCT images by post-processing; however, it could not be removed from the Hamamatsu spectrum since there were temporal fluctuations. There was an optimum amplifier current at 1580 mA where only one artifactual peak appeared at a depth of ~100 μm in the point spread function. The coherence length of the Hamamatsu source was larger (2.8 μm) compared to the NKT (1.4 μm).

I noticed that the spectral fluctuations on the Hamamatsu spectrum were predominantly over the red-edge (>1350 nm) as it can be seen in Figure 6-4. The satellite peaks and the artifacts line could be removed by excluding the red-edge from the Hamamatsu spectra. Figure 6-12 shows results for the Hamamatsu light source at 1580 mA amplifier value. Row I shows the whole spectrum at 1580 mA, and its corresponding FFT analysis and OCT image, and row II shows results where the red-edge longer than ~1350 nm were excluded from the spectra. The ripples and artifacts were removed on the FFT signal and the OCT image, and it confirmed the artifacts were over the red-edge of the

spectrum. The transmission spectra of single mode fibers in this region have a number of absorption bands due to -OH overtones centered at 1240 and 1380 nm as shown in Figure 6-13:. [108] However, there is little chance that OH absorption and subsequent heating is the major cause. If that were the case, the entire spectrum would be affected by the change in temperature, but the effect is localized. Moreover, since Hamamatsu has a proprietary right to the light source, I do not have more information regarding the light source design and construction to address the origin of artifacts.

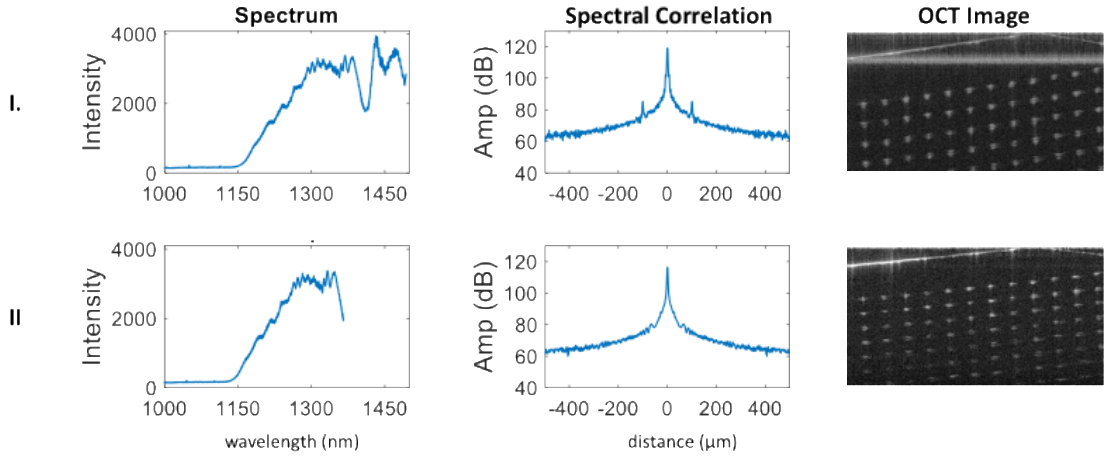

Figure 6-12: Spectral fluctuation over Hamamatsu light source. Row I shows data and its analysis from the whole spectrum of Hamamatsu at 1580 mA. Row II shows windowed-spectrum data and its analysis for ~1000-1350 nm.

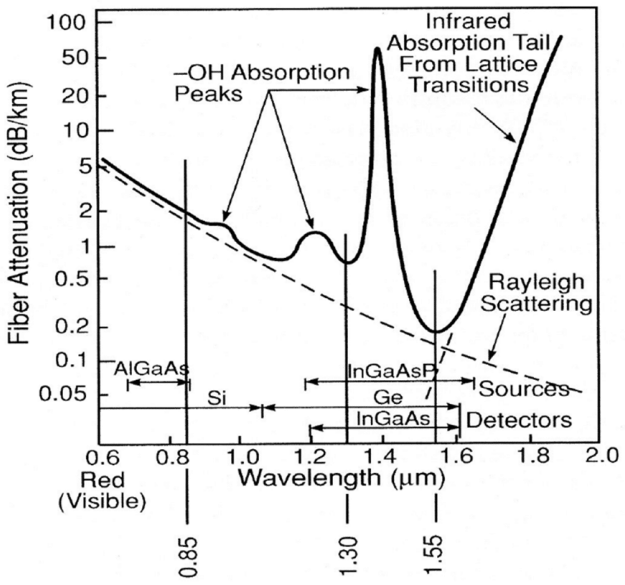

Figure 6-13: Optical fiber transmission spectrum showing the -OH absorption bands at 950, 1240 and 1380 nm.

Fresh and unfixed kidney, skin adipose, lung and esophageal tissues were imaged to evaluate performance. OCT images produced by the Hamamatsu source from tissue demonstrated the anticipated deeper imaging depths compared to NKT images by roughly 2-3 times. Qualitative comparison of the histological features in the NKT and Hamamatsu images (1580 mA) suggest that the axial resolution provided by the Hamamatsu source is slightly degraded compared to the NKT images, but in line with the approximately factor of two increase in coherence length. Hamamatsu images obtained at amplifier settings above 1580 mA became cluttered with satellite artifacts and difficult to interpret.

6.5 Conclusion

In summary, I evaluated the supercontinuum light source from Hamamatsu for NIR micro-OCT imaging. Our analysis shows the intrinsic spectral modulations in the supercontinuum are

prominent and degrade the overall quality of OCT images. Suppressing these modulations and extending the OCT bandwidth, ideally toward 1000 nm side, will result in a potentially usable source for high-resolution 1300 nm NIR micro-OCT. I reported the evaluation and results to Hamamatsu for improving the light source as well as constructing their own NIR micro-OCT system to assess the light source performance. Further optical engineering of the Hamamatsu source to increase the spectral bandwidth and suppress the intrinsic spectral modulations in the supercontinuum may result in a potentially usable source for high resolution OCT above a wavelength of 1000 nm with greater tissue penetration depth.

Chapter 7: Conclusion

7.1 Summary

It is important that cancer be detected and diagnosed at its early stage where it is localized to its tissue of origin, allowing effective treatment and improving survival and mortality rates. A non-invasive *in vivo* imaging modality with high sensitivity and specificity in diagnosing cancerous tissue is required for successful screening of patients in the clinic. OCT imaging is a great candidate technology which is making its way into clinical utility. In this work, we optimized several aspects of OCT imaging systems for early cancer diagnosis, specifically for lung and cervical cancer.

In chapter 2 and 3, an image processing/reconstruction technique was applied to 3D OCT images and 2D AF images of pulmonary endoscopic data sets. We developed a motion correction algorithm to greatly reduce motion artifacts in these images to improve image quality and to enhance image interpretation of OCT and AF images. We qualitatively evaluated this correction algorithm by visual assessment of the corrected images. We also quantitatively evaluated this correction algorithm by modeling and simulating the motion artifacts observed in the data sets and developing a metric for quantitative analysis. We also compared our proposed algorithm to a previous method from another group. We showed that our proposed algorithm resulted in a better correction compared to a previous motion correction algorithm, as well as it is computationally faster and more effective.

In Chapter 4, we evaluated a branch of OCT known as micro-OCT which provides high resolution OCT images with cellular and sub-cellular resolution. We conducted a clinical study to evaluate a bench top micro-OCT system for cervical cancer grading of low-risk and high-risk lesions. We

demonstrated that the micro-OCT has high sensitivity and specificity for diagnosis of cervical dysplasia compared to H&E histological slides and could differentiate between low-risk and high-risk lesions. Accordingly, micro-OCT has potential to be translated to the clinic as a complementary tool for cervical cancer screening.

In chapter 5, we presented an optical design and an optical model for a forward-viewing micro-OCT probe. This probe would enable the translation of the bench top micro-OCT system, described in chapter 4, into the clinic for real time *in vivo* cervical micro-OCT imaging. The optical probe was simulated and characterized based on an optical design model for its performance as a micro-OCT imaging probe. The probe was designed in order to be incorporated into the current standard of care in the cervical clinic for doing micro-OCT imaging of patients as a complementary tissue evaluation tool.

In chapter 6, we evaluated a supercontinuum light source that could potential improve micro-OCT penetration depth. This light source works in NIR region and allows for OCT imaging with deeper penetration into biomedical tissue. We compared this NIR supercontinuum OCT light source with the light source used in the bench top micro-OCT system in chapter 4, as well as a conventional OCT light source. Although there were artifact lines in the OCT images which originated from the (the noise bands?) in the light source, we observed an anticipated deeper penetration and higher resolution of OCT images of biomedical tissues using this light source. Therefore, further optical engineering is required before it becomes a potential light source that could improve the penetration depth of micro-OCT imaging for biomedical tissue imaging.

7.2 Contributions

The scholarly contributions of this thesis can be summarized as below:

- Development of a novel motion correction algorithm for 2D and 3D images from a rotary pull-back probe.

A motion correction algorithm developed and applied on OCT and AF pulmonary images. A simulation of observed motion artifacts as well as a metric was developed to quantitatively evaluate this developed motion correction algorithm.

- Clinical evaluation of a bench top micro-OCT system for diagnosis of cervical lesions.

A clinical study was conducted to assess micro-OCT imaging for screening cervical dysplasia and diagnosis of cervical lesions; the feasibility of this technique in detection and grading of cervical lesions was demonstrated. Incorporation of micro-OCT in clinical settings could potentially result in a significant increase in the accuracy of screening and detection of cervical cancer.

- Design of a forward-viewing micro-OCT probe to allow the translation of the bench top micro-OCT system into the clinic for *in vivo* micro-OCT imaging of cervical dysplasia.

A model for the optical forward-view micro-OCT probe is evaluated and characterized. A probe was designed to translate the bench top micro-OCT system into the clinic.

- Evaluation of a supercontinuum light source for NIR micro-OCT imaging.

A supercontinuum light source operating in the NIR bandwidth was evaluated for NIR micro-OCT imaging. A comparison of this light source was done against the light source used in the current bench top micro-OCT system as well as a conventional light source for an OCT system.

7.3 Future Works

The research work presented in this thesis has some limitations that need to be addressed.

We showed the motion correction based on the AF and *en face* OCT images, separately. It would be advantageous to apply the correction based on the two images simultaneously and optimize the motion correction based on the information from both image modalities in combination.

For clinical study on cervical micro-OCT imaging, it would be necessary to continue and expand the study to collect more samples and enlarge the data set to improve the performance estimates. However, there was a similar study from a group in China who showed similar results based on their large number of patients samples. [71] Their study together with ours make a strong foundation and support to take the micro-OCT imaging into the clinic for real time *in vivo* screening of patients.

As we designed a forward-viewing micro-OCT imaging probe for implementing the bench top micro-OCT system in the clinic, it remains to be built and evaluated for its performance. In future studies, the forward-viewing micro-OCT probe needs to be built, and its performance characterized. Then, verify and validate the design model; it also needs a validation of how well it would meet the users' needs, as well as validation tests for its intended use. Next steps would be to test the probe on biological samples as well as excised cervical samples and moving forward to

conduct a clinical study for *in vivo* imaging. The performance of this probe should be evaluated in the clinic for its efficacy as an *in vivo* cervical imaging tool.

Finally, one needs to improve the micro-OCT imaging performance in future. Micro-OCT provides high resolution images comparable to cellular and subcellular resolution of H&E histological slides. However, its penetration depth is limited to a few hundred microns. Using a NIR supercontinuum light source would overcome this limitation. A broadband NIR micro-OCT imaging system would enable a high resolution OCT as well as a deep penetration into the biological tissue. The Hamamatsu supercontinuum light source showed that we can achieve 2-3 times deeper penetration compared to a current supercontinuum light source at 800 nm. Although, it had some artifacts in the OCT images, further optical engineering of the light source could potential eliminate these artifacts. In the future, supercontinuum NIR light sources would allow high resolution OCT images with deeper penetration into the tissue which potentially could provide cross sectional images comparable to H&E slides.

Bibliography

1. Sung H, Ferlay J, Siegel RL, et al (2021) Global Cancer Statistics 2020: GLOBOCAN Estimates of Incidence and Mortality Worldwide for 36 Cancers in 185 Countries Hyuna. CA Cancer J Clin 0:394–424. https://doi.org/10.3322/caac.21492
2. Torre LA, Siegel RL, Ward EM, Jemal A (2016) Global cancer incidence and mortality rates and trends - An update. Cancer Epidemiol Biomarkers Prev 25:16–27. https://doi.org/10.1158/1055-9965.EPI-15-0578
3. Inage T, Nakajima T, Yoshino I, Yasufuku K (2018) Early Lung Cancer Detection. Clin Chest Med 39:45–55. https://doi.org/10.1016/j.ccm.2017.10.003
4. Kadara H, Scheet P, Wistuba II, Spira AE (2016) Early events in the molecular pathogenesis of lung cancer. Cancer Prev Res 9:518–527. https://doi.org/10.1158/1940-6207.CAPR-15-0400
5. Gargano J, Meites E, Watson M, et al (2020) Chapter 5: Human Papillomavirus. 1–11
6. Crosbie EJ, Einstein MH, Franceschi S, Kitchener HC (2013) Human papillomavirus and cervical cancer. Lancet 382:889–899. https://doi.org/10.1016/S0140-6736(13)60022-7
7. Pahlevaninezhad H, Lee AMD, Ritchie A, et al (2015) Endoscopic Doppler optical coherence tomography and autofluorescence imaging of peripheral pulmonary nodules and vasculature. Biomed Opt Express 6:4191. https://doi.org/10.1364/boe.6.004191
8. Zhang W, Ritchie AJ, Pahlevaninezhad H, et al (2015) Doppler optical coherence tomography and co-registered autofluorescence imaging of peripheral lung cancer. Endosc Microsc X; Opt Tech Pulm Med II 9304:93040B. https://doi.org/10.1117/12.2077848
9. Orfanoudaki IM, Kappou D, Sifakis S (2011) Recent advances in optical imaging for cervical cancer detection. Arch Gynecol Obstet 284:1197–1208.

https://doi.org/10.1007/s00404-011-2009-4

10. Drexler W, Fujimoto JG (2008) Optical coherence tomography: Technology and Applications

11. Pahlevaninezhad H, Lee AMD, Hohert G, et al (2016) Endoscopic high-resolution autofluorescence imaging and OCT of pulmonary vascular networks. Opt Lett 41:3209–3212. https://doi.org/10.1364/OL.41.003209

12. Duan L, McRaven MD, Liu W, et al (2017) Colposcopic imaging using visible-light optical coherence tomography. J. Biomed. Opt. 22:056003

13. Ren C, Wang B, Zeng X, et al (2020) Application of Optical Coherence Tomography on In-vivo Cervical Screening. 2020 Conf Lasers Electro-Optics Pacific Rim, CLEO-PR 2020 - Proc 6–7. https://doi.org/10.1364/CLEOPR.2020.C10D_1

14. Zuluaga AF, Follen M, Boiko I, et al (2005) Optical coherence tomography: A pilot study of a new imaging technique for noninvasive examination of cervical tissue. Am J Obstet Gynecol 193:83–88. https://doi.org/10.1016/j.ajog.2004.11.054

15. Gallwas JKS, Turk L, Stepp H, et al (2011) Optical coherence tomography for the diagnosis of cervical intraepithelial neoplasia. Lasers Surg Med 43:206–212. https://doi.org/10.1002/lsm.21030

16. Lane PM, Lam S, McWilliams A, et al (2009) Confocal fluorescence microendoscopy of bronchial epithelium. J Biomed Opt 14:024008. https://doi.org/10.1117/1.3103583

17. Gallwas J, Turk L, Friese K, Dannecker C (2010) Optical coherence tomography as a non-invasive imaging technique for preinvasive and invasive neoplasia of the uterine cervix. Ultrasound Obstet Gynecol 36:624–629. https://doi.org/10.1002/uog.7656

18. Fuchs FS, Zirlik S, Hildner K, et al (2013) Confocal laser endomicroscopy for diagnosing

lung cancer in vivo. Eur Respir J 41:1401–1408. https://doi.org/10.1183/09031936.00062512

19. Jing Y, Wang Y, Wang X, et al (2018) Label-free imaging and spectroscopy for early detection of cervical cancer. J Biophotonics 11:1–8. https://doi.org/10.1002/jbio.201700245
20. Quinn MK, Bubi TC, Pierce MC, et al (2012) High-Resolution Microendoscopy for the Detection of Cervical Neoplasia in Low-Resource Settings. PLoS One 7:1–6. https://doi.org/10.1371/journal.pone.0044924
21. Pavlova I, Hume KR, Yazinski SA, et al (2012) Multiphoton microscopy and microspectroscopy for diagnostics of inflammatory and neoplastic lung. J Biomed Opt 17:036014. https://doi.org/10.1117/1.jbo.17.3.036014
22. Zhuo S, Chen J, Luo T, et al (2009) Two-layered multiphoton microscopic imaging of cervical tissue. Lasers Med Sci 24:359–363. https://doi.org/10.1007/s10103-008-0570-2
23. Lee CY, Fujino K, Motooka Y, et al (2020) Photoacoustic imaging to localize indeterminate pulmonary nodules: A preclinical study. PLoS One 15:1–13. https://doi.org/10.1371/journal.pone.0231488
24. Peng K, He L, Wang B, Xiao J (2015) Detection of cervical cancer based on photoacoustic imaging—the in-vitro results. Biomed Opt Express 6:135. https://doi.org/10.1364/boe.6.000135
25. Drexler W, Fujimoto JG Optical Coherence Tomography- Technology and applications, 2nd ed
26. Pahlevaninezhad H, Lee AMD, Rosin M, et al (2014) Optical coherence tomography and autofluorescence imaging of human tonsil. PLoS One 9:1–11.

https://doi.org/10.1371/journal.pone.0115889

27. Pahlevaninezhad H, Lee AMD, Hohert G, et al (2016) Endoscopic high-resolution autofluorescence imaging and OCT of pulmonary vascular networks. 41:

28. Tate TH (2017) DUAL MODALITY OPTICAL COHERENCE TOMOGRAPHY AND MULTISPECTRAL FLUORESCENCE IMAGING FOR OVARIAN CANCER DETECTION

29. David Huang, Swanson EA, Lin CP, et al (1991) Optical coherence tomography. Science (80-) 254:363–375. https://doi.org/10.1007/978-3-642-27676-7_21

30. Fujimoto JG, Pitris C, Boppart SA, Brezinski ME (2000) Optical coherence tomography: An emerging technology for biomedical imaging and optical biopsy. Neoplasia 2:9–25. https://doi.org/10.1038/sj.neo.7900071

31. Yaqoob Z, Wu J, Yang C (2005) Spectral domain optical coherence tomography: a better OCT imaging strategy. Biotechniques 39:S6-13. https://doi.org/10.2144/000112090

32. Liu L, Gardecki JA, Nadkarni SK, et al (2011) Imaging the subcellular structure of human coronary atherosclerosis using micro-optical coherence tomography. Nat Med 17:1010-U132. https://doi.org/10.1038/nm.2409

33. Yin B, Hyun C, Gardecki JA, Tearney GJ (2017) Extended depth of focus for coherence-based cellular imaging. Optica 4:959. https://doi.org/10.1364/optica.4.000959

34. Nguyen VP, Paulus YM (2018) Photoacoustic ophthalmoscopy: Principle, application, and future directions. J Imaging 4:. https://doi.org/10.3390/jimaging4120149

35. Sainter AW, King TA, Dickinson MR (2004) Effect of target biological tissue and choice of light source on penetration depth and resolution in optical coherence tomography. J Biomed Opt 9:193. https://doi.org/10.1117/1.1628243

36. Uribe-Patarroyo N, Bouma BE (2015) Rotational distortion correction in endoscopic optical coherence tomography based on speckle decorrelation. Opt Lett 40:5518. https://doi.org/10.1364/ol.40.005518

37. Ahsen OO, Lee H-C, Giacomelli MG, et al (2014) Correction of rotational distortion for catheter-based en face OCT and OCT angiography. Opt Lett 39:5973–6

38. Abouei E, Lee AMD, Pahlevaninezhad H, et al (2018) Correction of motion artifacts in endoscopic optical coherence tomography and autofluorescence images based on azimuthal en face image registration. J Biomed Opt 23:1. https://doi.org/10.1117/1.jbo.23.1.016004

39. Cua M, Lee AMD, Lane PM, et al (2012) Lung vasculature imaging using speckle variance optical coherence tomography. Photonic Ther Diagnostics VIII 8207:82073P. https://doi.org/10.1117/12.906903

40. Soest G van, Bosch JG, Van Der Steen AFW (2008) Azimuthal Registration of Image Sequences Affected by Nonuniform Rotation Distortion. IEEE Trans Inf Technol Biomed 12:348–355

41. Gora MJ, Suter MJ, Tearney GJ, Li X (2017) Endoscopic optical coherence tomography: technologies and clinical applications [Invited]. Biomed Opt Express 8:2405. https://doi.org/10.1364/boe.8.002405

42. Schulz-Hildebrandt H, Pfeiffer T, Eixmann T, et al (2018) High-speed fiber scanning endoscope for volumetric multi-megahertz optical coherence tomography. Opt Lett 43:4386. https://doi.org/10.1364/ol.43.004386

43. Lee CM, Engelbrecht CJ, Soper TD, et al (2010) Scanning fiber endoscopy with highly flexible, 1 mm catheterscopes for wide-field, full-color imaging. J Biophotonics 3:385–

407. https://doi.org/10.1002/jbio.200900087

44. Liang K, Ahsen OO, Wang Z, et al (2017) Endoscopic forward-viewing optical coherence tomography and angiography with MHz swept source. Opt Lett 42:3193. https://doi.org/10.1364/ol.42.003193

45. Abouei E, Lee AMD, Pahlevaninezhad H, et al (2018) Correction of motion artifacts in endoscopic optical coherence tomography and autofluorescence images based on azimuthal en face image registration. J Biomed Opt 23:. https://doi.org/10.1117/1.JBO.23.1.016004

46. Kang W, Wang H, Wang Z, et al (2011) Motion artifacts associated with in vivo endoscopic OCT images of the esophagus. Opt Express 19:. https://doi.org/10.1364/OE.19.020722

47. Ughi GJ, Adriaenssens T, Larsson M, et al (2012) Automatic three-dimensional registration of intravascular optical coherence tomography images. J Biomed Opt 17:026005. https://doi.org/10.1117/1.JBO.17.2.026005

48. Sun C, Nolte F, Cheng KHY, et al (2012) In vivo feasibility of endovascular Doppler optical coherence tomography. Biomed Opt Express 3:2600–2610

49. Uribe-Patarroyo Né, Bouma BE (2015) Rotational distortion correction in endoscopic optical coherence tomography based on speckle decorrelation. Opt Lett 40:5518–5521

50. Hohert G, Pahlevaninezhad H, Lee A, Lane PM (2016) 3D-printed phantom for the characterization of non-uniform rotational distortion (Conference Presentation). Proc SPIE, Des Qual Biomed Technol IX, 9700:. https://doi.org/10.1117/12.2209638

51. Abouei E, Lee AMD, Hohert G, et al (2018) Quantitative evaluation of correction methods and simulation of motion artifacts for rotary pullback imaging catheters.

Commun Comput Inf Sci 894:65–73. https://doi.org/10.1007/978-3-319-95921-4_8

52. Yonetsu T, Bouma BE., Kato K, et al (2013) Optical Coherence Tomography- 15 Years in Cardiology. Circ J 77:1933–1940. https://doi.org/10.1007/978-90-481-8831-4_18

53. Pahlevaninezhad H, Cecic I, Lee AMD, et al (2013) Multimodal tissue imaging: using coregistered optical tomography data to estimate tissue autofluorescence intensity change due to scattering and absorption by neoplastic epithelial cells. J Biomed Opt 18:106007. https://doi.org/10.1117/1.JBO.18.10.106007

54. Evans JA, Bouma BE, Bressner J, et al (2007) Identifying intestinal metaplasia at the squamocolumnar junction by using optical coherence tomography. Gastrointest Endosc 65:50–56. https://doi.org/10.1016/j.gie.2006.04.027.Identifying

55. Kang W, Wang H, Wang Z, et al (2011) Motion artifacts associated with in vivo endoscopic OCT images of the esophagus. Opt Express 19:. https://doi.org/10.1364/OE.19.020722

56. Parra S, Oden M, Schmeler K, Richards-Kortum R (2019) Low-cost instructional apparatus to improve training for cervical cancer screening and prevention. Obstet Gynecol 133:559–567. https://doi.org/10.1097/AOG.0000000000003140

57. Rodriguez AC, Schiffman M, Herrero R, et al (2011) Response. J Natl Cancer Inst 103:158–159. https://doi.org/10.1093/jnci/djq485

58. Wright TC, Stoler MH, Behrens CM, et al (2015) Primary cervical cancer screening with human papillomavirus: End of study results from the ATHENA study using HPV as the first-line screening test. Gynecol Oncol 136:189–197. https://doi.org/10.1016/j.ygyno.2014.11.076

59. Arbyn M, Sasieni P, Meijer CJLM, et al (2006) Chapter 9: Clinical applications of HPV

testing: A summary of meta-analyses. Vaccine 24:78–89. https://doi.org/10.1016/j.vaccine.2006.05.117

60. (2016) PRACTICE BULLETIN No. 168: Cervical Cancer Screening and Prevention. Am Coll Obstet Gynecol 128:1118–1132

61. Zeng X, Zhang X, Li C, et al (2018) Ultrahigh resolution optical coherence microscopy for cervical cancer diagnosis. Opt InfoBase Conf Pap Part F91-T:7–9. https://doi.org/10.1364/TRANSLATIONAL.2018.CF4B.7

62. Singh V, Parashari A, Gupta S, et al (2014) Performance of a low cost magnifying device, magnivisualizer, versus colposcope for detection of pre-cancer and cancerous lesions of uterine cervix. J Gynecol Oncol 25:282–286. https://doi.org/10.3802/jgo.2014.25.4.282

63. Schlosser C, Bodenschatz N, Lam S, et al (2016) Fluorescence confocal endomicroscopy of the cervix: pilot study on the potential and limitations for clinical implementation. J Biomed Opt 21:126011. https://doi.org/10.1117/1.jbo.21.12.126011

64. Brady Hunt, José Humberto Tavares Guerreiro Fregnani RAS, Pantano N, et al (2018) Diagnosing cervical neoplasia in rural Brazi using a mobile van equipted with in vivo microscopy- A cluster-randomized commuity trial.pdf. Cancer Prev Res 11:359–369

65. Drezek R, Brookner C, Pavlova I;, et al (2001) Autofluorescence microscopy of fresh cervical-tissue sections reveals alterations in tissue biochemistry with dysplasia. Photochem Photobiol 73:636–41

66. Manuel Benavides J, Chang S, Park SY, et al (2003) Multispectral digital colposcopy for in vivo detection of cervical cancer. Opt Express 11:1223–1236

67. Fujimoto J, Swanson E (2016) The development, commercialization, and impact of optical coherence tomography. Investig Ophthalmol Vis Sci 57:OCT1–OCT13.

https://doi.org/10.1167/iovs.16-19963

68. Pitris C, Goodman A, Boppart SA, et al (1999) High-resolution imaging of gynecologic neoplasms using optical coherence tomography. Obstet Gynecol 93:135–139

69. Novikova T (2017) Optical techniques for cervical neoplasia detection. Beilstein J Nanotechnol 8:1844–1862. https://doi.org/10.3762/bjnano.8.186

70. Liu L, Chu KK, Houser GH, et al (2013) Method for Quantitative Study of Airway Functional Microanatomy Using Micro-Optical Coherence Tomography. PLoS One 8:2–13. https://doi.org/10.1371/journal.pone.0054473

71. Zeng X, Zhang X, Li C, et al (2018) Ultrahigh-resolution optical coherence microscopy accurately classifies precancerous and cancerous human cervix free of labeling. Theranostics 8:3099–3110. https://doi.org/10.7150/thno.24599

72. Belinson SE, Ledford K, Rasool N, et al (2013) Cervical epithelial brightness by optical coherence tomography can determine histological grades of cervical neoplasia. J Low Genit Tract Dis 17:160–166. https://doi.org/10.1097/LGT.0b013e31825d7bf0

73. Kirillin M, Motovilova T, Shakhova N (2017) Optical coherence tomography in gynecology : a narrative review Optical coherence tomography in gynecology : J Biomed Opt 22:. https://doi.org/10.1117/1.JBO.22.12.121709

74. Tang Y, Kortum A, Parra SG, et al (2020) In vivo imaging of cervical precancer using a low-cost and easy-to-use confocal microendoscope. Biomed Opt Express 11:269. https://doi.org/10.1364/boe.381064

75. Pantano N, Hunt B, Schwarz RA, et al (2018) Is Proflavine Exposure Associated with Disease Progression in Women with Cervical Dysplasia? A Brief Report. Photochem. Photobiol. 94:1308–1313

76. Escobar p. F, J.L.BELINSON, WHITE A, et al (2004) Diagnostic efficacy of optical coherence tomography in the management of pre-invasive and invasive cancer of the uterine cervix and the vulva. Int J Gynecol Cancer 2004, 14:470–474. https://doi.org/10.1097/00130404-200311000-00052

77. COLPOSCOPY. https://miamigyno.com/services/diagnostic-procedures/colposcopy/. Accessed 10 Mar 2021

78. Cusco's speculum. https://en.wikipedia.org/wiki/Cusco%27s_speculum. Accessed 10 Mar 2021

79. Aguirre AD (2008) Advances in Optical Coherence Tomography and Microscopy for Endoscopic Applications and Functional Neuroimaging. PhD thesis

80. Leggett CL, Gorospe EC, Chan DK, et al (2016) Comparative diagnostic performance of volumetric laser endomicroscopy and confocal laser endomicroscopy in the detection of dysplasia associated with Barrett's esophagus. 83:880–888. https://doi.org/10.1016/j.gie.2015.08.050.Comparative

81. Tearney GJ, Brezinski ME, Boppart SA, et al (1996) Catheter-based optical imaging of a human coronary artery. Circulation 94:3013

82. Tearney GJ, Brezinski ME, Bouma BE, et al (1997) In vivo Endoscopic Optical Biopsy with Optical Coherence Tomography. Science (80-) 276:2037–2039

83. Tsai T-H, Ahsen OO, Lee H-C, et al (2014) Endoscopic Optical Coherence Angiography Enables Three Dimensional Visualization of Subsurface Microvasculature. Gastroenterology 147:1219–1221. https://doi.org/10.1053/j.gastro.2014.08.034.Endoscopic

84. Jing JC, Chou L, Su E, et al (2016) Anatomically correct visualization of the human upper

airway using a high-speed long range optical coherence tomography system with an integrated positioning sensor. Sci Rep 6:1–8. https://doi.org/10.1038/srep39443

85. Seo Y-H, Hwang K, Jeong K-H (2018) 1.65 mm diameter forward-viewing confocal endomicroscopic catheter using a flip-chip bonded electrothermal MEMS fiber scanner. Opt Express 26:4780–4786. https://doi.org/10.1364/oe.26.004780

86. Pan Y, Xie H, Fedder GK (2001) Endoscopic optical coherence tomography based on a microelectromechanical mirror. Opt Lett 26:1966. https://doi.org/10.1364/ol.26.001966

87. Seibel EJ, Smithwick QYJ, Crossman-bosworth JL, Myers JA (2002) Prototype scanning fiber endoscope. Proc SPIE 4616, Opt Fibers Sensors Med Appl II 26:. https://doi.org/10.1117/12.463810

88. PiezoDrive (2020) TD250 V8- Six Channel +/-250V Amplifier, Manual and Specifications

89. PI Piezo Technology Miniaturized Piezo Tubes in High-Resolution Scanning Fiber Endoscopy. https://www.piceramic.com/en/applications/medical-technology/miniaturized-piezo-tubes/%0D%0A

90. Yin B, Piao Z, Nishimiya K, et al (2019) 3D cellular-resolution imaging in arteries using few-mode interferometry. Light Sci Appl 8:. https://doi.org/10.1038/s41377-019-0211-5

91. Okoro C, Cunningham CR, Baillargeon AR, et al (2021) Modeling , optimization , and validation of an extended-depth-of-field optical coherence tomography probe based on a mirror tunnel. Appl Opt 60:2393–2399

92. Liu X, Chen Y, Cobb MJ, Li X (2004) Rapid-scanning forward-imaging miniature endoscope for real-time forward-imaging optical coherence tomography. OSA Trends Opt Photonics Ser 29:

93. Chu KK, Unglert C, Ford TN, et al (2016) In vivo imaging of airway cilia and mucus clearance with micro-optical coherence tomography. Biomed Opt Express 7:2494. https://doi.org/10.1364/boe.7.002494

94. Leung HM, Birket SE, Hyun C, et al (2019) Intranasal micro-optical coherence tomography imaging for cystic fibrosis studies. Sci Transl Med 11:. https://doi.org/10.1126/scitranslmed.aav3505

95. Leung HM, Wang ML, Osman H, et al (2020) Imaging intracellular motion with dynamic micro-optical coherence tomography. Biomed Opt Express 11:2768. https://doi.org/10.1364/boe.390782

96. Drexler W (2004) Ultrahigh-resolution optical coherence tomography. J Biomed Opt 9:47–74. https://doi.org/10.1117/1.1629679

97. Fercher AF, Drexler W, Hitzenberger CK, Lasser T (2003) Optical coherence tomography - principles and applications. Reports Prog Phys 66:239–303. https://doi.org/10.1088/0034-4885/66/2/204

98. Fercher AF, Hitzenberger CK (2002) Chapter 4 - Optical coherence tomography. In: Wolf E (ed) Progress in Optics. Elsevier, pp 215–302

99. Yamanaka M, Hayakawa N, Nishizawa N (2019) High-spatial-resolution deep tissue imaging with spectral-domain optical coherence microscopy in the 1700-nm spectral band. J. Biomed. Opt. 24:1

100. Srinivasan VJ, Radhakrishnan H, Jiang JY, et al (2012) Optical coherence microscopy for deep tissue imaging of the cerebral cortex with intrinsic contrast. Opt Express 20:2220. https://doi.org/10.1364/oe.20.002220

101. Choi WJ, Wang RK (2015) Swept-source optical coherence tomography powered by a

1.3 - μ m vertical cavity surface emitting laser enables 2.3-mm-deep brain imaging in mice in vivo . J. Biomed. Opt. 20:106004

102. Lee S, Jeong H-W, Kim B-M, et al (2009) Optimization for Axial Resolution, Depth Range, and Sensitivity of Spectral Domain Optical Coherence Tomography at 1.3 μm. J Korean Phys Soc 55:2354–2360. https://doi.org/10.3938/jkps.55.2354.Optimization

103. Dudley JM, Genty G, Coen S (2006) Supercontinuum generation in photonic crystal fiber. Rev Mod Phys 78:1135–1184. https://doi.org/10.1103/RevModPhys.78.1135

104. Brown WJ, Kim S, Wax A (2014) Noise characterization of supercontinuum sources for low-coherence interferometry applications. J Opt Soc Am a-Optics Image Sci Vis 31:2703–2710. https://doi.org/10.1364/josaa.31.002703

105. Yuan W, Mavadia-Shukla J, Xi J, et al (2016) Optimal operational conditions for supercontinuum-based ultrahigh-resolution endoscopic OCT imaging. Opt Lett 41:250–253. https://doi.org/10.1364/ol.41.000250

106. Moon S, Qu Y, Chen Z (2018) Characterization of spectral-domain OCT with autocorrelation interference response for axial resolution performance. Opt Express 26:7253–7269. https://doi.org/10.1364/oe.26.007253

107. Birket SE, Chu KK, Liu L, et al (2014) A functional anatomic defect of the cystic fibrosis airway. Am J Respir Crit Care Med 190:421–432. https://doi.org/10.1164/rccm.201404-0670OC

108. Photonics NKT SuperK Extreme

109. Photonics A OCT Validation Phantom- APL-OP01. 44:0–2